Julius-Maximilians-Universität Würzburg
Fakultät für Physik und Astronomie
Lehrstuhl für Astronomie

Master Thesis

Jet physics with next generation VLBI arrays and radio telescopes

Author
Wladislaw Schulga

Supervisor
Dr. Christian Fromm
Prof. Dr. Matthias Kadler

ASTRO WÜRZBURG

A thesis submitted in fulfillment of the requirements for the degree of Master of Science in the group of

Dr. Christian Fromm

Chair of Astronomy

Zusammenfassung

Aktive Galaxienkerne (AGNs) sind kompakte Regionen im Zentrum von Galaxien und gehören zu den leuchtstärksten beständigen Quellen elektromagnetischer Strahlung im Universum. Sie werden durch die Akkretion von Materie auf das supermassereiche schwarze Loch im Zentrum ihrer Wirtsgalaxien angetrieben und können hochrelativistische, kollimierte Jets erzeugen, die sich über Skalen von Sub-Parsec bis zu Megaparsec erstrecken. Der genaue Mechanismus, der für den Start dieser Jets verantwortlich ist, ist nach wie vor nicht vollständig geklärt und daher Gegenstand intensiver Forschung. Während ihrer Ausbreitung über derart große Distanzen können verschiedene Instabilitäten auftreten, die die kollimierte Struktur der Jets zerstören. Aufgrund des nichtlinearen Zusammenspiels zahlreicher Parameter ist es in der Regel schwierig, analytische Stabilitätskriterien für die einzelnen Instabilitätsarten zu formulieren. Ein Ziel dieser Arbeit ist es daher, die Entstehung und Entwicklung solcher Instabilitäten anhand einer spezifischen 3D-spezialrelativistischen magnetohydrodynamischen (RMHD) Simulation eines kiloparsec-großen Jets zu untersuchen. Die simulierten Jets haben eine geringere Dichte und einen höheren Druck als das umgebende Medium. Die Magnetfelder haben eine helikale Struktur und sind eng gewunden. Mit der Zeit verliert der Jet infolge der verschiedenen auftretenden Instabilitäten – wie Rayleigh-Taylor-, Kelvin-Helmholtz- und stromgetriebener Kink-Instabilitäten – seine kollimierte Struktur. Diese Instabilitäten führen zu filamentären Strukturen innerhalb des Jets, die aus der nichtlinearen Wechselwirkung zwischen unterschiedlichen Strömungskomponenten resultieren. Dies konnte durch mehrere Raytracing-Simulationen, die im Rahmen dieser Arbeit durchgeführt wurden, bestätigt werden. Zusätzlich wurde eine Parameterstudie durchgeführt, um den Einfluss von Emissions- und Skalierungsparametern auf die resultierende spektrale Emissionsverteilung der synthetischen Quelle zu analysieren. All diese Phänomene werden typischerweise mit Hilfe der Technik der Very Long Baseline Interferometry (VLBI) beobachtet, bei der mehrere Radioteleskope über große Distanzen synchronisiert werden, um die Winkelauflösung drastisch zu verbessern. Obwohl bestehende VLBI-Arrays wie GMVA, VLBA oder VLA bereits bedeutende Fortschritte ermöglicht haben, bestehen weiterhin Einschränkungen. Viele Beobachtungen zeigen nur trichterartige Morphologien, welche die innere Plasmastruktur verschleiern. Das geplante nächste Großprojekt, das Next Generation Very Large Array (ngVLA), mit einem Betriebsfrequenzbereich von 1.2–116 GHz, verspricht eine bisher unerreichte Empfindlichkeit und Auflösung. Diese Eigenschaften können durch das LEVERAGE-Programm (Long-baseline Extension in next-generation VLBI Experiments and Rapid-response Array Germany), das die Einbindung deutscher sowie möglicherweise weiterer europäischer Stationen in das ngVLA

vorsieht, noch weiter verbessert werden. Um die Leistungsfähigkeit dieser nächsten Generation von Arrays zu testen, wurden mehrere Bildrekonstruktionen bei 15 GHz, 43 GHz und 94 GHz – die den Beobachtungsbereich des ngVLA abdecken – unter Verwendung des synthetischen Jet-Modells durchgeführt. Dabei wurden Parameter wie Intensität, Quellgröße und Deklination variiert. Darüber hinaus wurden RMHD-Simulationsdaten von M87 mit verschiedenen Array-Konfigurationen rekonstruiert, um den Nutzen der LEVERAGE-Erweiterung zu demonstrieren. Alle Rekonstruktionen zeigen deutliche Verbesserungen und unterstreichen das Potenzial zukünftiger Arrays, den sich wandelnden wissenschaftlichen Anforderungen gerecht zu werden und unser Verständnis von AGN-Jets weiter voranzutreiben.

Abstract

Active Galactic Nuclei (AGNs) are compact regions at the centers of galaxies and rank among the most luminous persistent sources of electromagnetic radiation in the universe. They are powered by mass accretion onto the central supermassive black hole of their host galaxies and can produce highly relativistic, collimated jets that extend from subparsec to megaparsec scales. The exact mechanism responsible for launching these jets remains under debate, making them an object of high scientific interest. During their propagation over such large distances, various instabilities may arise that can disrupt their collimated structure. Due to the nonlinear interplay between multiple jet parameters, it is generally difficult to derive analytic stability criteria for each type of instability. In this thesis, one objective is to investigate the development and evolution of these instabilities using a specific 3D relativistic magnetohydrodynamic (RMHD) simulation of a kiloparsec-scale, overpressured jet with a helical magnetic field with a high pitch angle. Over time, the jet loses its initial collimation due to different instabilities, such as Rayleigh-Taylor, Kelvin-Helmholtz, and current-driven kink instabilities. These instabilities lead to filamentary structures within the jet, arising from nonlinear interactions between different flow components - this could be confirmed through several ray-tracing calculations also performed as part of this work. A parameter study was further conducted to analyze how emission and scaling parameters influence the resulting spectral emission distribution (SED) of the synthetic source. All the phenomena described are typically observed via the technique of Very Long Baseline Interferometry (VLBI), which synchronizes multiple radio telescopes over large distances to drastically improve angular resolution. Although existing VLBI arrays such as the GMVA, VLBA, and VLA have enabled major breakthroughs, limitations remain. Many observations still reveal only broad, funnel-like morphologies that obscure the internal plasma structure. The upcoming next-generation Very Large Array (ngVLA), with an operational frequency range of 1.2–116 GHz, promises unmatched sensitivity and resolution. These capabilities can be further enhanced through the Long-baseline Extension in next-generation VLBI Experiments and Rapid-response Array Germany (LEVERAGE) program, which envisions adding German and possibly other European stations to the ngVLA. To test the potential of these next-generation arrays, several image reconstructions at 15 GHz, 43 GHz, and 94 GHz - representing the ngVLA's frequency coverage - were performed using the synthetic simulated and raytraced jet model, varying key source parameters such as intensity, angular size, and declination. Additionally, RMHD simulation data of M87 was reconstructed using various array configurations to demonstrate the benefit of the LEVERAGE extension. All reconstructions show significant improvements, highlighting

the capability of future arrays to meet evolving scientific demands and to further push the frontiers of our understanding of AGN jets.

Contents

1 Theoretical Background

1.1 Active Galactic Nuclei

Active Galactic Nuclei (AGNs) are among the most luminous and persistent sources of electromagnetic radiation in the universe, powered by the accretion of matter onto supermassive black holes (SMBHs) at the centers of galaxies. Their bolometric luminosities typically range from $10^{43} - 10^{48}\,\mathrm{erg\,s^{-1}}$ (Padovani 1999). Due to their extreme nature, AGNs are vital for understanding high-energy astrophysical processes and serve as important tools for probing the formation and evolution of cosmic structures (Kadler et al. 2015).

The history of AGN research began in 1909 when Edward Fath observed unusual spectral features in "spiral nebulae," some showing both absorption and emission lines. A major milestone followed in 1943 when Carl Seyfert identified galaxies with exceptionally bright nuclei and broad emission lines (Carroll & Ostlie 2017). The discovery of quasars in the 1960s, especially 3C 273, further advanced the field. Despite their star-like appearance, redshift measurements confirmed their extragalactic origin and enormous luminosity, attributed to SMBH accretion.

Similar features were later found in Seyfert galaxies, radio galaxies, and blazars, leading to the classification of AGNs into different subtypes—collectively known as the "AGN Zoo". These types and their unification under a common model will be discussed in the following chapters.

1.1.1 Classification

When not otherwise explicitly mentioned, this chapter is based on Carroll & Ostlie (2017). One criterion among others to classify AGNs is their radio-loudness which is, according to Kellermann et al. (1989), given by the ratio R_{ro} of the radio flux density S_r and the optical flux density S_o

$$R_{ro} = \frac{S_r}{S_o} \tag{1.1.1}$$

and allows to differentiate the sources into radio-loud ($R_{ro} > 10$) and radio-quiet (0.1 $< R_{ro} < 1$) objects. Only a small part ($\approx 10\%$) of all galaxies is radio loud, showing a powerful radio jet. Another approach is to study the optical spectra of the sources. AGNs with broad emission lines are called type 1 sources, while those with narrow emission lines are called type 2 sources. Additionally, there is one type with weak or unusual line emission (type 0) (Urry & Padovani 1995). According to Fanaroff & Riley (1974) radio-loud AGNs can be further divided into two luminosity classes based on the ratio R_{FR} of the distance between the brightest spots of radio emission on either side of the center to the full extent of the radio source. Sources with $R_{FR} < 0.5$ were placed in class I (FRI) and sources with $R_{FR} > 0.5$ in class II (FRII). In other words, FRI galaxies' radio luminosity diminishes with increasing distance from the core and have two jets, whereas FRII galaxies tend to be most radio-bright at the end of the lobes and show only one recognizable radio jet.

Seyfert galaxies for example are radio quiet spiral galaxies with a bright core which are divided in two subclasses based on their optical spectra. **Seyfert I** have quite variable X-ray emission which can change on timescales from days to hours. **Seyfert II** in contrast, have weak X-ray emission.

Radio galaxies are an example of radio-loud AGNs. They are extremely bright at radio wavelengths and can be divided into two classes according to their emission line properties, similar to Seyfert galaxies. Broad line radio galaxies (**BLRG**) show broad and narrow emission lines and have bright, starlike nuclei surrounded by very faint, hazy envelopes. Narrow line radio galaxies (**NLRG**) show only narrow emission lines and their host galaxies are giant or supergiant elliptical galaxies.

Quasars (quasi-stellar radio sources) are another important type of objects. Quasars are very distant (redshifts up to $z > 7$ (Wang et al. 2021)) sources with overwhelming brightness and have starlike nuclei surrounded by faint fuzzy halos. Sometimes this fuzzy halo can be resolved into a faint parent galaxy. Quasars can also be divided into radio-loud quasars (**QSR**) and radio-quiet quasars (**QSO**). Furthermore, QSRs can be separated - depending on the value of their radio spectral index α_r - into steep-spectrum radio quasars (**SSRQ**, $\alpha_r > 0.5$) and flat-spectrum radio quasars (**FSRQ** , $\alpha_r < 0.5$). Since FSRQs have multifrequency spectra which are dominated by non-thermal emission, they are also included in 'type 0'.

Blazars are defined by rapid variability and a high degree of linear polarization at visible wavelengths. The most prominent blazar is BL Lacertae located in the constellation of Lacerta (Latin for lizard). More details on this source can be found in Schulga (2023). The irregular variation in its brightness led originally to the classification as a variable star. The luminosity doubled up in a week and changes by a factor of 15 in timescales of months. Despite its stellar appearance, the spectrum shows only a featureless continuum with very weak absorption and emission lines. Blazars that show similar properties to BL Lacertae are therefore called **BL Lac** objects. In general, BL Lac objects are also characterized by weak or absent emission lines, beside the above mentioned high polarization and rapid variability. To visualize the astonishing time variability: the

luminosities can change by up to 30% in just 24 hours and even by a factor of 100 over a longer period of time. 90% of all BL Lacs are in elliptical galaxies.
To summarize: Although there is a big AGN zoo, it became clear that there are only a few parameters which determine the flavour of an AGN. Within the scope of this thesis, the parameters are restricted to: radio-loudness, width of the emission lines and the luminosity. It is mentionable that there are attempts to improve the classification model by adding parameters like accretion rates or by using time-dependent systems since all the mentioned parameters change with time (Padovani et al. 2017). The classification of AGNs is also listed in Tab.1.1 taken from Kadler (2023) [1]

Type	Radio Loudness	Emission Lines	Luminosity	Jets?	Radio Morphology
Seyfert 1	RQ	B+N	Low	No	-
Seyfert 2	RQ	N	Low	No	-
QSO (type 1)	RQ	B+N	High	No	-
QSO (type 2)	RQ	N	High	No	-
BLRG	RL	B+N	Low	Yes	FR1
	RL	B+N	High	Yes	FR2
NLRG	RL	N	Low	Yes	FR1
	RL	N	High	Yes	FR2
BL Lac	RL	-	Low	Yes	Compact
FSRQ	RL	B+N	High	Yes	Compact

Table 1.1: Simplified classification of AGNs with only a few parameters mentioned above. RQ = radio-quiet, RL = radio-loud, B = broad emission lines, N = narrow emission lines.

1.1.2 Unification

Although AGNs exhibit diverse observational features (see Sect. 1.1.1), they can be broadly unified under the **Unification Model** proposed by Urry & Padovani (1995). According to this model, all AGNs are powered by the same underlying physical processes, and the observed differences primarily arise from variations in the **viewing angle**. At the core of every AGN lies a **supermassive black hole (SMBH)** with a typical mass of $10^6\,M_\odot$ and a diameter on the order of 1 AU (Padovani 1999). The two defining parameters of a black hole - **mass and spin** - strongly influence an AGN's observable characteristics. More massive black holes are easier to detect due to their higher luminosity. This relationship is determined by the Eddington ratio, which is the ratio between the observed luminosity and the Eddington luminosity: $L_{Edd} = 1.31046(M/10^8 M_\odot\ )$erg/s. This represents the maximum isotropic luminosity a body can achieve when radiation pressure on electrons counterbalances the gravitational pull on protons (Padovani et al.

[1]Extragalactic jets, Lecture on extragalactic jets held in the summer term

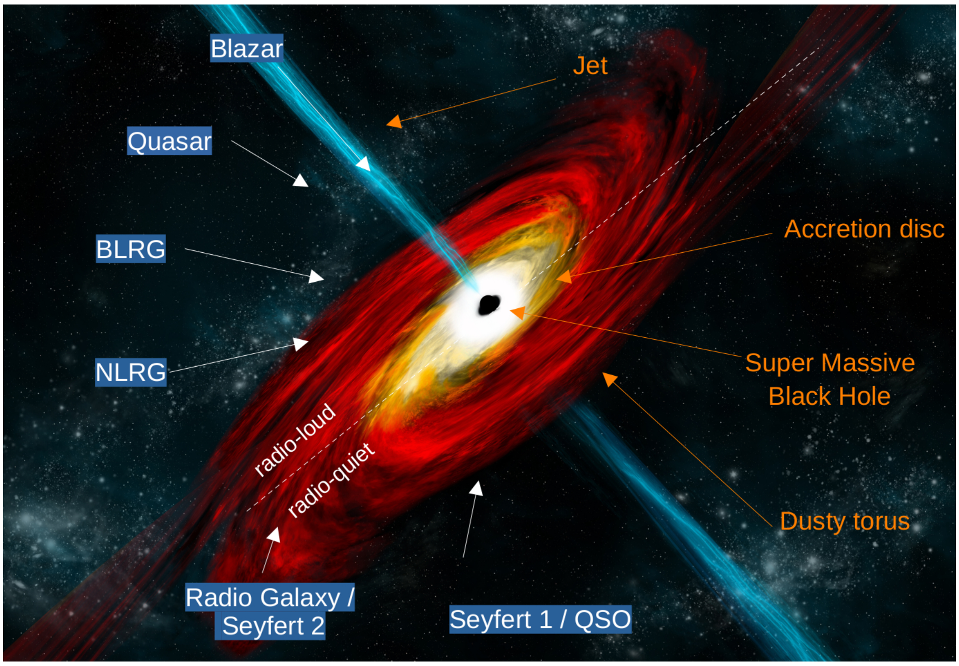

Figure 1.1: Artistic impression of all important classes of AGN unified in one picture according to Padovani (1999). The observed objects are represented through the white arrows which also shows the viewing angle. The picture is also separated in radio-loud (upper part) and radio-quiet (lower part) AGNs, divided by the dotted white line. Adopted by University of Pittsburgh [2]

2017). Surrounding the SMBH is an **accretion disk**, which emits radiation by converting gravitational energy into heat. Enveloping this is the **broad-line region (BLR)** with electron densities around $n \sim 10^{10}, \mathrm{cm}^{-3}$, responsible for producing broad emission lines. Further out, a **dusty torus** - spanning 0.01 to 10 parsecs - obscures the inner regions depending on orientation (Burtscher et al. 2013). Beyond the torus lies the **narrow-line region (NLR)**, characterized by lower densities $n \sim 10^4, \mathrm{cm}^{-3}$, where narrow emission lines are produced. The key distinction lies in whether the inner region is visible (Type 1 AGNs) or obscured by the dust torus (Type 2 AGNs). In Type 2 AGNs, the dust torus absorbs radiation, leading to weaker emissions, such as the reduced X-ray emissions observed in Seyfert I and II galaxies. In **radio-loud AGNs**, relativistic **jets** are launched perpendicular to the accretion disk and can extend from 0.1 kpc up to hundreds of kpc (Padovani 1999). The **viewing angle** with respect to the jet axis determines the observed AGN type, as illustrated in Fig. 1.1.

[2]https://www.psc.edu/wp-content/uploads/2024/05/AdobeStock_94796347.jpeg

1.2 Relativistic magnetohydrodynamics (RMHD)

Since jets are collimated flows of relativistic particles, it is essential to introduce the fundamental concepts of relativistic magnetohydrodynamics. In this thesis, the focus is on the evolution of jets far from their formation region, where the effects of general relativity can be neglected. Therefore, the framework of special relativistic hydrodynamics will be employed. The movement of relativistic plasma governed by magnetic fields can be described by

$$\partial_\mu(\rho U^\mu) = 0 \tag{1.2.1}$$

$$\partial_\mu(T^{\mu\nu}_{pl} + T^{\mu\nu}_{em}) = 0 \tag{1.2.2}$$

which is the combination of plasma stress-energy and electromagnetic field stress-energy tensor. Here ρ is the particle density, $\mu, \nu = 0,\ 1,\ 2,\ 3$ are the temporal and spatial components of the four-velocity $U^\mu = \gamma(t, v^1, v^2, v^3)$, where $\gamma = 1/\sqrt{1 - v^i v_i/c^2}$ and the plasma energy-momentum tensor T:

$$T^{\mu\nu}_{pl} = (\rho c^2 + \rho\epsilon + p)\frac{U^\mu U^\nu}{c^2} + p g^{\mu\nu} \tag{1.2.3}$$

The electromagnetic energy-momentum tensor can be written as:

$$T^{\mu\nu}_{em} = F^\mu_\gamma F^{\nu\gamma} - \frac{1}{4} g^{\mu\nu} F^{\gamma\delta} F_{\gamma\delta} \tag{1.2.4}$$

where F is the electromagnetic tensor. For numerical codes like BHAC (Porth et al. 2017) which solve these equations, one has to rewrite the system into a conserved form. This formulation makes the underlying conservation laws — for mass, momentum, energy, and magnetic flux — explicit, and is particularly suited for numerical schemes such as the Finite Volume Method, which rely on fluxes across cell interfaces. The conserved form of the RMHD equations results in:

$$\frac{\delta}{\delta t}(\gamma\rho) + \nabla(\gamma\rho\mathbf{v}) = 0 \quad \text{continuity equation} \tag{1.2.5}$$

$$\frac{\delta}{\delta t}(\omega_t\gamma^2\mathbf{v} - b^0\mathbf{b}) + \nabla\cdot(\omega_t\gamma^2\mathbf{vv} - \mathbf{bb} + \delta^i_j p_t) = S_0 \quad \text{momentum conservation} \tag{1.2.6}$$

$$\frac{\delta}{\delta t}(\omega_t\gamma^2 - b^0 b^0 - p_t) + \nabla\cdot(\omega_t\gamma^2\mathbf{v} - b^0\mathbf{b}) = S_j \quad \text{energy conservation} \tag{1.2.7}$$

$$\frac{\delta}{\delta t}\mathbf{B} + \nabla\cdot(\mathbf{vB} - \mathbf{Bv}) = 0 \quad \text{magnetic field} \tag{1.2.8}$$

where $c = 1$ is the speed of light in natural units, $\Gamma = 4/3$ (adiabatic index),

$$b^0 = \gamma \mathbf{v} \cdot \mathbf{B} \tag{1.2.9}$$

the time component of the magnetic 4-vector in the co-moving frame,

$$\sigma = |\mathbf{b}|^2/\rho \tag{1.2.10}$$

is the magnetization,

$$\mathbf{b} = \mathbf{B}/\gamma + \gamma(\mathbf{v} \cdot \mathbf{B})\ \mathbf{v} \tag{1.2.11}$$

is the magnetic field in the fluid frame, where

$$\omega_t = \rho h + B^2/\gamma + (\mathbf{v} \cdot \mathbf{B})^2 \tag{1.2.12}$$

is the total enthalpy density,

$$p_t = p_{gas} + [B^2/\gamma^2 + (\mathbf{v} \cdot \mathbf{B}^2]/2 \tag{1.2.13}$$

is the total pressure and

$$h = 1 + \Gamma p_{gas}/(\Gamma - 1)\rho \tag{1.2.14}$$

is the specific enthalpy. In numerical schemes such as the Finite Volume Method, the evolution is performed on conserved quantities mentioned above, which are defined as cell-averaged values and updated via fluxes across cell interfaces. After each timestep, the corresponding primitive variables (ρ, v, p, B), which represent the physical state of the fluid, are recovered from the conserved quantities through a non-linear inversion procedure.

1.3 Radiative processes

To understand the emission and absorption processes which one observes in a large variety in AGNs, it is essential to understand the interaction between photons and particles and particles with each other. The highest photon energies are reached through inverse Compton processes in the jet or in a plasma close to the accretion disk, whereas the emission processes in the jet are dominated by synchrotron emissions. This section discusses synchrotron emission and is primarily based on Rybicki & Lightman (1979). Some of the material presented here has also appeared in Schulga (2023), where it was likewise based on Rybicki & Lightman (1979).

1.3.1 Synchrotron radiation - basics

In one sentence, the synchrotron radiation can be explained like this: Synchrotron radiation is the electromagnetic radiation emitted when relativistic charged particles spiral around magnetic field lines (Rybicki & Lightman 1979). Since it is the essential radiation process of this thesis, I want to derive it in more detail starting with the basics. Accelerated charged particles radiate energy. This conclusion follows from the Liénard-Wiechert potentials (Nolting 2007)

$$\phi(\mathbf{r}, t) = \frac{q}{\kappa(t_{ret})R(t_{ret})} \tag{1.3.1}$$

$$\mathbf{A} = \frac{\mathbf{v}(t_{ret})}{c}\phi(\mathbf{r}, t) \tag{1.3.2}$$

where $\kappa(t_{ret}) = 1 - \frac{1}{c}\mathbf{n}(t_{ret}) \cdot \mathbf{v}(t_{ret})$, $R(t_{ret}) = |\mathbf{r} - \mathbf{r_0}(\mathbf{t_{ret}})|$ describes the trajectory of a particle with charge q and velocity $\mathbf{v}(\mathbf{t}) = \frac{d\mathbf{r_0}(t)}{dt}$ and $\mathbf{n} = \mathbf{R}/R$ is the unit vector. These are solutions to the inhomogeneous Maxwell equations while accounting for retardation effects (generalized Coulomb potential). From the Lienard-Wiechert potentials, one can derive the electric and magnetic fields of a moving charge by means of

$$\mathbf{E}(\mathbf{r}, t) = -\nabla\phi(\mathbf{r}, t) - \frac{\partial \mathbf{A}(\mathbf{r}, t)}{\partial t} \tag{1.3.3}$$

and

$$\mathbf{B}(\mathbf{r}, t) = \nabla \times \mathbf{A}(\mathbf{r}, t). \tag{1.3.4}$$

Using these fields, the total emitted power can be calculated, leading to the Larmor formula (Rybicki & Lightman 1979). For non-relativistic velocities, the Larmor formula for emission power from a single accelerated charge q is given by :

$$P = \frac{2q^2\vec{a}^2}{3c^3} \tag{1.3.5}$$

with $\vec{a}$ as acceleration and c as light speed. For a particle which is moving with relativistic speeds, Larmor's formula reads:

$$P = \frac{2q^2}{3c^3}\gamma^4(\vec{a}_\perp^2 + \gamma^2\vec{a}_\parallel^2) \tag{1.3.6}$$

in which $\vec{a}_\perp$ is the perpendicular and $\vec{a}_\parallel$ is the parallel component of the acceleration. The relativistic equations of motion for a certain particle of mass m and charge q in a magnetic field $\vec{B}$ are given by:

$$\frac{d}{dt}(\gamma m\vec{v}) = \frac{q}{c}\vec{v} \times \vec{B} \tag{1.3.7}$$

$$\frac{d}{dt}(\gamma mc^2) = q\vec{v} \cdot \vec{E} = 0 \tag{1.3.8}$$

in which $\vec{v}$ is the velocity and $\vec{E}$ the electric field. From Eq.1.3.8 one can see that $\gamma =$ const. Writing the velocity as a sum of components (perpendicular and parallel) along the field and in a plane normal to the field $\vec{v} = (\vec{v_\perp} + \vec{v_\parallel})$ gives:

$$\frac{d\vec{v_\parallel}}{dt} = 0 \tag{1.3.9}$$

and

$$\frac{d\vec{v_\perp}}{dt} = \frac{q}{\gamma mc}\vec{v_\perp} \times \vec{B} \tag{1.3.10}$$

what leads to a differential equation describing a uniform circular motion. If one combines the solutions for this circular motion and the uniform motion along the field ($v_\parallel$) one gets a helical motion with a rotation frequency (gyration) of:

$$\omega_B = \frac{qB}{\gamma mc} \tag{1.3.11}$$

which results in:

$$a_\perp = \omega_B v_\perp \tag{1.3.12}$$

Combining this information with Eq.1.3.6 one obtains the total emitted radiation averaged over all angles for a given speed β:

$$P = \frac{4}{3}\sigma_T c \beta^2 \gamma^2 U_b \tag{1.3.13}$$

Figure 1.2: Angular distribution of the radiation of a particle whose acceleration is perpendicular to its velocity. Taken from Rybicki & Lightman (1979)

in which $\sigma_t = 8\pi r_0^2/3$ is the Thomson cross section, $r_0 = q^2/mc^2$ and $U_b = B^2/8\pi$ is the magnetic energy density. For non-relativistic speeds the nature of the radiation process is rather simple and is called cyclotron radiation. The frequency of emission is simply the frequency of gyration in the magnetic field (Rybicki & Lightman 1979). At relativistic speeds which are present in AGN jets there are two important effects which have to be considered, namely **relativistic beaming** and the **lighthouse effect**. Relativistic beaming is the process in which relativistic effects affect the apparent luminosity of emitting matter that is moving at speeds close to the speed of light. So, if, for example, a cloud of gas is moving towards an observer, its emitted radiation would appear brighter than that of a cloud at rest. On the other side, the emission would appear fainter if the cloud moves away from the observer. Because of this effect the emitted radiation fields appear to be concentrated in a narrow cone directed into the particles' velocity direction with an angular width of $1/\gamma$. According to Eq.1.3.7, the acceleration of the particles is perpendicular to their velocity, so the angular distribution of the emission looks like that which is shown in Fig.1.2.

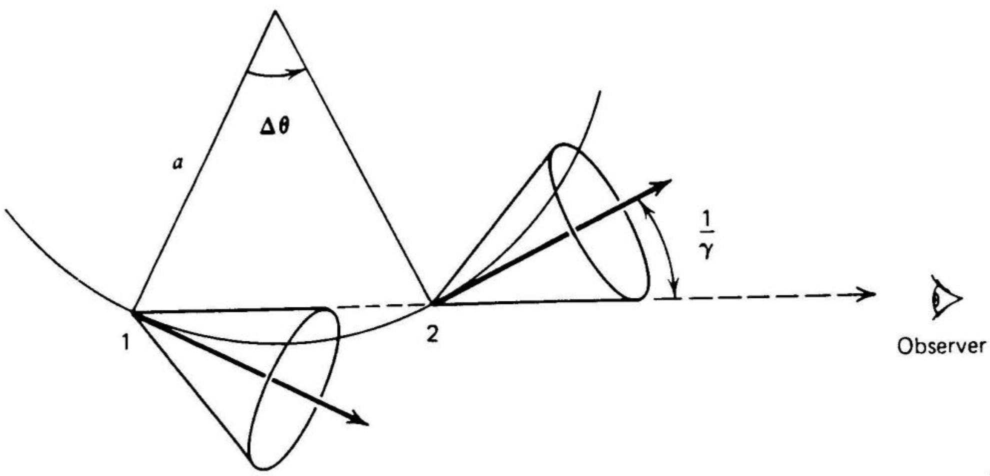

Figure 1.3: Emission cones at various points of an accelerated particle's trajectory. Taken from Rybicki & Lightman (1979)

Considering this effect and the fact that the electron moves in a helical motion as mentioned above, an observer registers pulsed radiation of the length $\delta t = (\gamma^3 \omega_b \sin(\alpha))^{-1}$ if it crosses his line of sight see Fig.1.3. As one can see, the width of the observed pulses is smaller than the gyration period by the factor of γ^3. This is the reason why the observed frequency of radiation is much greater than the gyration frequency, leading to a continuous synchrotron spectrum in comparison to the discrete cyclotron spectrum.

1.3.2 Synchrotron spectrum and radiative transfer

Once the solutions of the RMHD equations (see 1.2) are obtained, one needs to compute the geodesics of the spacetime (e.g., Kerr or Schwarzschild) to determine the paths of light rays. Subsequently, the evolution of an ensemble of particles emitting synchrotron radiation must be analyzed to track the intensity evolution of the radiation along those paths (see Fig. 1.4). This can be done by solving the radiative transfer equation along the rays that pass through the simulated plasma.

$$\frac{dI_\nu}{ds} = j_\nu - \kappa I_\nu. \tag{1.3.14}$$

To include the effect of synchrotron self-absorption, one can define the so-called optical depth, which is a measure of how much absorption occurs along the path to

$$\tau = \int \kappa ds \tag{1.3.15}$$

Now the radiative transfer equation 1.3.14 can be rewritten as

$$\frac{dI_\nu}{d\tau} = -I_\nu + \frac{j_\nu}{\kappa_\nu} \tag{1.3.16}$$

By the integrating factor method one can solve this equation to

$$I_\nu(s) = I_\nu(s_0)\exp^{-\tau(s)} + \int_{s_0}^{s} j_\nu(\mathbf{r}')\exp^{-[\tau(s)-\tau(s')]} ds' \tag{1.3.17}$$

One can assume that the background radiation $I_\nu(s)$ is negligible, which results in (Rybicki & Lightman 1979)

$$I_\nu(s) = \int_{s_0}^{s} j_\nu(\mathbf{r}')\exp^{-[\tau(s)-\tau(s')]} ds' \tag{1.3.18}$$

The emission- and absorption coefficients, $j(\epsilon)$ and $\kappa(\epsilon)$, of an ensemble of particles $N(\gamma)$ following a powerlaw distribution $N(\gamma) = k_e\gamma^{-p}$ can be expressed by (detailed derivation can be found in Rybicki & Lightman (1979))

$$j(\epsilon) = \frac{\sqrt{3}e^3 B}{4\pi h}\int_{\gamma_{min}}^{\gamma_{max}} N(\gamma)G(x)d\gamma \tag{1.3.19}$$

and

$$\kappa(\epsilon) = \frac{\sqrt{3}e^3 B h^2}{8\pi m_e^4 \epsilon^2 c^6}\int_{\gamma_{min}}^{\gamma_{max}} \left[\gamma^2 \frac{\partial}{\partial\gamma}(\frac{N(\gamma)}{\gamma^2})\right] \cdot G(x)d\gamma \tag{1.3.20}$$

where $G(x)$ - according to Aharonian et al. (2010) - is an approximation to the integral over pitch angles and the Bessel function of order $\frac{5}{3}$, $K_{5/3}$

$$G(x) \approx \frac{1.808x^{1/3}}{\sqrt{1+3.4x^{2/3}}}\frac{1+2.21x^{2/3}+0.347x^{4/3}}{1+1.353x^{2/3}+0.217x^{4/3}}e^{-x} \tag{1.3.21}$$

where $x = \frac{4\pi\epsilon m_e^2 c^3}{3eBh\gamma^2}$ consists of dimensionless energy $\epsilon = \frac{h\nu}{m_e c^2}$ where h is the Planck constant, c the speed of light, m_e mass of the electron, B the magnetic field, e the

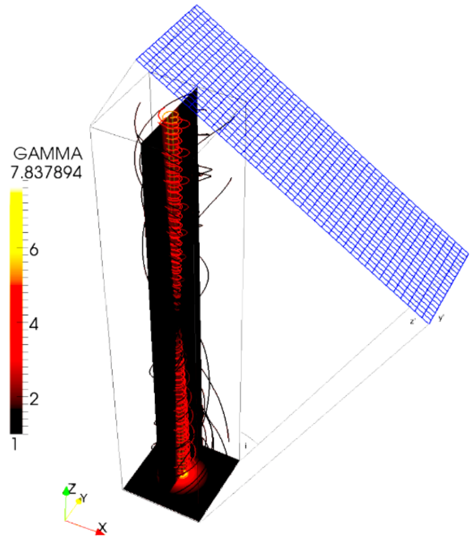

Figure 1.4: Illustration of the raytracing geometry on an exemplary solution. Taken from Porth (2011).

elementary charge and $\gamma = [1 - (v/c)^2]^{-0.5}$ as the Lorentz factor.

The flux density S_ν is given by Rybicki & Lightman (1979):

$$S_\nu = \int I_\nu d\Omega \tag{1.3.22}$$

where $d\Omega$ is the solid angle of the source. For a distant source, one can approximate the solid angle as $d\Omega = dA/d^2$ with A as the area of the emitting region and d as the line of sight distance to the source. By inserting eq.1.3.18 and using eq.1.3.15 one gets

$$S_\nu = \int j_\nu(\mathbf{r}') \exp^{-\int \kappa(\mathbf{r}')\mathbf{ds}'} dV \tag{1.3.23}$$

The flux density when observing a spherical volume with the radius R_b ($dV = 2\pi\rho d\rho dl$) at large distances ($d_l >> R_b$) can be calculated by

$$S_\nu = \frac{1}{4\pi d_l^2} \int d^3\mathbf{r}\ j(\epsilon; \mathbf{r} \exp(- \int \kappa(\mathbf{r}')ds') \tag{1.3.24}$$

With the assumption that the emission and absorption coefficients are uniformly distributed ($j(\epsilon;\mathbf{r}) = j(\epsilon)$ and $\kappa(\mathbf{r}) = \kappa$ for $r \leq r_b$ one can write

$$
\begin{aligned}
S_\nu &= \frac{j(\epsilon)}{2d_l^2}\int_0^{r_b} d\rho\rho \int_0^{2\sqrt{r_b^2-\rho^2}} dl \exp(-\kappa l) \\
&= \\
&\frac{j(\epsilon)}{8d_l^2\kappa^3}\int_0^{2\kappa r_b} dxx(1-\exp^{-x}) \\
&= \frac{j(\epsilon)}{2\kappa}(\frac{r_b^2}{d_l^2})u(\tau)
\end{aligned}
\tag{1.3.25}
$$

So the total synchrotron spectrum including self-absorption from a spherical region (referred to as 'blob') of radius R_b traveling with bulk Lorentz factor Γ seen under a viewing angle θ in a source located at a luminosity distance d_l can be written as

$$
S_\nu = \frac{\delta^4 j(\epsilon)V_b 3u(\tau)}{4\pi d_l^2\tau}
\tag{1.3.26}
$$

where $\delta = \frac{1}{(\Gamma(1-\beta\cos(\theta)}$ is the Doppler factor (with $\beta = \frac{v}{c}$), $\tau = \int \kappa ds = 2\kappa R_b$ as the optical depth along the path ds and $V_b = \frac{4\pi}{3R_b^3}$ is the volume of the emitting spherical region Dermer & Menon (2009). The factor $u(\tau)$ can be obtained by

$$
u(\tau) = 0.5[1 - \frac{2}{\tau^2}(1-(1+\tau)e^{-\tau}]
\tag{1.3.27}
$$

The normalization factor k_e is computed by combining the equation of the energy density $u_e = \frac{3w_e}{4\pi R_b^3}$ - where a certain energy w_e is assumed within an emitting spherical region constrained by R_b - and the energy density contained within the emitting particles

$$
u_e = m_e c^2 \int_{\gamma_{min}}^{\gamma_{max}} \gamma N(\gamma) d\gamma
\tag{1.3.28}
$$

With the aforementioned power law distribution of particles, the normalization factor results in

$$
k_e = \frac{3w_e(-p-2)}{4\pi R_b^3 m_e c^2}\frac{1}{\gamma_{max}^{-p+2} - \gamma_{min}^{-p+2}}
\tag{1.3.29}
$$

.

An exemplary synchrotron spectrum as well as a demonstration of absorption effects introduced by synchrotron self-absorption mechanisms in eq.1.3.15 are shown in Fig. 1.5. There, the optical depth was sent to zero ($\tau \to 0$). This means that the light can pass through the medium (e.g dust torus, NLR or BLR) with nearly no attenuation, which would allow photons with lower energy to reach their observers. For this reason, it is sometimes possible to reveal the inner core of the jet by observing at higher frequencies, whereas observation at lower frequencies results in more detected flux.

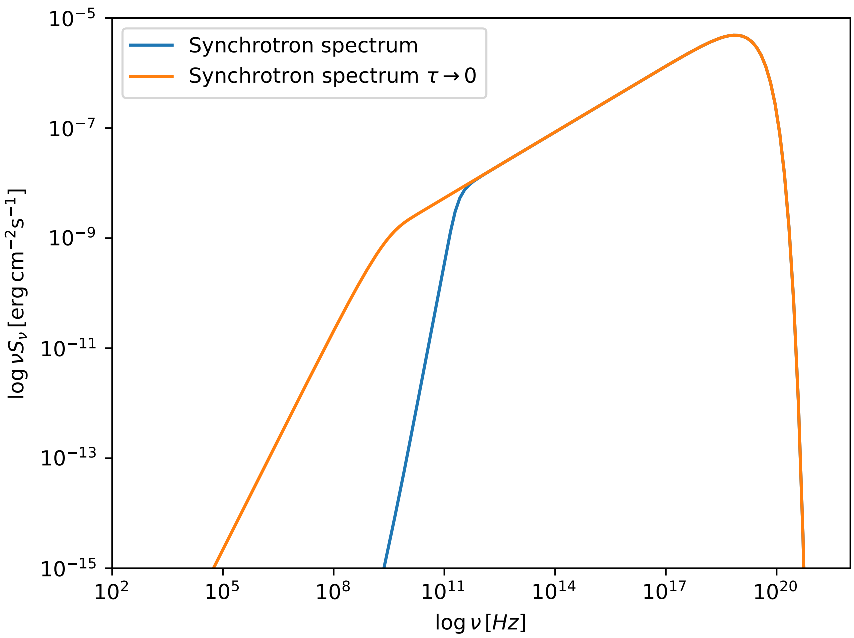

Figure 1.5: Synchrotron spectrum (blue) for a source with luminosity distance $d_l = 45$ Mpc, magnetic field B = 1 G, velocity $\beta = 0.95$, viewing angle $\theta = 3°$, total energy $w_e = 1 \cdot 10^{50} ergs$ and a power law particle distribution with a spectral slope of p = 2.2 within boundaries $\gamma_{min} = 10$ and $\gamma_{max} = 1 \cdot 10^6$. The effect of absorption for the synchrotron spectrum can be seen in orange. Here the optical depth τ was send to 0.

1.4 Very Long Baseline Interferometry (VLBI)

If not mentioned otherwise, the following chapter is based on Burke et al. (2019). Because of the radio window of the Earth's atmosphere, we are able to observe the electromagnetic radiation in the radio band from the Earth's surface. The radio flux density S_ν is the relevant quantity, which has to be determined. Its common unit is Jansky (Jy), which is the energy per time, surface area and frequency.

$$1\mathrm{Jy} = 10^{-27} [\frac{\mathrm{J}}{\mathrm{s\,m^2\,Hz}}] \tag{1.4.1}$$

To analyze the structure of objects like AGNs one has to be able to resolve them. The angular resolution for a single dish telescope follows the Rayleigh criterion

$$\theta \approx 1.22\frac{\lambda}{D}; [\theta] = \mathrm{rad} \tag{1.4.2}$$

Due to the circular aperture of radio dishes, the resulting intensity distribution follows an Airy pattern, which is described by a Bessel function. Two neighboring Airy patterns are just distinguishable when the central maximum of one coincides with the first minimum of the other. The numerical factor 1.22 arises from the location of the first minimum of the first-order Bessel function. This factor equals 1 for a rectangular beam of uniform intensity and 1.27 for a beam of Gaussian intensity distribution, see (Bass et al. 1995). Since observations are made at a constant wavelength λ, the only way to improve resolution is by increasing the telescope's diameter D. However, this approach quickly reaches practical limits, as the largest single-dish telescopes are around 500 meters in diameter (Nan et al. 2011). A more effective method to achieve higher resolution is Very Long Baseline Interferometry (VLBI). In this technique, one tries to synchronize multiple radio telescopes at the phase center of the antennas via baselines $\vec{b}_\lambda = \frac{\vec{b}}{\lambda}$ - the connection of the reflection centers of two telescopes. The baselines should be as large as possible for the best angular resolution. The simplest way to explain all important aspects of this technique is to have a look at a two-element interferometer like it is shown in Fig.1.6.

1.4.1 Radio interferometry

Two-element interferometer

The power received by one single telescope is given by

$$P = \int_0^\infty d\nu A_{eff}(\nu) S(\nu). \tag{1.4.3}$$

where A_{eff} is the effective area, which is smaller than the actual collecting area because in reality the total power will never be measured by a telescope and $S(\nu)$ is the flux density given by

$$S(\nu) = \int_{sky} d\Omega I(\nu, \theta, \phi) \tag{1.4.4}$$

where the angles ϕ and θ denote the incoming signal and $I(\nu, \theta, \phi)$ is the brightness distribution. Two of such antennas result in a two-element interferometer. Both antennas of such a connection are identical and point at a source under the direction $\vec{s} = \vec{s_0} + \vec{\sigma}$, where $\vec{s_0}$ is the reference direction and $\vec{\sigma}$ is the distance from the center of the source to the center of the primary beam, see Fig.1.6. The source is tracked by these two telescopes and one of them is selected as reference. There is a geometrical delay $\tau_g = \frac{\vec{b}\vec{s}}{c}$ when the signal arrives at the reference antenna. Additionally, the second antenna also receives an instrumental delay τ_i to equalize the signals. If $\tau_g = \tau_i$, the reference direction $\vec{s_0}$ mentioned before is defined as the phase tracking center. The cross-correlation $R_{xy}(\tau)$ - also called cross-power product since it has the dimension of power - over two amplitudes (voltages) x and y is given by :

$$R_{xy}(\tau) := \langle x(t)y(t-\tau)\rangle = SA(\vec{s})cos(2\pi\vec{b_\lambda}\vec{s}) \tag{1.4.5}$$

One of our assumptions is that the observed source is monochromatic, so the amplitudes can be expressed as $x(t) = v_1 \cos(2\pi\nu t)$ and $y(t) = v_2 \cos(2\pi\nu(t-\tau))$. The time average of the multiplication of $x(t)$ and $y(t)$ gives the received power of the source, which is proportional to the source flux S and the effective antenna area $A(\vec{s})$. The output of an antenna from an observation of an object at a frequency ν corresponds to the output noise power of a black body at this frequency. Here, like already mentioned above, the baseline vector $\vec{b}$ is measured in wavelengths, which allows to simplify corresponding expressions.

Array of N-telescopes

Since the most measurements are taken place with more than two telescopes, it is useful to generalize the results above to an array of N telescopes. In an array with N dishes, there exist N(N-1)/2 baselines b_{ij}. The fundamental equation for a practical interferometer is given by the complex visibility:

$$V_{i,j} = \int A(\sigma)I_\nu(\sigma)\exp(i2\pi b_{i,j,\lambda}\sigma)d\Omega \tag{1.4.6}$$

The amplitude and the phase of this function are the principal observables in interferometry, which can be measured with an array of multiple baselines $\vec{b}_{i,j}$ with an instrumental delay τ_i adjusted to the geometrical delay τ_g.
To get a relation between the complex visibility function $V_{i,j}$ and the brightness distribution $I_\nu(\sigma)$ of the observed source, it is useful to introduce the right-handed rectilinear coordinate system (u, v, w). The w-direction can be defined with the unit vector $\vec{s_0}$

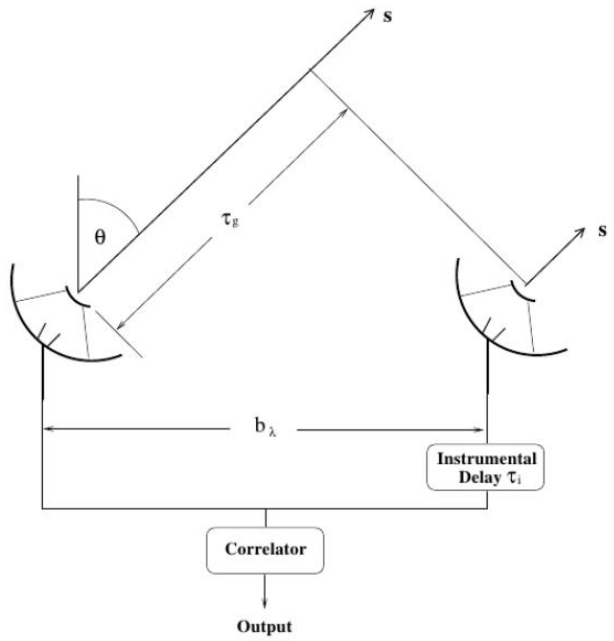

Figure 1.6: The general structure of the two-element Michelson interferometer. Taken from Burke et al. (2019)

which is perpendicular to the (u,v)-plane consisting of u, which is projected into the eastern direction and v, which is projected into the northern direction. The offset vector $\vec{\sigma}$ is parallel to the (u,v)-plane. With this assumption Eq.1.4.6 becomes

$$V_{i,j} = \int_{4\pi} A(l,m) I_\nu(l,m) \exp[i2\pi(ul + vm + wn)] d\Omega \tag{1.4.7}$$

where l,m,n are the direction cosines of the unit vector $\vec{s}$. So, (l,m) are the coordinates of $\vec{\sigma}$ and w=0 because $\vec{s_0}$ is perpendicular to the (u,v)-plane. With this consideration, the solid angle $d\Omega$ can be written as

$$d\Omega = \frac{\mathrm{dl}\,\mathrm{dm}}{\sqrt{1 - l^2 - m^2}} \tag{1.4.8}$$

Since for most cases the offset angle σ is small, it is practical to rewrite Eq.1.4.6 in terms of the rectilinear coordinates for σ, x and y in the small angle approximation:

$$V(u,v) \approx \int A(x,y) I(x,y) \exp[2\pi i(ux + vy)] dxdy \tag{1.4.9}$$

With this introduced coordinate system one now can see that the visibility in the (u,v)-

plane is the Fourier transform of a source's brightness distribution in the (x,y)-plane

$$V(u,v)\overset{FT}{\longleftrightarrow}I(x,y) \tag{1.4.10}$$

The biggest problem in practice is that it is not possible to cover the whole (u,v)-plane. Only a sample coverage is available.

$$V(u,v) \longrightarrow S(u,v)V(u,v) \tag{1.4.11}$$

where

$$S(u,v) = \sum_k \omega_k \delta(u-u_k)\delta(v-v_k) \tag{1.4.12}$$

where ω_k is the weighting factor.

The missing pieces in the (u,v)-plane lead to a loss of Fourier components in the synthesized image. One tries to fill up these components as far as possible with the so-called aperture synthesis, where the Earth's rotation is used to cover the empty areas in the (u,v)-plane, which means that each pair of telescopes samples a trajectory of spatial frequencies as a function of time. Such coverages depend on the position and the declination of the telescopes. For a declination of $\pm 90\,\mathrm{deg}$ the (u,v)-coverage would be circular, whereas a coverage with a certain declination results in an elliptical geometry, e.g Fig.1.7.

Because VLBI incompletely samples the Fourier transform of the source image, any image reconstruction that attempts to fill in the unmeasured spatial frequencies is inherently non-unique, and thus requires reconstruction algorithms (Chael et al. 2016). The standard reconstruction method is the CLEAN algorithm (Högbom 1974), which models the image as a collection of point sources. To recover the true brightness distribution with CLEAN, one must deconvolve the so-called dirty image.

$$I^D(x,y) = \int S(u,v)V(u,v)\exp[-2\pi i(ux+vy)]dudv \tag{1.4.13}$$

applying Eq.1.4.12 one gets:

$$I^D(x,y) = \sum_k V(u_k,v_k)\omega_k \exp[-2\pi i(u_k x+v_k y)] \tag{1.4.14}$$

With the convolution theorem one gets

$$I^D = P^D * I \tag{1.4.15}$$

with

$$P^D = \int S(u,v)\exp[-2\pi i(ux+vy)]dudv \tag{1.4.16}$$

which equals:

$$P^D = \sum_k \omega_k \exp[-2\pi i(ux + vy)] \tag{1.4.17}$$

where the so-called dirty beam P^D is equivalent to a point spread function. The CLEAN algorithm reconstructs the sky image by iteratively identifying the brightest point in the dirty image and subtracting a scaled version of the dirty beam from that location. These subtracted components are stored and later convolved with an idealized clean beam (typically a Gaussian) to form the final image. This process effectively deconvolves the dirty beam from the observed data, yielding a more accurate estimate of the true brightness distribution. An alternative to deconvolution-based imaging in VLBI is to fit a model directly to the visibility data using Bayesian regularization methods, which incorporate prior knowledge about the image's spatial structure and physical properties. A prominent example is the Maximum Entropy Method (MEM), which selects the image that best matches the data while maximizing an entropy function — conceptually similar to the log of a prior probability distribution (Chael et al. 2016). Since this method will be primarily used in this thesis, it will be discussed in more detail in Chapter 1.6.

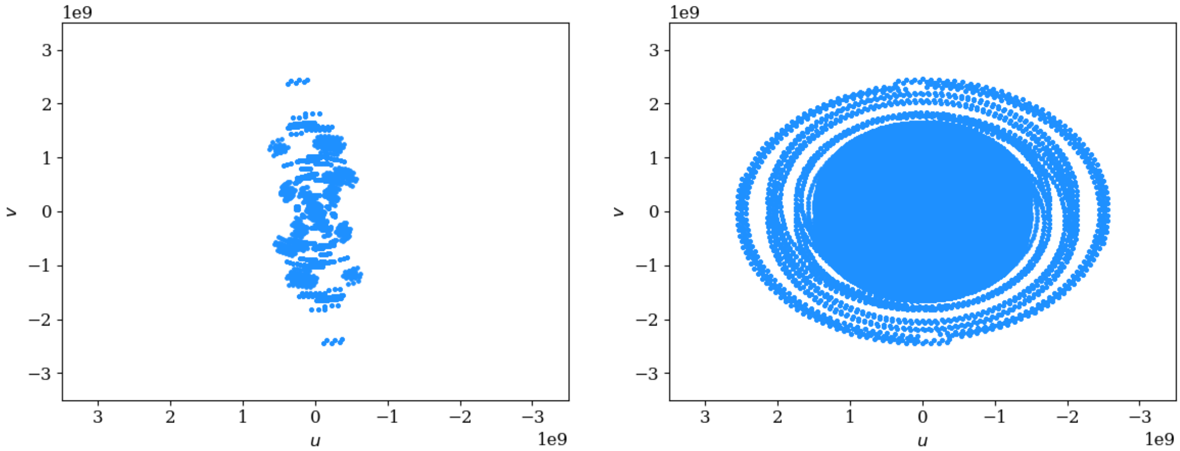

Figure 1.7: Uv-coverage of a generic source at a declination of 70° at 94 GHz observed with ngVLA to demonstrate the effect of aperture synthesis. On the left an observation with 1 h observation duration and on the right 24 h observation.

1.4.2 Sensitivity

Sensitivity refers to the smallest detectable level of radio emission from a source and is a crucial parameter for characterizing the performance of a telescope or an array (Wrobel & Walker 1999). There are two important types which play a role. On the one hand, there is the **baseline sensitivity**, which refers to the sensitivity of a single baseline in an interferometer array and is given according to Wrobel & Walker (1999) and Wrobel (1995) by

$$\Delta S_{i,j} = \frac{1}{\eta}\sqrt{\frac{SEFD_i SEFD_j}{2\Delta t \Delta \nu}} \tag{1.4.18}$$

where Δt is the integration time, $\Delta \nu$ is the bandwidth, η is the efficiency constrained by the telescope properties and $SEFD_i$ is the system equivalent flux density of the i-th telescope, which is given by

$$SEFD = \frac{2kT_{sys}}{\eta A_{eff}}. \tag{1.4.19}$$

On the other hand, there is the overall sensitivity of the interferometric array for producing an image of a source called **image sensitivity**. The image sensitivity for an array of N identical telescopes is given by Wrobel (1995) and Wrobel & Walker (1999):

$$\Delta S_{image} = \frac{1}{\eta}\frac{SEFD}{\sqrt{N(N-1)\Delta\nu\Delta t}} \tag{1.4.20}$$

where T_{obs} is the total observation time. In the case of different telescopes, the formula changes according to the EVN calculator website [3]to:

$$\Delta S_{image} = \frac{1}{\eta}\frac{SEFD^*}{\sqrt{\frac{R}{2}T_{obs}}} \tag{1.4.21}$$

where R is the data rate in bit/s and $SEFD^*$ is given by:

$$SEFD^* = \frac{1}{\sqrt{\sum_{i,j}^{N;i<j}\frac{1}{SEFD_i SEFD_j}}} \tag{1.4.22}$$

1.4.3 Disturbance effects

When observing a radio source, various effects can interfere with the received signal and degrade data quality. In an ideal scenario, a radio telescope would only detect radiation coming directly from the line of sight. However, in reality, the sensitivity of a parabolic radio telescope varies with angle and is highest along the so-called main beam - the central axis of the telescope's field of view. In addition to this primary sensitivity, the telescope also detects radiation from other directions due to side lobes. These become particularly problematic when strong, unrelated sources lie near the direction of observation, introducing significant contamination. Another important factor is scattering. Incoming radio waves can scatter off the feedhorn and its mounting, distorting or

[3]https://services.jive.eu/evn-calculator/cgi-bin/EVNcalc.pl

weakening the signal. Radio frequency interference (RFI) poses another challenge, originating from artificial or man-made sources, and can superimpose unwanted signals onto the astronomical data. Lastly, the spillover effect refers to radiation that bypasses the primary focus and directly reaches the secondary focus, further complicating accurate signal reception.

1.4.4 Closure relationships

Closure effects refer to specific relationships between visibility measurements taken on baselines that form a closed geometric shape - such as a triangle or quadrilateral - where each vertex represents an antenna (Thompson et al. 2017). The signals in a synthesis array may pass through multiple analog devices like amplifiers, filters, and mixers before being converted to digital form, so it is important to consider the effect of gain variations. The correlator output for an antenna pair (i,j) can be written as:

$$r_{ij} = G_{ij} V_{ij} = g_i g_j^* V_{ij} \tag{1.4.23}$$

where V_{ij} is the source-dependent complex visibility from which the intensity map can be computed and G_{ij} is the complex gain for the antenna pair and g_i and g_j are gain factors for the individual antennas, which contain the effects of the atmospheric paths to the antennas as well as already mentioned instrumental effects. In practice, the G_{ij} values may be determined from observations of calibration sources for which the visibilities are known. Although it is possible to correct the correlator output data directly by the measured antenna pair gains, it is reasonable to determine the gain factors for individual antennas like it is shown in Eq.1.4.23. The motivation behind it is that VLBI data is big (e.g bandwidth = 46 GHz → 92 Gsamples/sec, according to the Nyquist criterion → 2 bits/sample and dual polarization result in 368 Gbps per antenna which is 95.3 TB per day per antenna)[4]and one wants to avoid redundant information. In a large array, there are far more antenna pairs (baselines) than individual antennas - specifically, $N(N-1)/2$ baselines for N antennas (Burke et al. 2019). By applying closure relations (like closure phase), one constructs triangles of baselines to reduce the number of independent measurements needed for calibration, helping to manage this large number of baselines. This means that not all of the calibration data must be used, giving flexibility in the calibration process. For instance, if a source is resolved (i.e., appears extended) on the longest baselines, you can still use measurements from the shorter baselines - where the source remains compact - to accurately determine the antenna gains (Thompson et al. 2017). Since the written out form of the gains is $g = |g|e^{j\phi}$, one can use the arguments of the exponential terms to constitute the following phase relationship based on Eq.1.4.23:

$$\phi_{ij} = \phi_i - \phi_j + \phi_{vij} \tag{1.4.24}$$

[4]https://star.herts.ac.uk/regvlbi/files/mex19_colomer.pdf

where ϕ_{ij} is the measured phase ϕ_i and ϕ_j are the phase errors associated with the i-th telescope and ϕ_{vij} is the real phase which one wants to determine (calibrate). For three antennas i, j, k, the phase closure relationship is

$$\begin{aligned}\phi_{c_{ijk}} &= \phi_{ij} + \phi_{jk} + \phi_{ki} \\ &= \phi_i - \phi_j + \phi_{vij} \\ &+ \phi_j - \phi_k + \phi_{vjk} \\ &+ \phi_k - \phi_i + \phi_{vki}\end{aligned} \tag{1.4.25}$$

where $\phi_{c_{ijk}}$ is the closure phase, which is the sum of the measured phases around a loop of three baselines. From Eq.1.4.25 one can see that the individual telescope phase errors cancel out, which results in:

$$\phi_{c_{ijk}} = \phi_{vij} + \phi_{vjk} + \phi_{vki}. \tag{1.4.26}$$

Here it is evident that the combination of the three correlator output phases constitutes an observable quantity that depends only on the phase of the visibility. In the same manner, the amplitude closure relations can be written as:

$$A_{cl} = \frac{|r_{ij}||r_{kl}|}{|r_{ik}||r_{jl}|} = \frac{|V_{ij}||V_{kl}|}{|V_{ik}||V_{jl}|} \tag{1.4.27}$$

Although closure relationships recover some phase and amplitude information, they do not preserve the absolute values. Since it is important to avoid redundant information — for example, to improve computational efficiency, especially in large arrays like the ngVLA where the number of baselines increases rapidly with the number of dishes N — it is useful to determine how many baselines carry independent phase and amplitude information. This can be quantified by calculating the fractions of independent closure phases and closure amplitudes relative to the total number of measured visibilities. These fractions of recoverable phase and amplitude information, denoted as f_ϕ and f_A, respectively, are given by:

$$f_\phi = \frac{N-2}{N} \tag{1.4.28}$$

and

$$f_A = \frac{N-3}{N-1} \tag{1.4.29}$$

Further details and explanations can be found in Thompson et al. (2017). The cyclical process in finding the calibration gain factors g_i and g_j involves intensive computation, and also must be repeated at frequent intervals. The process is, however, fully automated in a suite of programs known as the Astronomical Image Processing System (AIPS) (Burke et al. 2019).

1.5 Arrays

1.5.1 Next Generation Very Large Array (ngVLA)

Motivation and science goals

All images and tables are adopted from the offical ngVLA website if not mentioned otherwise : https://ngvla.nrao.edu/. Since the start of the operation in the 70s, the Very Large Array (VLA) has been a cornerstone of astronomical research, contributing to thousands of high-impact discoveries across nearly every field of astronomy. Since its upgrade to the Expanded VLA (EVLA) and rededication as the Karl G. Jansky VLA in 2012, it remains one of the world's most versatile and widely used radio telescopes, supporting over 11,000 observing projects by more than 3,000 researchers globally. To build on this legacy and meet evolving scientific priorities, the National Radio Astronomy Observatory (NRAO) is planning the next-generation VLA (Murphy et al. 2017).

Figure 1.8: VLA Y-shape. Taken from https://public.nrao.edu/gallery/this-is-the-vla-wye/

The next-generation Very Large Array (ngVLA) is an astronomical observatory planned to operate at a frequency range extending from 1.2 - 50.5 GHz and 70 - 116 GHz in multiple bands (see Tab.1.2) - adopted from Selina et al. (2020). The observatory will be a synthesis radio telescope constituted of around 244 reflector antennas, each of 18 meters diameter, and 19 reflector antennas, each of 6 meters diameter, operating in a phased or interferometric mode (Selina et al. 2020).
It aims to significantly surpass the capabilities of both the current VLA and ALMA, offering a tenfold improvement in resolution and sensitivity. Comparisons to other arrays are shown in Fig.1.14 and Fig.1.9. It will be designed in collaboration with the broader astronomical community, which has proposed over 80 science use cases [5]that address fundamental astrophysical problems. These cases require observing capabilities at centimeter and millimeter wavelengths that go well beyond those of existing or planned telescopes, aiming to explore new frontiers in this regime. The science cases submitted spanned a broad range of topics which form the basis for developing the ngVLA Key Science Goals (KSGs).
Given the large and diverse range of compelling science cases proposed by the community, it was clear that the primary scientific requirement for the ngVLA is **flexibility**. The array must be capable of supporting a broad spectrum of investigations throughout

[5]https://ngvla.nrao.edu/page/scicase

Band	f_L (GHz)	f_M (GHz)	f_H (GHz)	BW (GHz)	η_A		
					@ f_L	@ f_M	@ f_H
1	1.2	2.0	3.5	2.3	0.80	0.79	0.74
2	3.5	6.6	12.3	8.8	0.80	0.78	0.76
3	12.3	15.9	20.5	8.2	0.84	0.87	0.86
4	20.5	26.4	34.0	13.5	0.83	0.86	0.83
5	30.5	39.2	50.5	20.0	0.81	0.82	0.78
6	70.0	90.1	116.0	46.0	0.68	0.61	0.48

Table 1.2: ngVLA frequency bands and aperture efficiency (η_A) at selected frequencies.

its operational lifetime. This need is underscored by the wide-ranging topics - from planet formation and the conditions for habitability to fundamental tests of gravity using pulsars near the Galactic Center's supermassive black hole and instability investigations within the outer jet lobes of AGNs. This broad scientific scope distinguishes the ngVLA from other next-generation facilities such as SKA-1 and LSST, which are more focused on large-scale surveys. To prioritize scientific goals, all submitted science cases were objectively reviewed and discussed within the ngVLA Science Advisory Council's Science Working Groups. Each KSG met three key criteria:

1. It addresses a major open question in astrophysics with broad relevance beyond radio astronomy.

2. It requires the unique capabilities of the ngVLA.

3. It complements ongoing or upcoming science efforts at other facilities expected to be operational around 2025.

The top five KSGs emerged from this process, representing a community-driven vision for the ngVLA's core science objectives, are briefly displayed in Tab.1.3. For further details on KSGs, see Bolatto et al. (2017).

KSG	Title
1	Unveiling the Formation of Solar System Analogs on Terrestrial Scales
2	Probing the Initial Conditions for Planetary Systems and Life with Astrochemistry
3	Charting the Assembly, Structure, and Evolution of Galaxies from the First Billion Years to the Present
4	Using Pulsars in the Galactic Center to Make a Fundamental Test of Gravity
5	Understanding the Formation and Evolution of Stellar and Supermassive Black Holes in the Era of Multi-Messenger Astronomy

Table 1.3: The ngVLA Key Science Goals

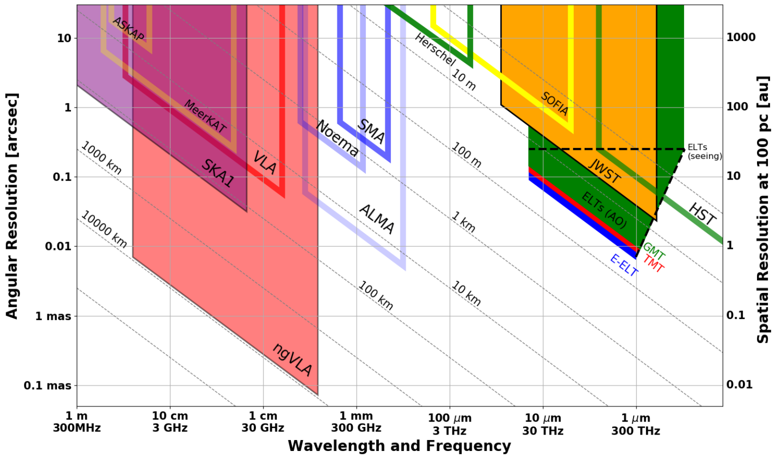

Figure 1.10: Comparison of the angular resolution capabilities of current and upcoming facilities, spanning radio to optical wavelengths, anticipated to be operational in the 2030s.

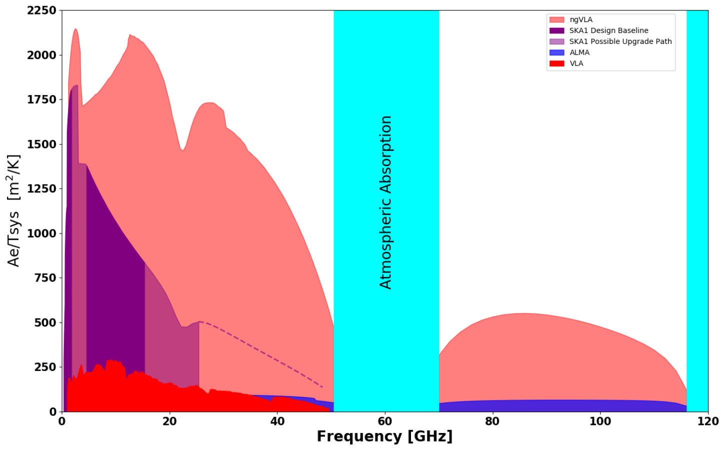

Figure 1.9: Comparison of the sensitivity of various radio, millimeter, and sub-millimeter dish arrays projected to be operational in the 2030s. The y-axis represents the effective collecting area divided by the system temperature - a key metric that reflects antenna efficiency, receiver performance, and atmospheric transparency across frequencies.

1.5.2 The ngVLA reference design

As already mentioned, the observatory will be a synthesis radio telescope consisting of

- **Main Array**: The core of the ngVLA will consist of 214 reflector antennas, each with an 18-meter diameter, operating in phased or interferometric mode. These antennas will be distributed across baselines ranging from tens of meters to approximately 1000 kilometers, enabling observations across a wide range of spatial scales. A dense central core combined with spiral arms will provide enhanced surface brightness sensitivity, while mid-baseline stations will contribute to improved angular resolution , see Fig.1.11a and Fig.1.11b

- **Short Baseline Array** (**SBA**): To recover larger angular scale structures that the main array cannot detect, the ngVLA will include a Short Baseline Array composed of 19 reflector antennas, each 6 meters in diameter. Additionally, four 18-meter antennas from the main array will operate in total power mode alongside the SBA to help fill in the central gap in the (u, v)-plane coverage that results from the SBA's smaller dishes, see Fig.1.11c

- **Long Baseline Array** (**LBA**): The ngVLA will also feature a Long Baseline Array, adding 30 additional 18-meter antennas, organized into 10 clusters. This configuration will enable continental-scale baselines of up to approximately 8860 kilometers ($B_{max} \approx 8860$ km). The LBA is designed for both standalone sub-array use and integrated observations with the main array, enabling high-resolution imaging across a broad range of angular scales, see Fig.1.11a (Selina et al. 2020).

The ngVLA will offer roughly **10x** the sensitivity of both the current VLA and ALMA (Fig.1.9), with continental-scale baselines enabling sub-milliarcsecond resolution, and a dense central core optimized for high surface brightness sensitivity on kilometer scales. Such an array bridges the gap between ALMA, a superb sub-mm array, and the future SKA1, optimized for longer wavelengths. The dense core and central signal processing facility will be located at the current VLA site on the plains of San Agustin, New Mexico. Situated at over 2000 m elevation, the site offers excellent atmospheric conditions for observations, including favorable phase stability and low opacity at 3 mm, suitable for a large portion of the year. Beyond the core, the array will extend to additional stations across New Mexico, west Texas, eastern Arizona, and northern Mexico. Long-baseline stations will also be located in Hawaii, Washington, California, Iowa, Massachusetts, New Hampshire, Puerto Rico, the U.S. Virgin Islands, and Canada, ensuring wide geographic coverage and exceptional angular resolution (Fig.1.14). All mentioned array configurations are summarized in Tab.1.4 and the predicted performance of the array is shown in Tab.1.5. For further details see Selina et al. (2020) and Murphy et al. (2017). In addition to this extensive baseline network, international collaboration will further enhance the array's capabilities. The upcoming LEVERAGE program (Kadler et al. 2024), for example, plans to introduce new stations in Germany and, eventually, other European countries - and will be discussed in more detail in the following chapter.

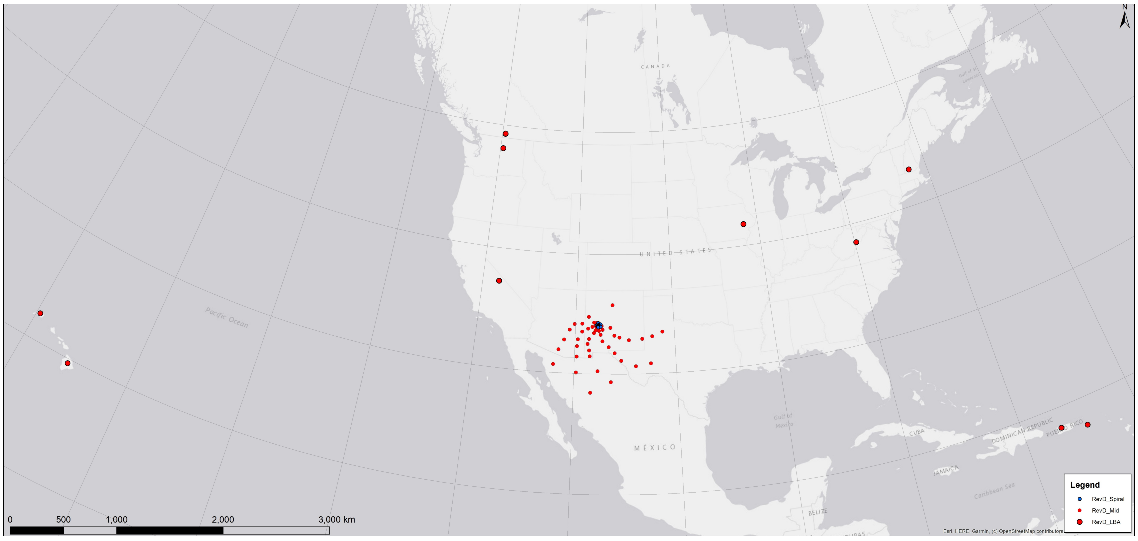

(a) View of the main array, mid stations and the Long Baseline Array stations. Multiple antennas are located at each LBA site

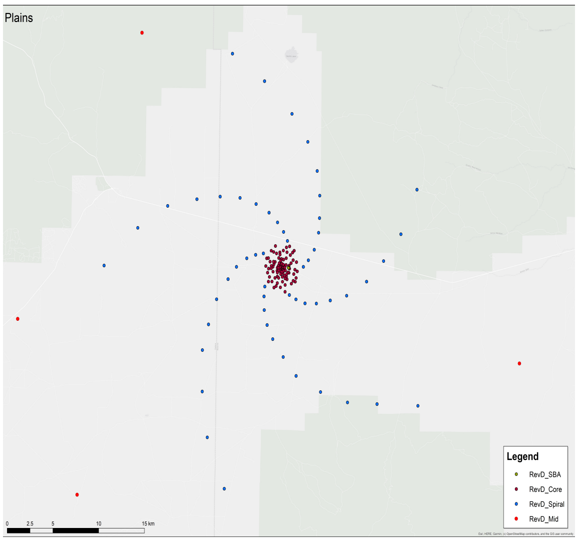

(b) Zoom view of the plains of San Agustin. Dense central core combined with spiral arms (spiral configuration).

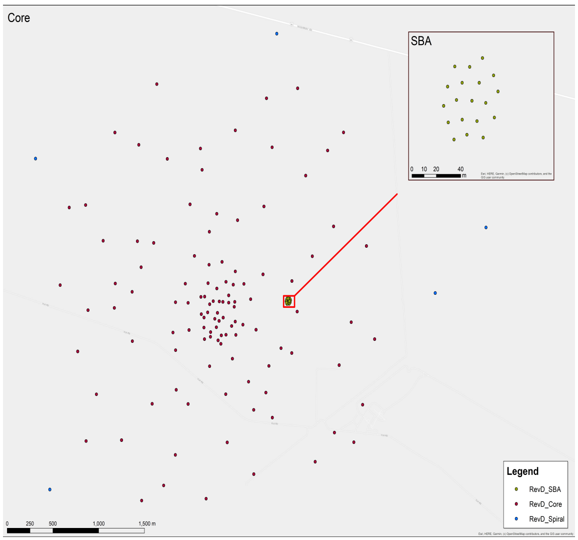

(c) Zoom view of the compact core and the SBA antennas

Figure 1.11: Overview of all stations of the ngVLA. The antenna positions are still preliminary, but serve as a representative basis for performance evaluation and cost estimation.

Array Element	**Aperture Diameter [m]**	**Quantity**	**B_{MIN} [m]**	**B_{MAX} [km]**
Long Baseline Array	18	30	32.6	8856
Main Interferometric Array	18	214	30.6	1005
Short Baseline Array	6	19	11.0	0.06

Table 1.4: Summary of ngVLA Array Elements

Center Frequency [GHz]	2.4	8	16	27	41	93
Band Lower Frequency [GHz]	1.2	3.5	12.3	20.5	30.5	70.0
Band Upper Frequency [GHz]	3.5	12.3	20.5	34.0	50.5	116.0
Field of View FWHM [arcmin]	24.3	7.3	3.6	2.2	1.4	0.6
Aperture Efficiency	0.77	0.76	0.87	0.85	0.81	0.58
Effective Area A_{eff} [$\times 10^3$ m^2]	47.8	47.1	53.8	52.6	50.4	36.0
System Temp T_{sys} [K]	25	27	28	35	56	103
Max Inst. Bandwidth [GHz]	2.3	8.8	8.2	13.5	20.0	20.0
Sampler Resolution [bits]	8	8	8	8	8	4
Antenna SEFD [Jy]	372.3	419.1	372.1	485.1	809.0	2080.5
Resolution of Max. Baseline [mas]	2.91	0.87	0.44	0.26	0.17	0.07
Continuum rms, 1 hr [μJy/beam]	0.38	0.22	0.20	0.21	0.28	0.73
Line Width, 10 km/s [kHz]	80.1	266.9	533.7	900.6	1367.6	3102.1
Line rms, 1 hr, 10 km/s [μJy/beam]	65.0	40.1	25.2	25.2	34.2	58.3

Table 1.5: ngVLA Key Performance Metrics

1.5.3 The LEVERAGE Program

Long-baseline Extension in next-generation VLBI Experiments and Rapid-response Array Germany (LEVERAGE) is a proposed network of mid-to-high-frequency antennas in Germany, with potential expansions across Europe. This array will consist of multiple antenna clusters, with distances of several hundred kilometers between them. Operating in the mid-frequency range, between 1.2 GHz and 15.3 GHz, LEVERAGE has the potential to create strong synergies with the ngVLA and SKA, particularly the SKA-mid. The dual-purpose role of LEVERAGE involves complementing the ngVLA and SKA-VLBI networks, while also functioning as an independent facility for transient studies and other scientific applications. This will enhance Europe's capabilities in multimessenger astronomy. The primary goal of the LEVERAGE concept is to foster scientific collaboration between VLBI arrays, improving image reconstruction precision at sub-milliarcsecond scales, and providing rapid-response capabilities for transient events. For more details on

the European VLBI science vision, see Venturi et al. (2020). LEVERAGE significantly enhances the (u, v) coverage beyond 5000 km in the ngVLA Long subarray. For SKA-VLBI, LEVERAGE complements the European VLBI Network (EVN) and establishes connections with African telescopes, thereby improving image fidelity for observations up to 15 GHz. LEVERAGE will play a crucial role in providing high-precision astrometric measurements and enabling advanced imaging of transient phenomena in the northern sky (Sokolovsky et al. 2018). Further details will be presented in an upcoming publication by Kadler et al. (in preparation).
The exact location of the German stations has not yet been finalized, but one potential site has already been identified. The Wetterstein Millimeter Telescope (WMT) is a planned radio telescope linked to the Environmental Research Station Schneefernerhaus (UFS), located at 2,650 meters above sea level near the summit of the Zugspitze, Germany's highest mountain. The site's coordinates are 47°24'59.8" N, 10°58'46.5" E. A site-selection study is underway to determine the best location near the UFS. The WMT will be a state-of-the-art telescope, serving as Germany's flagship contribution to the ngVLA and European VLBI networks. As part of the LEVERAGE program, it will enhance global coverage, especially in east-west baselines with North America and north-south baselines with Africa. Looking ahead into the era of the full ngVLA and SKA, the LEVERAGE and WMT projects are well aligned with the broad scientific interests of the German astronomical community (Kadler et al. 2024), supporting high-profile research areas:

- **Stellar Astrophysics:** Stellar remnants as compact radio sources.
- **Solar System, Planetary Systems and Habitability:** For example, small solar system bodies, planetary atmospheres, star and planet formation.
- **Circuit of Cosmic Matter:** Such as star formation and galaxy evolution.
- **The Galaxy and the Local Group:** For example, Galactic structure, Galactic center, interstellar nebulae.
- **Galaxies and AGN:** Including black holes and relativistic jets, gas distribution and dynamics in galaxies across distance scales, starburst galaxies, and magnetic fields.
- **Cosmology:** For example, megamasers, dark matter, and cosmological parameters.
- **Extreme Conditions in the Cosmos and Fundamental Astrophysics:** Including high-energy astrophysics, compact objects, and multimessenger astronomy (electromagnetic counterparts to cosmic neutrinos and gravitational wave events).

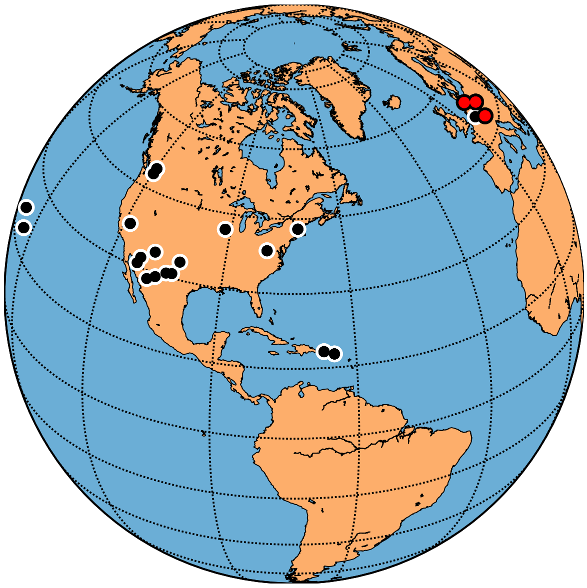

Figure 1.12: ngVLA stations plus additional german antennas of the LEVERAGE programm

1.5.4 VLBA

The VLBA (Very Long Baseline Array) consists of ten identical 25-meter antennas spread across the United States, with baseline lengths ranging from 200 km to transcontinental distances of up to 8,600 km. To illustrate, the longest baseline extends between Mauna Kea, Hawaii, and St. Croix, Virgin Islands. One key scientific application of the VLBA is the long-term MOJAVE program (Monitoring Of Jets in Active galactic nuclei with VLBA Experiments), which focuses on observing AGN jets in the northern sky at frequencies of 15 GHz, 23 GHz, and 43 GHz. According to the MOJAVE team, the main goals of the program are to provide significantly improved image resolution, size, and statistical completeness compared to previous surveys, and to analyze the temporal behavior of jet kinematics and polarization—particularly how these properties relate to other source characteristics.

The complete MOJAVE sample, which has grown since its inception in 1994 (most recently with the "MOJAVE 1.5 Jy Quarter Century Sample" by Lister et al. (2019)), includes 409 AGNs observed at 15 GHz with the VLBA between 1994 and 2019. This dataset represents the largest and most complete radio-loud blazar sample to date, covering approximately 75% of the entire sky. The selection criterion for inclusion is a total 15 GHz VLBA flux density exceeding 1.5 Jy at any epoch between 1994.0 and 2019.0.

The VLBA stations involved in the imaging process include FD (Fort Davis), PT (Pie Town), LA (Los Alamos), KP (Kitt Peak), MK (Mauna Kea), BR (Brewster), NL (North Liberty), and OV (Owens Valley). Since the reconstructions in this thesis will be done with 15 GHz, 43 GHz and 94 GHz, the stations at HN (Hancock) and SC (St. Croix) do not participate in the reconstruction process, since they are located in more humid environments and are not equipped with 3 mm receivers, which are needed for the 94 GHz observations. The performance estimates are shown in Tab.1.6 [6]

Parameter	**Value**
Number of Dishes	10
Dish Size	25 meters (82 feet)
Antenna Weight	∼218 tons
Total Collecting Area	19,635 square meters
Receiver Frequencies	0.3 GHz – 96 GHz (90 cm – 3 mm)
Resolution	0.17 – 22 milliarcseconds
Array Size	Maximum baseline of 8,611 km (5,350 mi)
Bandwidth	128 MHz

Table 1.6: Very Long Baseline Array (VLBA) Specifications

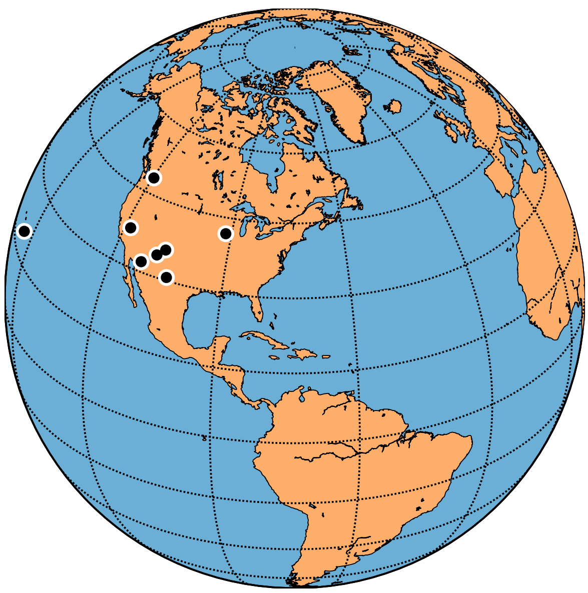

Figure 1.13: VLBA stations on Earth.

1.5.5 GMVA

The Global Millimeter VLBI Array (GMVA) is an international collaboration of radio observatories dedicated to performing very long baseline interferometry (VLBI) at mil-

[6] https://public.nrao.edu/telescopes/vlba/

limeter wavelengths, primarily at 86 GHz (3.5 mm). By linking radio telescopes across Europe, North America, and occasionally other regions such as Greenland or Korea, the GMVA forms an intercontinental array capable of achieving angular resolutions of up to 45 microarcseconds with typical single baseline detection thresholds of 50-200 mJy. This resolution enables detailed imaging of AGNs, relativistic jets, and the environments of supermassive black holes. The GMVA complements shorter-wavelength arrays like the Event Horizon Telescope (EHT) by offering higher sensitivity and longer observing sessions, making it particularly valuable for time-domain studies. Operated through a collaborative and open-access framework, the GMVA issues regular proposal calls and plays a key role in advancing our understanding of some of the most extreme environments in the universe. The array performance is summarized in Tab.1.7 [7]

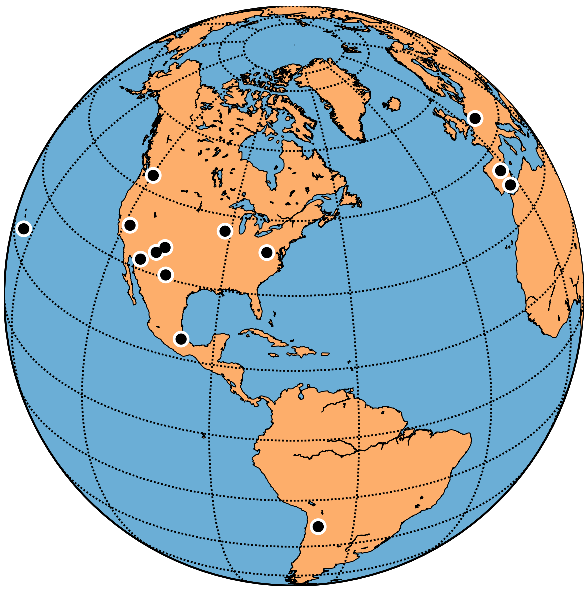

Figure 1.14: GMVA stations on Earth.

[7]https://www3.mpifr-bonn.mpg.de/div/vlbi/globalmm/

Station	Diameter (m)	Tsys (K)	Gain (K/Jy)	Eta (%)	SEFD (Jy)
GBT	100.0	130.0	0.98	35	133
Effelsberg	80.0 (eff.)	140.0	0.14	7.7	1000
Noema	46.2 (eff.)	70.0	0.42	70	163
Pico Veleta	30.0	100.0	0.15	60	654
Yebes	40.0	100.0	0.10	22	990
VLBA (8x25m)	25.0	115.0	0.028	16	4100
KVN (3x21m)	21.0	150.0	0.05	40	3000
Onsala	20.0	130.0	0.049	43	2650
Metsähovi	14.0	150.0	0.010	18	15000
LMT (prelim)	50.0	200.0	0.39	55	513
GLT	12.0	170.0	0.032	78	5312
ALMA	71.1 (eff.)	70.0	1.02	71	69

Table 1.7: Station Parameters at 86 GHz

1.6 Maximum Entropy Method (MEM)

In MEM, the goal is to maximize an objective function that balances how well the model matches the data and how much it aligns with prior information:

$$J = S(\mathbf{I}', \mathbf{B}) - \alpha(\chi^2(\mathbf{I}') - 1) \tag{1.6.1}$$

for a n^2 pixel test image $\mathbf{I}'$, a prior/bias image $\mathbf{B}$, and an array of N measured visibilities V. In this formulation, $S(\mathbf{I}', \mathbf{B})$ is the chosen regularization or entropy function, while χ^2 is the goodness-of-fit statistic that compares the visibilities of the test image $\mathbf{I}'$ to the observed data. All arrays of image pixels or visibilities are denoted in bold. The parameter α serves as a mixing coefficient that balances the relative contributions of the regularizer (entropy term) and the data fit (the χ^2 term). In practice, α can either be fixed, manually adjusted, or allowed to vary during the maximization process (Chael et al. 2016).
The standard entropy function, based on information theory (Cornwell & Evans 1985), is given by:

$$S(\mathbf{I}', \mathbf{B}) = -\sum_{i=1}^{n^2} I_i' \log\left(\frac{I_i'}{B_i}\right) \tag{1.6.2}$$

.
However, it has been shown that for any convex function $S(\mathbf{I}', \mathbf{B})$ of the I_i, the reconstruction process is guaranteed to converge (Ramesh & Nityananda 1986). Therefore, many different functions can be used. For example: $S(\mathbf{I}') = \sum \log(I_i')$, $S(\mathbf{I}') = \sum \sqrt{I_i'}$,

the ℓ_1 norm $S(\mathbf{I}') = \sum |I'_i|$ or the total variation function (TV) as a regularizer:

$$TV(\mathbf{X}) = \sum_{i=1}^{n} \sum_{j=1}^{n} \sqrt{|X_{i+1,j} - X_{i,j}|^2 + |X_{i,j+1} - X_{i,j}|^2} \tag{1.6.3}$$

where $\mathbf{X}$ is a complex image matrix. TV helps maintain edges while smoothing out noise. It is especially useful in problems where you want to preserve sharp transitions (like edges) but suppress random fluctuations (like noise) (Chael et al. 2016), whereas ℓ_1, for example, promotes sparsity in the image, making it useful when only a few significant features are expected (Honma et al. 2014). The data to be fitted consist of visibility amplitudes and closure phases, so in this case the goodness-of-fit χ^2 term can be written as:

$$\chi^2 = \sum_{i=1}^{N} \frac{(|V_i| - |V_{i,m}(\mathbf{I}')|)^2}{\sigma_{A_i}^2} + \sum_{i=1}^{N_c} \frac{(\phi_{c_i} - \phi_{mc_i}(\mathbf{I}'))^2}{\sigma_{c_i}^2} \tag{1.6.4}$$

where $\sigma_{A_i}^2$ and $\sigma_{c_i}^2$ are the measurement variances on the closure amplitudes and closure phases, respectively (Thompson et al. 2017). For a perfect fit, the χ^2 value should be close to unity, indicating that the residuals between the model and the data are on the same order as the measurement uncertainties. Strong deviations from $\chi^2 = 1$ indicate that the model is not correctly parametrized or that the estimates of errors are not correct.

1.7 Jet physics

1.7.1 Jet formation

Blazars exhibit powerful relativistic jets that transport energetic plasma from the vicinity of the supermassive black hole (SMBH) out to distances of hundreds of kiloparsecs. The precise mechanism behind jet formation is still not well understood, but the current models are primarily based on relativistic magnetohydrodynamics (RMHD).

One prominent model is the **Blandford – Znajek** (**BZ**) mechanism (Blandford & Znajek 1977), in which the jet is powered by the rotational energy of a spinning (Kerr) black hole. In this model, magnetic fields from the accretion disk surround the black hole and create a magnetosphere around its rotating region (the so-called ergosphere) which can be described by the Grad-Shafranov equation (Camenzind 2007). Plasma in this region interacts with the magnetic field, enabling the extraction of rotational energy and launching a relativistic jet along the spin axis.

An alternative model is the **Blandford – Payne** (**BP**) mechanism (Blandford & Payne 1982), where jets are driven by the rotational motion of a magnetized accretion disk. Here, plasma is accelerated along magnetic field lines anchored in the disk, launching

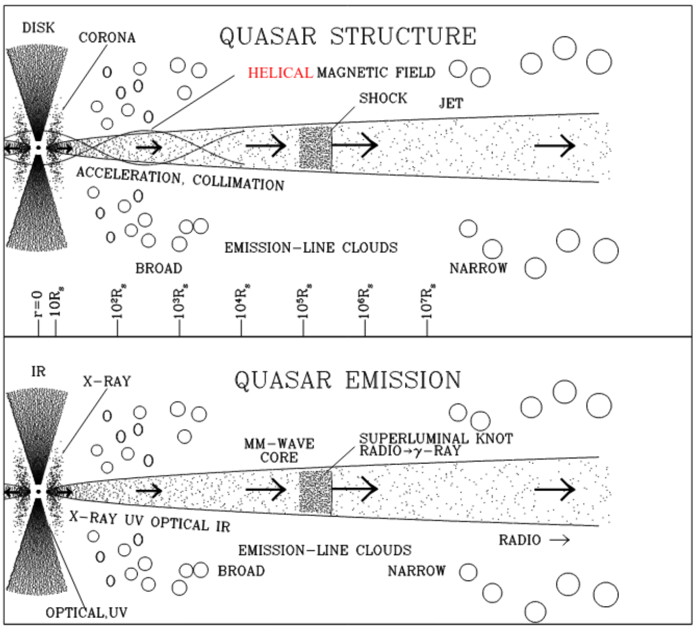

Figure 1.15: Illustration of the above mentioned calculations to derive the apparent velocity. Taken from Marscher (2009)

material outward.
The structure of jets in radio-loud AGNs, including their emission properties, can be investigated through Very Long Baseline Interferometry (VLBI). These observations reveal distinct jet features: the radio core, quasi-stationary components, and superluminally moving knots (Marscher 2009). Quasi-stationary features often appear fixed or moving at subluminal apparent speeds and may be the result of recollimation shocks, jet bending, or interactions with interstellar material. In contrast, superluminal components are typically interpreted as propagating shock waves, generated when the plasma's velocity or energy density increases suddenly near the jet base.

1.7.2 Superluminal motion

One of the first results after the implementation of VLBI in radio astronomy in the late 1960s and early 1970s, was that some AGNs consisted of more than one component. These components seem to move with superluminal speeds (speeds higher than the speed of light), which seem to be unphysical. By means of the model of Rees (1966), it will be shown that **superluminal motion** can be explained as an optical illusion caused by an object moving partly in the direction of the observer. This section is based on Kembhavi & Narlikar (1999) and Carroll & Ostlie (2017) if not mentioned otherwise. Imagine a relativistic jet moves with speed v (actual speed of the source) towards an observer at point O as illustrated in Fig.1.16. At time t_1 a signal is emitted from point A. At time

$t_2 = t_1 + \Delta t$ a second signal is emitted from point B. The signals arrive at the observer at t'_1 and t'_2. The angle ϕ is small enough that the two luminosity distances named D_L are approximately the same. The first signal reaches the observer after $t'_1 = t_1 + \frac{D_L + v\Delta t cos\theta}{c}$. The second arrives at $t'_2 = t_2 + \frac{D_L}{c}$. The time between the reception of the two signals is therefore:

$$\Delta t' = t'_2 - t'_1 = t_2 - t_1 - \frac{v\Delta t \cos\theta}{c} = \Delta t(1 - \beta\cos\theta) \tag{1.7.1}$$

with $\beta = \frac{v}{c}$, which is shorter than Δt. Considering that:

$$BC = D_L \sin\phi \approx \phi D_L = v\Delta t \sin\theta \tag{1.7.2}$$

$$\phi D_L = v \sin\theta \frac{\Delta t'}{1 - \beta\cos\theta} \tag{1.7.3}$$

The apparent transverse speed measured at the point O is:

$$v_{app} = \frac{\phi D_L}{\Delta t'} = \frac{v sin\theta}{1 - \beta\cos\theta} \tag{1.7.4}$$

which leads to superluminal motion for large β and small θ. v_{app} can be rewritten to:

$$\beta_{app} = \frac{v_{app}}{c} = \frac{\beta\sin\theta}{1 - \beta\cos\theta} \tag{1.7.5}$$

Whenever a signal moves with relativistic speed ($\gamma >> 1$) the **relativistic beaming effect**, which was discussed in Sect. [1.3.1] becomes important. It has an affect on the morphology of an AGN, since because of this effect a two-sided source can appear one-sided. This became clear when one considers that if S_ν is the flux density, then S_ν/ν^3 is invariant under Lorentz transformation see (Rybicki & Lightman 1979). Since $S_\nu \propto I(\nu)$ the observed intensity of a moving jet component which follow a power law ($I(\nu) = A\nu^\alpha$) reads:

$$I(\nu_{obs}) = \delta^3 A\nu_{emit}^\alpha = \delta^3 A\delta^{-\alpha}\nu_{obs}^\alpha \tag{1.7.6}$$

which can be rewritten into:

$$I(\nu_{obs}) = \delta^{3-\alpha} I(\nu_{emit}) \tag{1.7.7}$$

where δ is the so-called relativistic Doppler factor:

$$\delta = \frac{\sqrt{(1 - \beta^2}}{1 - \beta\cos(\theta)} \tag{1.7.8}$$

.

So if one combines Eq.1.7.8 and Eq.1.7.7 one obtains for the ratio of the observed fluxes:

$$\frac{S_{\text{jet}}}{S_{\text{counter}}} = \left(\frac{1 + \beta\cos\phi}{1 - \beta\cos\phi}\right)^p \tag{1.7.9}$$

where $p = (3 - \alpha)$ for observations of multiple components and $p = (2 - \alpha)$ for observations of jets which can be expressed as a series of components.

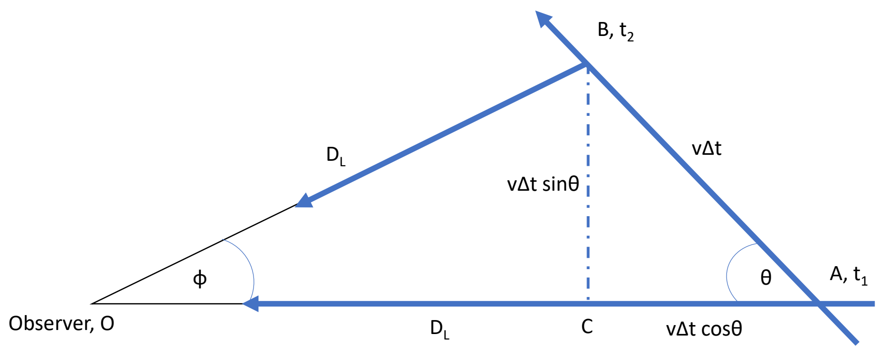

Figure 1.16: Illustration of the above mentioned calculations to derive the apparent velocity.

1.8 RMHD jet instabilities

One of the main objectives of this thesis is to investigate the instabilities that develop in jet simulations over time as small perturbations grow from the initial state after launching - as described earlier. To analyze the behavior and underlying physics of these instabilities, the dispersion relation must be derived. The general procedure is as follows: the governing equations presented in Sec.1.2 are linearized using a perturbation ansatz. By decomposing the perturbations into plane waves, these linearized differential equations reduce to a system of linear algebraic equations, from which the dispersion relation can be directly obtained by requiring non-trivial solutions (Bartelmann 2013). For simplicity, the generalized dispersion relation for e.g. a two-fluid interface with a magnetic field, which allows one to analyze instabilities like Kelvin-Helmholtz or Rayleigh-Taylor - is adopted from Mizuno's lectures on plasma physics [8], allowing the main physical properties to be discussed. A more rigorous analysis, which also includes relativistic effects, can be performed using spectral theory (see Goedbloed et al. (2019)). So when

[8] https://web.tdli.sjtu.edu.cn/mizuno/astrophysical-hydrodynamics/

talking about a two-layer interface, one can consider a boundary situated at $z = 0$ separating two perfectly conducting plasmas, labeled with superscripts (1) and (2), with the gravitational force acting in the $-z$ direction and a magnetic field parallel to the boundary along the x-axis. In this simplified case, it is assumed that the unperturbed (initial) state is steady (time-independent), with the density, velocity, magnetic field, and pressure given by $\rho = \rho_0$, $\mathbf{v} = (v_0, 0,)$, $\mathbf{B} = (B_0, 0, 0)$ and $p = p_0$, respectively. For this configuration, the dispersion relation for the two-plasma interface is given by:

$$\left(\rho_0^{(1)} + \rho_0^{(2)}\right)\omega^2 - 2k\left(\rho_0^{(1)}v_0^{(1)} + \rho_0^{(2)}v_0^{(2)}\right)\omega + k^2\left(\rho_0^{(1)}v_0^{(1)2} + \rho_0^{(2)}v_0^{(2)2}\right) - \frac{2k^2B_0^2}{\mu_0} + kg\left(\rho_0^{(1)} - \rho_0^{(2)}\right) = 0 \tag{1.8.1}$$

1.8.1 Rayleigh-Taylor instability (RTI)

If there is no velocity shear, meaning $v_0^{(1)} = v_0^{(1)} = 0$ and the perturbation behaves like $\propto \exp(i(k_X x + k_y y - \omega t))$, the dispersion relation simplifies to:

$$\omega^2 = -gk\frac{\rho_0^{(1)} - \rho_0^{(2)}}{\rho_0^{(1)} + \rho_0^{(2)}} + \frac{2B_0^2k_x^2}{\mu_0\left(\rho_0^{(1)} + \rho_0^{(2)}\right)} \tag{1.8.2}$$

This shows that, in the absence of magnetic fields, the system becomes unstable ($\omega^2 < 0$) if a heavier plasma is resting on top of a lighter one ($\rho_0^{(1)} > \rho_0^{(2)}$). This is the so-called **Rayleigh – Taylor instability** (RTI). When a displacement occurs at the boundary, the lighter plasma pushed upward experiences buoyancy and continues to rise, while the denser plasma pushed downward feels a stronger gravitational force and continues to sink, leading to the mixing of the two layers. For perturbations uniform along the field direction ($k_x = 0$) the magnetic field has no effect on stability. In contrast, perturbations purely along the field $k_y = 0, k_x = k$ are stabilized by the magnetic tension force, as indicated by the second term in Eq. 1.8.2. If the condition that a heavier plasma is on top of a lighter one is satisfied, the interface is unstable for wavelengths where $0 < k < k_c$ with the critical wavenumber given by:

$$\boxed{k_c = \frac{(\rho_0^{(1)} - \rho_0^{(2)})g\mu_0}{2B_0^2}} \tag{1.8.3}$$

1.8.2 Kelvin-Helmholtz instability (KHI)

Another case arises when there is velocity shear at the boundary ($v_0^{(1)} \neq v_0^{(1)}$) without gravity force. In this situation, displacements at the interface bend the plasma flowing parallel to the boundary, inducing a centrifugal force that amplifies the deformation and leads to mixing. This is the so-called **Kelvin – Helmholtz instability** (KHI). In a uniform magnetic field without gravitational force, the interface is unstable when

$$\boxed{v_A^2 < \frac{\rho_0^{(1)}\rho_0^{(2)}}{\left(\rho_0^{(1)} + \rho_0^{(2)}\right)^2}\left(v_0^{(1)} - v_0^{(2)}\right)^2} \tag{1.8.4}$$

where the Alfvén speed v_A is given by:

$$v_A^2 = \frac{2B_0^2}{\mu_0\left(\rho_0^{(1)} + \rho_0^{(2)}\right)}. \tag{1.8.5}$$

In the absence of both magnetic fields and gravity, all wavelengths become unstable as long as there is a velocity difference between the two layers ($v_0^{(1)} \neq v_0^{(2)}$).

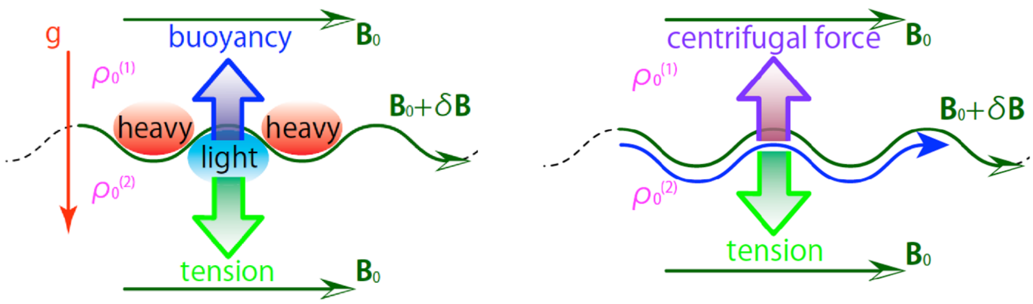

RT instability due to density stratification.

KH instability due to velocity shear.

Figure 1.17: Schematic overwiev of the RT and KH instability.

1.8.3 Current-driven kink instability (kink)

Having discussed the Rayleigh-Taylor and Kelvin-Helmholtz instabilities, which are primarily driven by density stratification and velocity shear at interfaces, it is important to turn to another class of instabilities that plays a crucial role in the dynamics of magnetized jets. In particular, when strong magnetic fields are present, current-driven instabilities (CDIs) become relevant. Among these, the kink instability is of special interest, as it can significantly distort the jet structure by displacing the plasma column in a helical fashion. Unlike the KH and RT instabilities, which are essentially surface instabilities, the kink instability develops in the bulk of the plasma column and is closely linked to the configuration of the magnetic field, especially the presence of a toroidal (azimuthal) component. This makes the kink instability a key mechanism in understanding the stability and eventual disruption of astrophysical jets. Consider a linear pinched discharge, which is a plasma confinement configuration where an

electric current is driven through a plasma column, and the resulting self-generated magnetic field pinches or compresses the plasma radially inward - similar to a jet. A perturbation of the kink mode in this configuration leads to increased magnetic pressure inside the kinked plasma column, while simultaneously reducing the magnetic pressure outside. This enhances the perturbation, allowing the instability to grow.
The stability criterion for the kink mode is given by the Kruskal-Shafranov criterion:

$$\boxed{\frac{B_\phi^2}{B_z^2} < (ka)^2 = \left(\frac{2\pi a}{\lambda}\right)^2} \qquad (1.8.6)$$

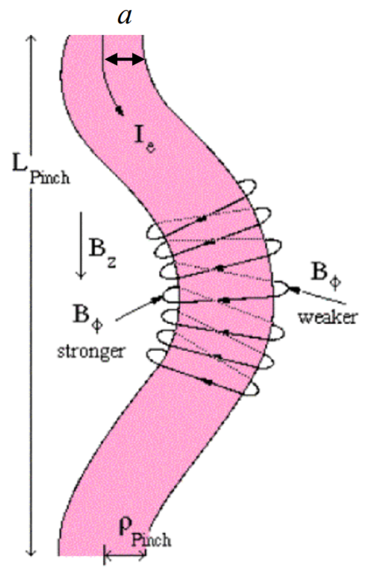

Figure 1.18: Perturbation of the linear pinched discharge with developing kink instabilities due to toroidal magnetic field according to the Kruskal-Shafranov criterion.

2 Simulation

2.1 2D simulation results and discussion

First, 2D axisymmetric time-dependent simulations using the relativistic AMRVAC code were executed (underlying equations are given in Sec.1.2). The motivation behind this is twofold: on the one hand, these simulations represent the first exploration of the topic, and on the other hand, they highlight the importance of 3D simulations by demonstrating the limitations of such 2D models, especially regarding jet instabilities. The simulated jet is based on a spine-sheath model (see Fig.2.1) according to Komissarov (1999). The jet is magnetized with a non-negligibly small rest mass density of its particles. Its structure at the injection is that of a cylindrical jet in magnetostatic equilibrium following the force balance equation:

$$\frac{dp_t}{dr} + \frac{b_\phi}{r}\frac{drb^\phi}{dr} = 0 \tag{2.1.1}$$

where $b^\phi = B^\phi/\Gamma$ is the azimuthal component of the magnetic field as measured in the fluid frame using normalized basis and p_t is the sum of the gas pressure and the magnetic pressure due to the axial magnetic field B_z. There are infinitely many solutions, one of them is according to Komissarov (1999):

$$b^\phi(r) = \begin{cases} b_m(r/r_m), & ;\, r < r_m \\ b_m(r_m/r) & ;\, r_m < r < r_j \\ 0 & ;\, r > r_j \end{cases} \tag{2.1.2}$$

$$p_t(r) = \begin{cases} p_0[\alpha + \frac{2}{\beta_m}(1-(r/r_m)^2)], & ;\, r < r_m \\ \alpha p_0, & ;\, r_m < r < r_j \\ p_0 & ;\, r > r_j \end{cases} \tag{2.1.3}$$

where $\beta_m = \frac{2p_0}{b_m^2}$ and $\alpha = 1 - (1/\beta_m)(r_m/r_j)^2$ with r_j as the jet radius or sheath and r_m is the radius of its core or spine (see spine-sheath-jet model in Fig.2.1). The parameters for the overpressured model are given in Tab.2.1.

As shown in Fig.2.2, which presents slice plots in the x-z plane for the overpressured model — including density, pressure, velocity, and magnetization — only the Kelvin-Helmholtz instability is observed. This instability arises due to the different velocities and densities between the jet and the ambient medium (see the density and velocity plots in Fig. 2.2a) and Fig.2.2c) . The jet is faster and less dense than the ambient medium, so

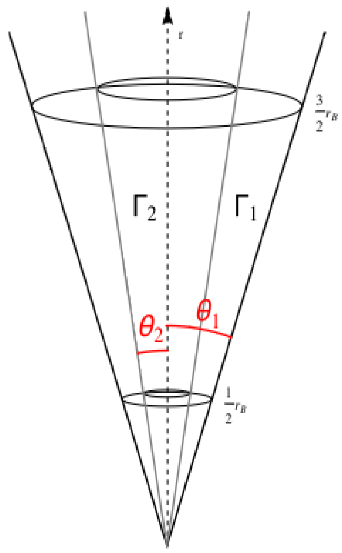

Figure 2.1: Spine-sheath-jet model. Here with r_1 as the radius of the sheath and r_2 as the radius of the spine and θ_1 and θ_2 as its according opening angles. Taken from Sikora et al. (2016)

model	Γ	$\rho_{ambient}$	ρ_{jet}	r_{sheath}	r_{spine}	v_{jet}	$\frac{p_{jet}}{p_{ambient}}$	b_m	β_m
overpressured	4/3	1	0.1	1	0.17	0.85	2.5	0.25	0.80

Table 2.1: Parameters for the spine-sheath overpressured jet model.

the velocity difference between the two layers creates shear at their interface. The faster-moving jet tends to pull on the slower-moving ambient layer, while the slower-moving layer exerts a drag force on the jet. This interaction generates shear at the interface, leading to variations in pressure (see the pressure plot in Fig.2.2b) and velocity along the boundary between the jet and the ambient medium.

If the velocity difference is sufficiently strong and the shear is steep, small perturbations (ripples or waves) can develop at the interface due to these variations. These initial perturbations grow over time because of the persistent velocity difference between the two layers. The faster-moving jet pushes into the slower-moving ambient medium, causing the perturbations to elongate and amplify. This amplification process continues, leading to the development of larger and more pronounced waves along the interface.

The recollimation shocks occur periodically until approximately $t = 60$ in units of R_j/c. After this point, the jet head slows down as it loses momentum to the ambient medium. CD and RT instabilities are not observed in this setup due to the confinement to two dimensions. In this 2D configuration, the magnetic field in the axial direction stabilizes these instabilities, preventing them from evolving. For further discussions on jet instabilities in 2D cases, see Hu et al. (2025).

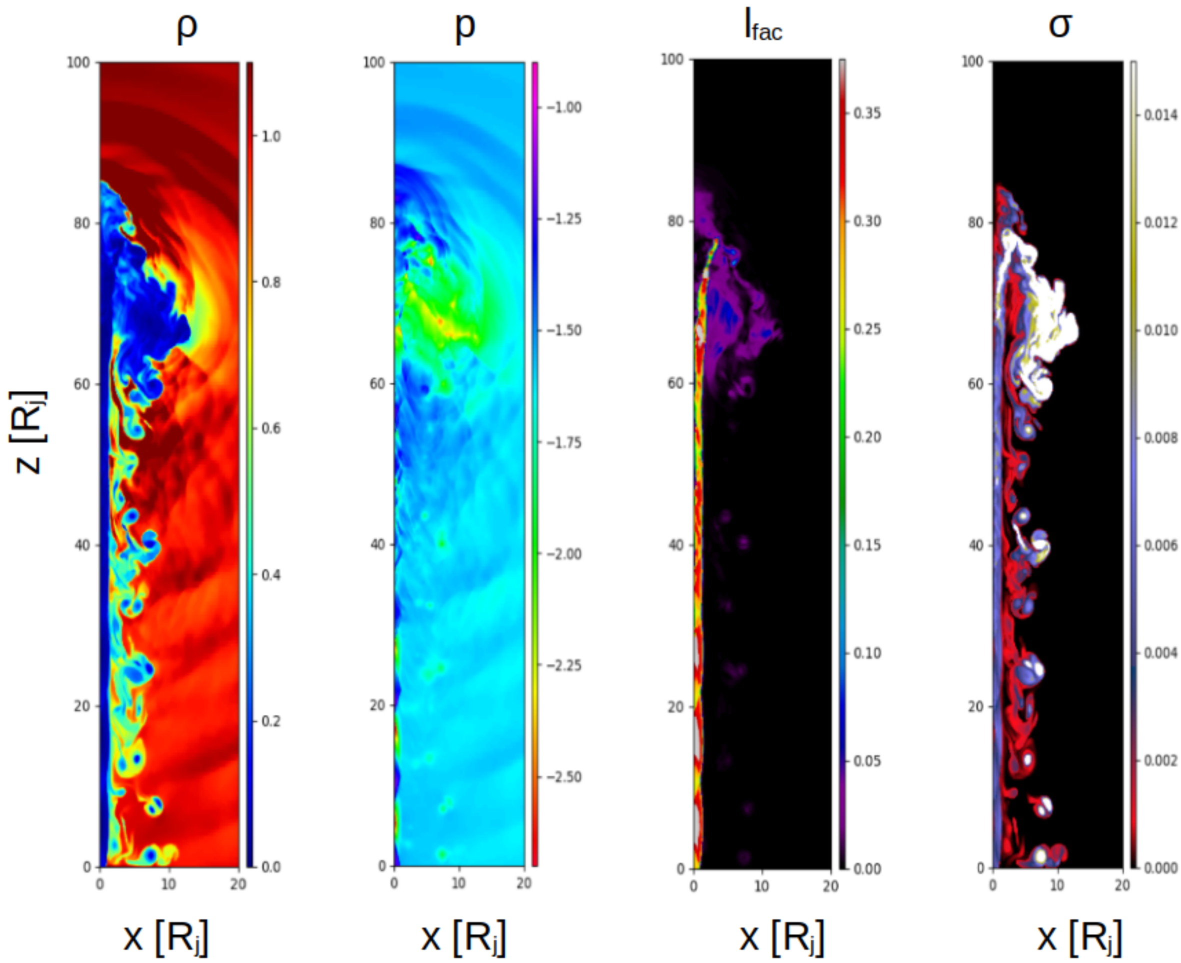

Figure 2.2: 2D overpressured model in linear scale - from left to right - a) density ρ, b) pressure p, c) velocity l_{fac}, d) magnetization σ of the model.

2.2 Numerical setup 3D simulations

In this thesis, the solutions of a time-dependent relativistic magnetized axisymmetric overpressured jet propagating through an unmagnetized ambient medium are required. For this, 3D relativistic magnetohydrodynamic simulations were conducted, where the set of RMHD equations which was presented in Sec.1.2 was solved by means of the Black Hole Accretion Code (BHAC) (Porth et al. 2017). The general numerical setup is shown in Tab.2.2. The code's internal units will be used for the simulation, which are defined in terms of the jet radius R_j, the rest-mass density of the ambient medium at the jet nozzle ρ_a, and the speed of light c. Later on, physical values for R_j and ρ_a will be provided in CGS units. The pressure is given in units of $\rho_a c^2$, the time is measured in units of R_j/c, the rest-mass density in the jet ρ_j is expressed in units of the ambient rest-mass density, and the magnetic field B is given in units of $\sqrt{4\pi\rho_a c^2}$. Both the jet

Parameter name	Parameter value
Frame	3D Cartesian
Riemann Solver	HLL
Divergence controll	Constrained Transport (uct2)
Reconstruction	Piecewise parabolic method
Adiabatic index (γ)	4/3
Jet core radius (r_m)	0.27
Jet Lorentz factor (Γ_j)	6.0
Jet plasma-beta (β_m)	2.5
Magnetic field (B_m)	0.055
Magnetic pitch (k_m)	0.1
Jet over-pressure (d_k)	1.5
Jet density (ρ_j)	1.0×10^{-3}
Jet opening angle (ϕ_j)	0.1
Ambient gradient (κ)	1.5
Ambient core radius (r_c)	10.0
Shear layer width (w_{shear})	1.0×10^{-3}
Lorentz factor damping (δ)	8.0
Domain (x,y,z)	$\pm 20R_j$, $\pm 20R_j$, $200R_j$
Number of cells (N_x, N_y, N_z)	96, 96, 192
time $[R_j/c]$	800

Table 2.2: Setup of the 3D RMHD simulation for the helical model.

and the ambient medium are assumed to behave as a perfect gas, so their adiabatic index is set to $\gamma = 4/3$. As the initial conditions, the solutions of steady, relativistic, magnetized axisymmetric jets were chosen in the form of profiles according to Martí (2015). The profiles are solutions to the transversal equilibrium equation establishing the radial balance between the total pressure gradient, the centrifugal force and the magnetic tension. In case for models without rotation ($v_\phi(r) = 0$) the equilibrium equation reads:

$$\frac{dp}{dr} = -\frac{(B_\phi)^2}{r\Gamma^2} - \frac{B_\phi}{\Gamma^2}\frac{dB_\phi}{dr} \tag{2.2.1}$$

The radial profiles for the density ρ, Lorentz factor Γ and magnetic fields B_ϕ and B_z are fixed, so that one can solve for the gas pressure p. For the density $\rho(r)$ and the Lorentz factor $\Gamma(r)$ top-hat profiles were used.

$$\rho(r) = \begin{cases} \rho_j, & r < r_j \\ \rho_a, & r \geq r_j \end{cases} \tag{2.2.2}$$

$$\Gamma(r) = \begin{cases} \Gamma, & r < r_j \\ 1, & r \geq r_j \end{cases} \tag{2.2.3}$$

The ambient density ρ_a is always set to be 1 (beside $v_a = 0$ and $B_a = 0$). With the given Lorentz profile, the velocity can be computed by means of:

$$v = \sqrt{1 - \frac{1}{\Gamma^2}} \tag{2.2.4}$$

.

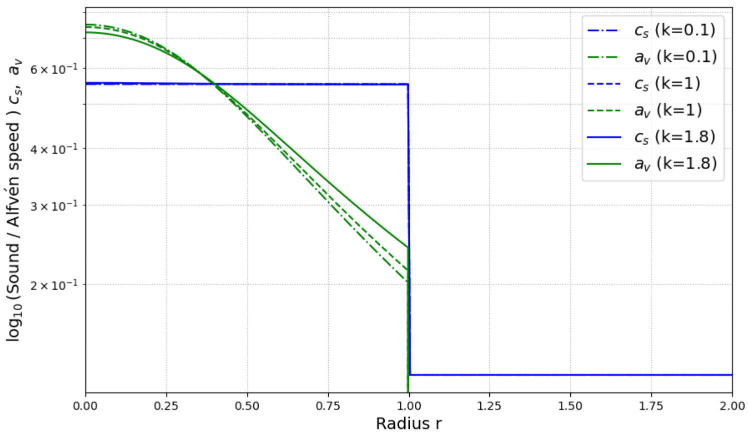

Figure 2.3: Alfvén speed a_v and sound speed c_s profiles for different k values.

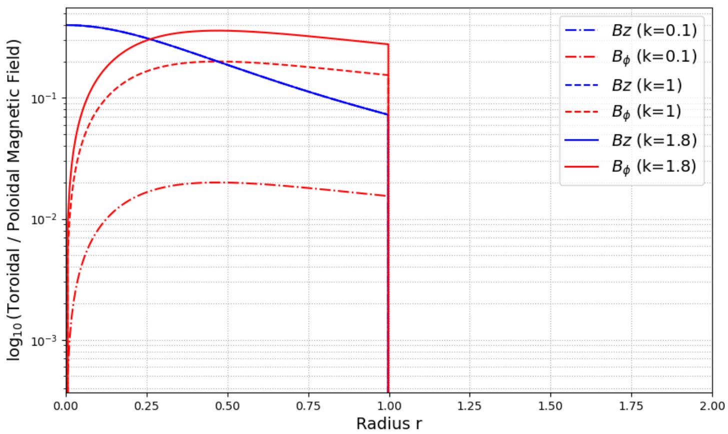

Figure 2.4: B_z (poloidal) and B_ϕ (toroidal) profiles for different k values.

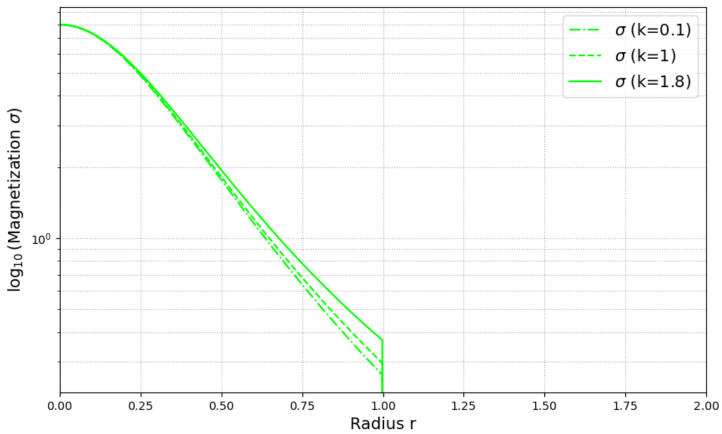

Figure 2.5: Magnetization σ profiles for different k values.

Other characteristic velocities are sound speed

$$c_s = \sqrt{\frac{\gamma p}{\rho + \frac{\gamma}{\gamma - 1} p}}, \tag{2.2.5}$$

which is the maximum speed at which pressure disturbances can travel in a fluid or in other words how quickly the fluid can react to disturbances and Alfvén speed

$$v_A = \sqrt{\frac{B^2}{B^2 + \rho + \frac{\gamma}{\gamma - 1} p}}, \tag{2.2.6}$$

which is the speed at which magnetic disturbances travel through a plasma (both shown in Fig.2.3 for different k values. The k is absorbed by the magnetic fields, see Eq.2.2.9). Where B^2 is the magnetic energy density and is given by:

$$B^2 = \frac{B_\phi^2 + B_z^2}{\Gamma^2} + (v_z B_z)^2. \tag{2.2.7}$$

where $v_z = 0.97$ (according to Martí (2015)). The magnetic energy density divided by twice the density defines the magnetization σ, which determine how strong the plasma is dominated by the magnetic fields and is given by

$$\sigma = \frac{B^2}{2\rho} \tag{2.2.8}$$

The magnetization profiles are shown in Fig.2.5 for different k values. The azimuthal

B_ϕ and axial B_z magnetic fields are given by:

$$B_\phi(r) = \begin{cases} k \cdot \dfrac{b_0\,(r/r_0)}{1+(r/r_0)^2}, & r < r_j \\ 0, & r \geq r_j \end{cases} \tag{2.2.9}$$

$$B_z(r) = \begin{cases} \dfrac{b_0}{1+(r/r_0)^2}, & r < r_j \\ 0, & r \geq r_j \end{cases} \tag{2.2.10}$$

where k, b_0 and r_0 are scaling parameters that define the magnetic field strength and radial structure within the jet. The profiles for the magnetic fields are presented for different k values in Fig.2.4. So with all profiles set, after the integration of Eq.2.2.1 by parts the pressure profile equals

$$p(r) = \begin{cases} \dfrac{1}{2} \cdot \dfrac{(kb_0/\Gamma)^2}{(1+(r/r_0)^2)^2} + \mathrm{C}, & r < r_z \\ p_a, & r \geq r_z \end{cases} \tag{2.2.11}$$

where the constant C equals:

$$\mathrm{C} = d_k p_a - \frac{1}{2}\left(\frac{b_0}{1+(1/r_0)^2}\right)^2 - \frac{(kb_0)^2}{2\Gamma^2(1+(1/r_0)^2)} \tag{2.2.12}$$

where d_k is the jet overpressure factor. The total pressure is given by:

$$p_{\mathrm{tot}}(r) = p(r) + \frac{B^2}{2} \tag{2.2.13}$$

and the ambient pressure is

$$p_{\mathrm{ambient}} = \frac{2p_0}{b_m^2} \tag{2.2.14}$$

where b_m is a scaling factor. In addition, the enthalpy is given by:

$$h = 1 + \frac{p}{\rho(\gamma-1)} + \frac{p}{\rho} \tag{2.2.15}$$

and the density contrast (inertia)

$$\eta_r = \frac{\rho h_{\mathrm{jet}}\Gamma^2}{\rho_{\mathrm{amb}} h_{\mathrm{amb}}} \tag{2.2.16}$$

where

$$h_{\mathrm{jet}} = 1 + \frac{\gamma}{\gamma-1} \cdot \frac{p}{\rho} \tag{2.2.17}$$

and

$$h_{\mathrm{amb}} = 1 + \frac{\gamma}{\gamma - 1} \cdot \frac{p_{\mathrm{amb}}}{\rho_{\mathrm{amb}}}. \tag{2.2.18}$$

With these initial profiles, one can let the jet evolve with time and investigate the eventual occurring instabilities.

2.3 3D simulation results and discussion

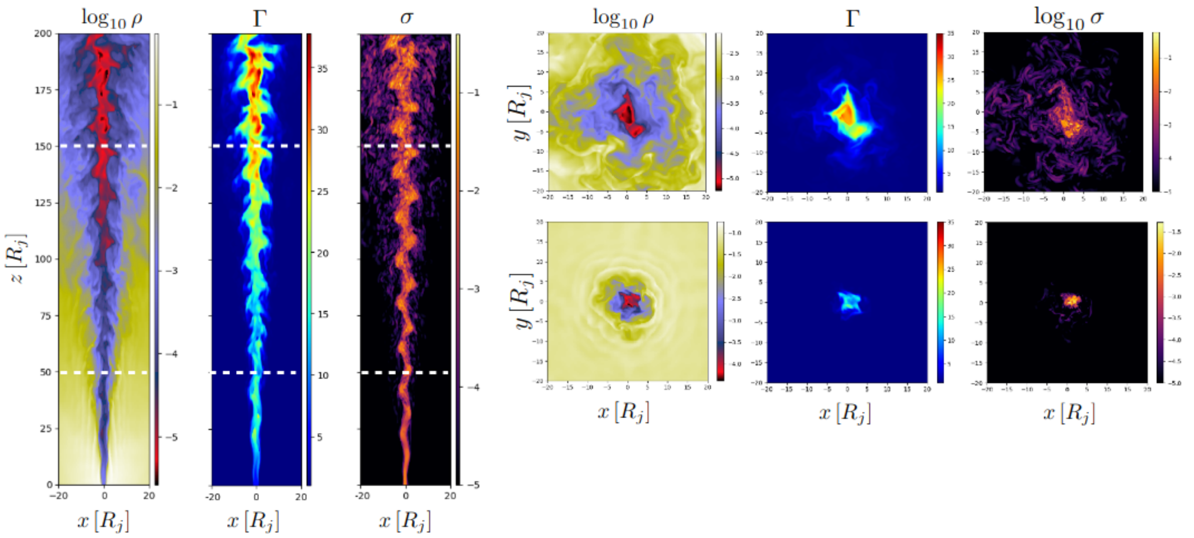

Figure 2.6: Different plane slices of RMHD 3D simulation with corresponding instabilities.

The results of the 3D simulations performed with the settings described in the previous chapters are shown in Fig. 2.6. Similar to the 2D simulations, different slices - of density ρ, Lorentz factor Γ, and magnetization σ in the x-z and x-y planes - are displayed. One of the first findings is that the instabilities observed in the jet are more complex than in 2D. The jet no longer shows a straight shape with periodic behavior as in the 2D case. Instead, multiple time-evolving processes occur. Initially, the onset of the current-driven (CD) kink instability is observed. According to the Kruskal–Shafranov criterion (Eq. 1.8.6), the CD instability depends on the toroidal field, which is strongly present from the start of the jet and thus appears first. The magnetic fields that trigger the kink instabilities also stabilize the jet against other instabilities such as Kelvin–Helmholtz (KH) and Rayleigh–Taylor (RT). Although the toroidal magnetic field B_ϕ is present, the poloidal magnetic field initially dominates and stabilizes the jet against kink instabilities. However, over time, the toroidal magnetic field becomes dominant and twists the jet more strongly, leading to the evolution and amplification of kink instabilities. This twisting exposes the jet to velocity shear, as seen in the different Lorentz factors within the jet (Γ plots in Fig.2.6), leading to the onset of KH instabilities, since the velocity difference

gets larger than the Alfvén speed (stability criterion KH). Initially, the jet is confined by the ambient medium since the jet's density is a priori smaller than the ambient's. As time evolves, the jet accelerates. The appearance and evolution of KH instabilities were already discussed in more detail in the 2D case.
Once the jet is sufficiently distorted by the kink and KH instabilities, it begins to break up, creating regions with density inversions or strong radial pressure gradients that allow RT instabilities to develop. These conditions - with the heavier fluid (cocoon) accelerating against the lighter jet interior - start to appear at roughly $t = 100$, when the jet density becomes lower than that of the outer cocoon. This manifests as finger-like structures. Although the toroidal magnetic field that triggers the kink instability initially stabilizes the KH and RT instabilities, it is possible to capture the full development of these instabilities within the jet if they are allowed to evolve sufficiently to completely distort it. In addition to these instabilities, others such as the Richtmyer–Meshkov instability (RMI) are also likely to arise. The RMI is similar in structure to the RT instability but is triggered through impulsive shocks rather than continuous gravity acting on the fluids (Hu et al. 2025). Another possibility would be the current-driven filamentary instability (CFI), but according to Matsumoto et al. (2021), when the jet magnetization σ becomes larger than 0.01, the CFI is stabilized. Since in the presented model the magnetization is always higher, this instability can be excluded. Regarding collimation, one can see that the initially collimated jet remains more or less collimated at the timestep $t = 50$. However, it becomes increasingly distorted by the instabilities, as shown in the upper panel of the x-y slice at $t = 150$. A snapshot rendering of the jet with all the mentioned instabilities is given in Fig. 2.7 showing the bigger picture also with the included jet launching region, which is not existent in the present simulations. Here the jet is just pushed into the grid from the beginning.

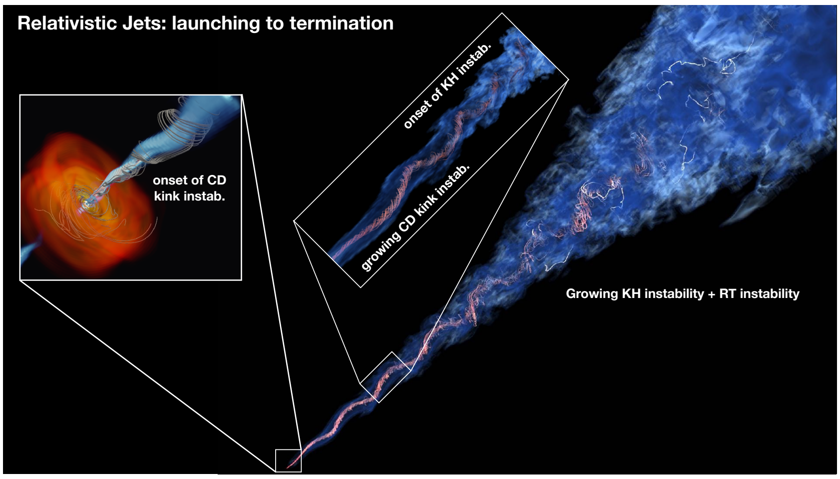

Figure 2.7: RMHD 3D simulation rendering with corresponding instabilities.

3 Raytracing

3.1 Numerical setup and emission parameters

As was already pointed out in the Sec.1.3.2 the radiative transfer equation 1.3.14 is solved along each ray to extract physical quantities from the 3D simulation to be able to compare them to other images. For this, it is necessary to determine the emission and absorption, which is done according to Fromm et al. (2018). A power law distribution of emitting particles is assumed

$$N(\gamma) = k_e \gamma^{-p} \text{ for } \gamma_{min} < \gamma < \gamma_{max} \tag{3.1.1}$$

where k_e is the normalization factor similar to the one shown in Eq.1.3.29. The lower and upper Lorentz electron factors are given by:

$$\gamma_{min} = \frac{P}{\rho} \frac{m_p}{m_e c^2} \frac{(s-2)}{(s-1)(\gamma_{adi}-1)} \frac{\epsilon_e}{\zeta_e} \tag{3.1.2}$$

since the spectral slope is always set $s > 2$ and

$$\gamma_{max} = \sqrt{\frac{3 m_e^2 c^4}{4\pi \cdot acc_e \cdot q^3 B_{cgs}}} \tag{3.1.3}$$

where ζ_e is the fraction of thermal particles in the distribution of non-thermal ones

$$\int_{\gamma_{min}}^{\gamma_{max}} N(\gamma) d\gamma = \zeta \frac{\rho}{m_p} \tag{3.1.4}$$

where m_p is the proton mass. The other parameter is ϵ_e, which relates the energy in the relativistic particles to the energy in the thermal particles

$$\int_{\gamma_{min}}^{\gamma_{max}} N(\gamma) \gamma m_e c^2 d\gamma = \epsilon_e \frac{p}{\gamma_{adi}-1} \tag{3.1.5}$$

where m_e is the electron mass. The parameter acc$_e$ sets γ_{max}, thus it determines the number of gyrations until γ_{max} is reached.
First, the numerical code units were provided with physical values. The jet density ρ_j was set to $8.3 \times 10^{-21}\,\mathrm{g/cm^3}$, and the jet radius R_j was chosen to be 50 gravitational

radii r_g. The gravitational radius was defined as

$$r_g = \frac{GM}{c^2}, \tag{3.1.6}$$

where G is the gravitational constant, M is the black hole mass, and c is the speed of light. Here, the black hole mass was set to $5 \times 10^5\, M_\odot$. The viewing angle was chosen to be $\theta = 9°$.
In addition to these scaling parameters, the emission parameters had to be set. To determine suitable values, a small parameter study was performed (see Fig. 3.1) to analyze the effects of the emission parameters on the SED of the source. It was found that the acceleration parameter acc_e has only a minor effect on the SED. In contrast, increasing the density and the energy fraction ϵ_e leads to an increase in flux, which is expected: a higher density provides more radiating particles, while a higher energy fraction means more available energy. The turnover frequency also shifts toward higher frequencies with increasing density or ϵ_e. The other big effect on the SED originates in the spectral slope s. Here, with a higher slope there is also more emission and the turnover shifts towards higher frequencies. Regarding the number density fraction ζ, increasing ζ leads to a reduced flux. While one might expect a higher ζ to increase the overall flux due to the larger number of available particles, the increased number density results in individual particles having lower γ factors, reducing the overall flux.

3.2 Results and discussion

For the final ray-tracing calculations, the emission parameters were set to $\epsilon_e = 0.4$, $\zeta_e = 0.7$, and $acc_e = 1 \times 10^7$, with a spectral slope of $s = 2.1$ representing dimensions of a 'realistic' source. The resulting SED is shown in Fig. 3.1f) - displaying a typical synchrotron hump, see Ch.1.3.2. The model was ray-traced for 40 different frequencies; the most relevant for later reconstructions - 15 GHz, 43 GHz, and 94 GHz - are marked with vertical lines. At 15 GHz, the SED reaches the turnover from the optically thick to the optically thin regime, while at 43 GHz and 94 GHz it is fully in the optically thin regime. Additionally, the flux at 15 GHz is higher than at 43 GHz and 94 GHz. The final ray-traced image is shown in Fig. 3.2. It has been discussed for some time that the magnetic field responsible for launching the jet likely has a helical structure. This helical structure, along with the filaments, arises from a certain pitch angle and the development of several instabilities - already discussed in the simulation chapter Sec.2.2 - and represents a generic source motivated by the observed appearance of 3C 279 (Fuentes et al. 2023). Besides the bright core and its surrounding region (within about 0.05 mas), there is a second enhanced bright spot further out (around 0.6 mas). This secondary component corresponds to a helical perturbation mode. The properties of the flow — such as pressure, density, and velocity - are locally modified by the helical wave, with the magnitude of these changes depending on position and time as modu-

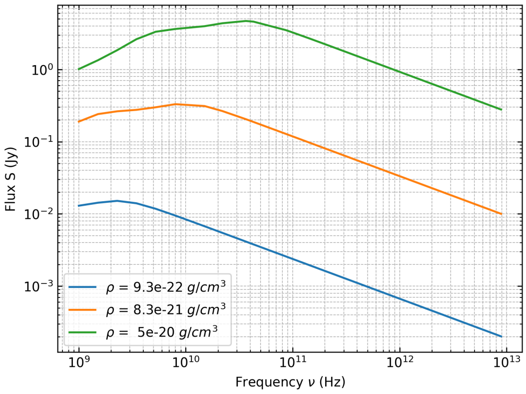

(a) ρ_e variation

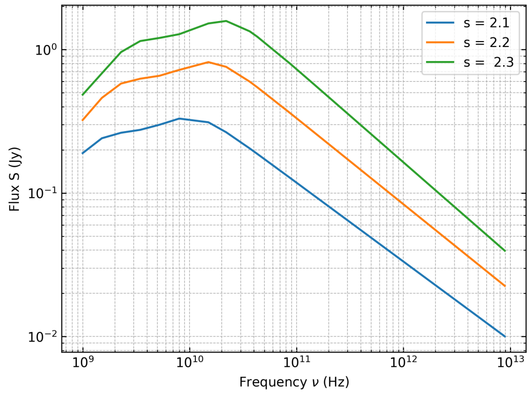

(b) slope s variation

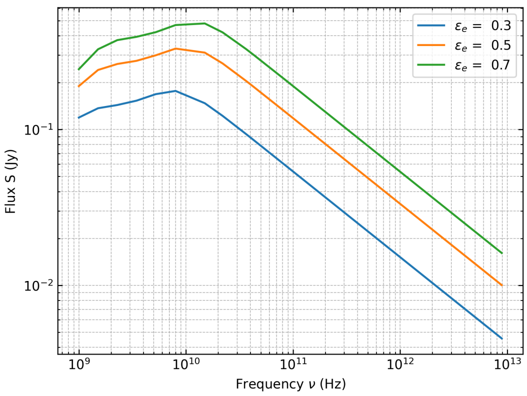

(c) ϵ_e variation

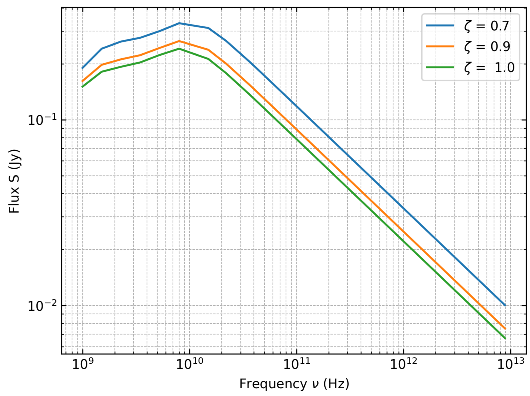

(d) ζ_e variation

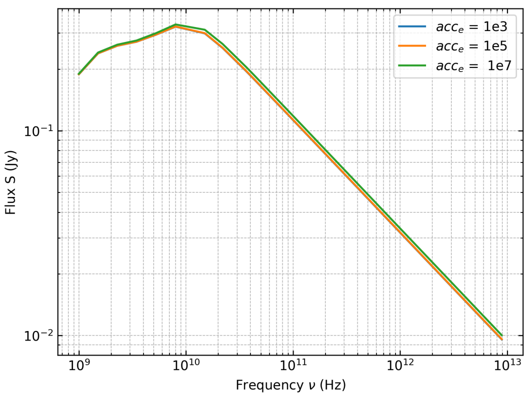

(e) acc$_e$ variation

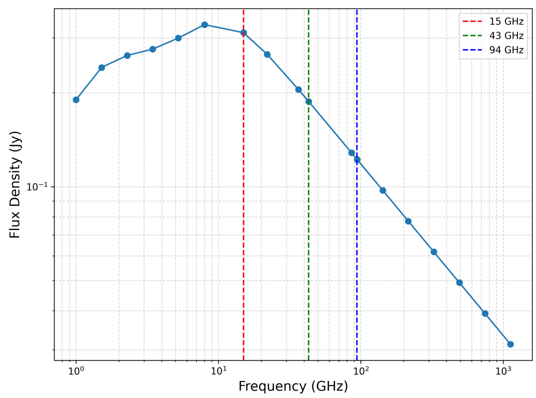

(f) SED of the final model

Figure 3.1: Overview of the effect of different parameters on the spectra and the final SED.

lated by the wave phase. These small variations in the flow properties could explain the observed differences in brightness between regions inside the jet and, in particular, along the filaments. Here, the perturbation of the three-velocity vector and the resulting changes in local Doppler boosting play a major role (Fuentes et al. 2023). This underlying structure is also supported by observations of 3C 279 with RadioAstron, a space VLBI array (Fuentes et al. 2023), as shown in Fig. 3.3. These observations were conducted at 22.2 GHz on March 10–11, 2014, achieving a resolution of roughly 27 μas - comparable to the Event Horizon Telescope (EHT) resolution of approximately 20 μas (Collaboration et al. 2019) - within 11.44 hours of observation time. RadioAstron was complemented by 23 ground-based antennas: ATCA (AT), Ceduna (CD), Hobart (HO), Korean VLBI Network (KVN) antennas Tanman (KT), Ulsan (KU), and Yonsei (KY), Mopra (MP), Parkes (PA), Sheshan (SH), Badary (BD), Urumqi (UR), Hartebeesthoek (HH), Kalyazin (KL), Metsähovi (MH), Noto (NT), Torun (TR), Medicina (MC), Onsala (ON), Yebes (YS), Jodrell Bank (JB), Effelsberg (EF), Svetloe (SV), and Zelenchukskaya (ZC). The sources have comparable sizes (about 1 mas). One can see that in the raytraced image, the pitch angle is higher, resulting in more frequent windings compared to the stretched-out windings seen in the observations. This suggests that the simulation is dominated by a helical perturbation mode, while the observations are better explained by elliptical perturbation modes. Another difference is that the simulated jet appears to contain only one filament with one additional component besides the core, whereas the observations reveal up to three filaments and two additional components besides the core. It should be noted, however, that the ray tracing shown in Fig. 3.2 represents only a snapshot of a dynamic simulation and serves primarily as a test model, without claiming to fully represent the real source. For the observations, a proposed source structure is schematically shown in Fig. 3.4. Here, as already mentioned, an elliptical perturbation mode - rather than a helical or standard shock-in-jet model according to Marscher & Gear (1985) - is proposed to explain the appearance of the two components in the jet along the filaments.

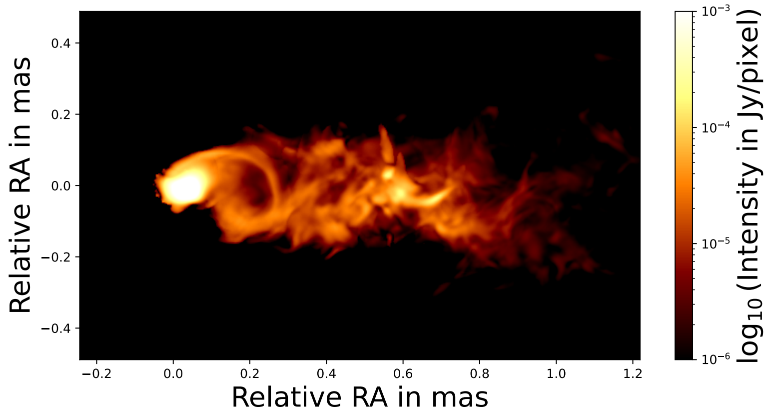

Figure 3.2: Raytraced model of a generic source.

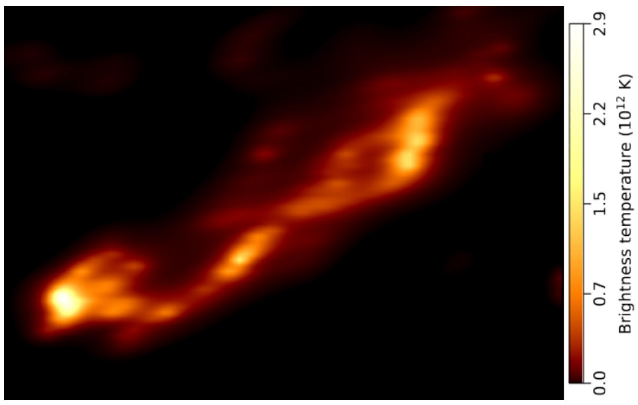

Figure 3.3: Actual observation of 3C 279 by RadioAstron.

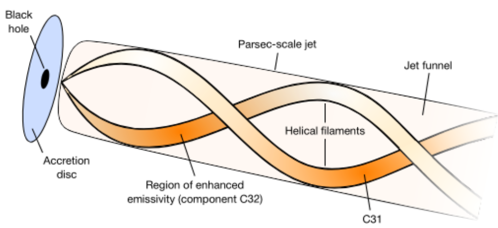

Figure 3.4: Proposed internal structure of the observed source by Fuentes et al. (2023).

4 Reconstructions

4.1 Numerical and observational setup

The final model presented in the previous chapter (Ch. 3) will now be reconstructed with different arrays. For this, synthetic observations have to be created. The observation date was set by default to 04.07.2017, representing the EHT observation of M87. The observation lasted for 24 hours with a 10-minute off-source time. The integration time was 12 seconds. The elevation limits were set with a 5-degree lower cutoff and a 90-degree upper cutoff. Due to computational constraints, all reconstructions were performed with 256 pixels. A systematic noise level of 2% was added in addition to the baseline-dependent thermal noise. The bandwidth was adjusted according to the specific array: 46 GHz for the ngVLA at 94 GHz, 20 GHz for lower frequencies, 512 MHz for GMVA, and 128 MHz for VLBA. The reconstructions were performed using the MEM algorithm, which was explained in Sec. 1.6. To ensure comparability, the same regularization functions were used for every reconstruction. Similar to Chael et al. (2016), four of them were employed. As the first step, a simple entropy regularizer, which rewards pixel-to-pixel similarity to a prior image, was applied on closure phases and amplitudes to obtain an initial reconstructed image:

$$S_{entropy} = -\sum_i I_i \log\left(\frac{I_i}{P_i}\right) \tag{4.1.1}$$

where I_i is the pixel intensity and P_i is the prior intensity. Then, to refine the output, additional regularization functions were applied on amplitude, closure phases, and logarithmic closure amplitudes. One of them is the smoothness constraint, which favors piecewise-smooth images with flat regions separated by sharp edges, in the form of a total variation (TV):

$$S_{TV} = -\sum_l \sum_m \sqrt{(I_{l+1,m} - I_{l,m})^2 + (I_{l,m+1} - I_{l,m})^2} \tag{4.1.2}$$

where the two sums are taken over the two image dimensions, and the image pixels $I_{l,m}$ are now indexed by their position (l, m) in the 2D $m \times m$ grid. In addition, there is also a l_1 sparsity prior:

$$S_{l_1} = -\sum I_i \tag{4.1.3}$$

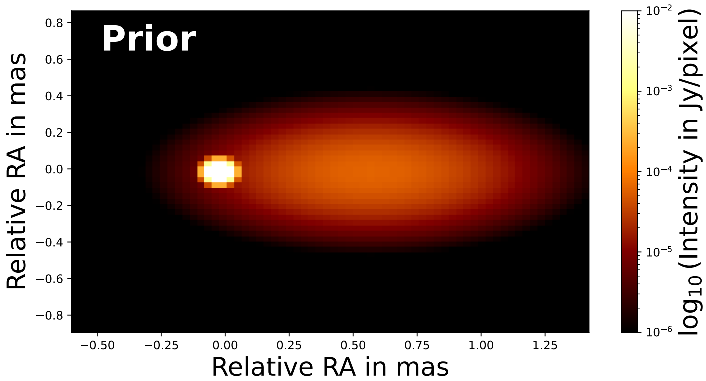

Figure 4.1: Initial prior for the reconstructed images consisting of one tiny Gaussian to prevent singularities, a small Gaussian prior to model the core region, and a large Gaussian prior to capture the extended emission.

and a total image flux density constraint:

$$S_{flux} = -\left(\sum I_i - F\right)^2 \tag{4.1.4}$$

where the sum is over the M pixels in the image and F is the total source flux density. The priors were set as shown in Fig. 4.1. A tiny Gaussian prior was placed in the center of the image to avoid singularities that can cause numerical problems. Besides that, a small Gaussian prior was placed in the center with 80% flux, and a large Gaussian was used to capture the extended emission regions of the jet. The form and number of priors remained the same for all reconstructions, except for the scaling of their size and intensity. As observational arrays, the ngVLA and the LEVERAGE program (Sec. 1.5.3) - namely ngVLA plus German stations (LEVERAGE), LEVERAGE plus Hungarian station (LEVERAGE+), and LEVERAGE+ plus Scandinavian stations (LEVERAGE+ SCD) - were primarily investigated. In addition, observations and corresponding reconstructions were also made with GMVA and VLBA arrays to demonstrate their limitations in this specific setting. The main component of these arrays is the ngVLA. For this array, a subset was selected - shown in Tab.4.2 - to properly represent the capabilities while keeping computational costs down. To increase the resolution, the outermost station of each arm (mid and spiral, see Sec.1.5.2, denoted as `mda-e` and `spa-e`) was selected, as well as the station in the middle of each arm (typically the 4th or 5th station). The core, consisting of 114 antennas, was phased (by means of Eq.1.4.19) into a single dish with a very high SEFD (denoted as `cor001`, see Tab.4.2). The stations denoted as `br1-3, hi1-3, hn1-3, ku1-3, gb1-3, nl1-3, ov1-3, pn1-3, pr1-3, sc1-3` belong to the VLA, which also participates in the observations. The German stations are arranged such that there is one station in the west (`EF1-3`), one in the north (`NS1-3`), one in the south (`UW1-3`), and one in the east (`DZA1-3`) of Germany with 3 telescopes each. Multiple co-located antennas enable the use of a powerful technique known as paired antenna calibration. In this method, one antenna continuously observes a calibrator source, while the others observe a nearby science target or additional calibrators. The phase fluctuations measured on the calibrator can then be used to correct the phase errors on the science antennas. This approach is conceptually similar to conventional phase referencing but offers a crucial benefit: the switching times are significantly shorter, being determined by atmospheric fluctuation scales and wind speed rather than by antenna slewing and settling delays. For the highest astrometric accuracy, it is also essential to correct for atmospheric and geometric model gradients across the array, which typically requires observing at least three calibrators. This can be most effectively achieved when multiple antennas are available at a station (see ngVLA Memo 105 by R. Craig Walker, NRAO[1]). It should be noted that such intra-station calibration effects were not included in the synthetic data generation for this study. There is also one station in Hungary (denoted as `best`) and two stations in Scandinavia (denoted as `ON` and `MET`). In general, the SEFDs change for each frequency, so they were adapted accordingly (see Tab. 4.1). All used antennas are summarized in Tab.4.2. The beamparameters of all used arays at different frequencies are shown in Tab.4.3.

Station	**SEFD each antenna [Jy]**	**SEFD core [Jy]**
ngVLA 15 GHz	292.2	2.47
ngVLA 43 GHz	602.8	5.09
ngVLA 94 GHz	1136	9.60
best[a]	1000	-
ON[b]	5102	-
MET[b]	17647	-

Table 4.1: SEFD values for various stations. All stations of ngVLA and German dishes have the same SEFD which differ with frequency. [a] Hungarian single station, [b] Scandinavian single stations.

Name	**X (m)**	**Y (m)**	**Z (m)**
EF01[1]	4033903.99400	486927.36780	4900346.03000
EF02[1]	4033940.47100	486870.82080	4900319.15200
EF03[1]	4033964.27900	486920.31540	4900369.20600
NS01[1]	3727172.81900	655159.29130	5116980.34800
NS02[1]	3727209.29600	655102.74430	5116953.47000
NS03[1]	3727233.10400	655152.23890	5117003.52300
UW01[1]	4152505.10300	828825.19330	4754338.16800
UW02[1]	4152541.57900	828768.64620	4754311.29000
UW03[1]	4152565.38700	828818.14080	4754361.34400
DZA01[1]	3872563.93800	1036724.79200	4944379.77700

[1]https://ngvla.nrao.edu/page/memos

Name	X (m)	Y (m)	Z (m)
DZA02[1]	3872600.41400	1036668.24500	4944352.89900
DZA03[1]	3872624.22200	1036717.73900	4944402.95200
mda005	-1435040.5853	-5157096.27258	3460158.54777
mda010	-1449749.7626	-4975288.89248	3709116.57513
mdb005	-1544802.04741	-5174937.18957	3384483.77355
mdb009	-1183245.94741	-5351855.70072	3252293.08822
mdc004	-1708943.10466	-5081198.78493	3446649.68063
mdc009	-1571335.35071	-5340497.63453	3105756.63202
mdd004	-1761150.2711	-5025408.76284	3502795.73904
mdd009	-1768820.86871	-5329702.15118	3017941.29798
mde005	-1816834.40983	-4964790.04294	3559295.36137
mde009	-2061927.09577	-5087265.39302	3237621.99350
spa005	-1604874.55956	-5037177.24048	3560025.89388
spa010	-1617585.04445	-5034601.85646	3558125.95440
spb005	-1598437.03805	-5039902.06318	3559064.83463
spb010	-1602269.94689	-5031462.40865	3569215.71055
spc005	-1598473.70556	-5044261.81000	3552942.01399
spc010	-1587887.47524	-5041744.36901	3561391.13906
spd005	-1605025.07746	-5044299.11423	3549975.84880
spd010	-1595054.94734	-5050882.77730	3545322.08062
spe005	-1608847.25751	-5039922.58158	3554375.42406
spe010	-1613219.18362	-5046938.98403	3542508.79528
cor001	-1603219.74529	-5041112.28265	3555223.45148
br01	-2112119.18282	-3705319.91352	4726826.39806
br02	-2112082.70620	-3705376.46053	4726799.52013
br03	-2112058.89810	-3705326.96595	4726849.57371
hi01	-5469327.86714	-2494930.43893	2130520.58917
hi02	-5469287.72828	-2495002.73687	2130527.75728
hi03	-5469293.38374	-2494947.18312	2130577.68245
hn01	1446345.58057	-4447968.09007	4322309.08306
hn02	1446381.12043	-4447940.98815	4322324.97218
hn03	1446346.62992	-4447939.82122	4322336.61122
ku01	-5544010.48303	-2054622.51133	2387335.91967
ku02	-5544005.58410	-2054533.41484	2387423.38309
ku03	-5544064.78593	-2054502.65100	2387313.12008
gb01	881972.74725	-4925212.32671	3943404.32772
gb02	881952.72371	-4925294.94253	3943306.29573
gb03	882064.62445	-4925253.83966	3943332.41272
nl01	-130910.88041	-4762328.22326	4226866.75948
nl02	-130858.19069	-4762325.27549	4226869.10598
nl03	-130874.81903	-4762357.52758	4226831.04230

Name	X (m)	Y (m)	Z (m)
ov01	-2409161.00327	-4478575.08100	3838627.78782
ov02	-2409273.65133	-4478510.65127	3838630.57060
ov03	-2409269.89917	-4478569.99815	3838563.42396
pn01	-2059737.49520	-3621582.62030	4813837.44062
pn02	-2059771.20994	-3621532.89741	4813860.26845
pn03	-2059784.21279	-3621572.32834	4813825.27582
pr01	2391064.77250	-5564466.47257	1994762.93309
pr02	2391002.48227	-5564445.71877	1994894.59934
pr03	2390914.00645	-5564502.65748	1994842.17124
sc01	2607855.00631	-5488082.76621	1932743.13985
sc02	2607823.76040	-5488064.45201	1932836.67078
sc03	2607792.64756	-5488111.99599	1932744.27296
best[2]	4037034.92566	1432206.32006	4710344.59570
ON[3]	3370947.11028	711462.43463	5349630.78049
MET[3]	2892550.44948	1311747.77059	5512673.55592

Table 4.2: All used antennas in the reconstructions. [1] German antennas for the LEVERAGE reconstructions, [2] Hungarian antenna, [2] Scandinavian antennas for LEVERAGE+ and LEVERAGE+ SCD reconstructions.

Source	Major axis (μas)	Minor axis (μas)	Position angle (rad)
ngVLA 15 GHz	712.82	687.70	0.986
ngVLA 43 GHz	248.66	239.89	0.986
ngVLA 94 GHz	123.19	118.86	0.971
GngVLA 94 GHz	71.37	67.37	0.168
GngVLA + HUN	70.16	66.13	0.160
GngVLA + HUN + SCD	68.87	64.84	0.151

Table 4.3: Beam parameters of different arrays for different frequencies respectively. P.A stands for positional angle.

4.2 VLBA and GMVA reconstructions

The reconstruction process is organized as follows: For each given frequency - 15 GHz, 43 GHz, and 94 GHz - the source is reconstructed while varying the parameters of length, declination, and intensity. First, the reconstructions are performed with the ngVLA array; then, this process is repeated for 94 GHz with the LEVERAGE array. One of the main advantages of the ngVLA is its sensitivity. To demonstrate this improvement and to explain why it was necessary, the initial jet model was reconstructed with a total flux of 20 mJy at 94 GHz, as shown in Fig.4.2. Although the GMVA and VLBA are among the most powerful VLBI arrays with their long baselines, the GMVA is unable to reconstruct the source at all in this low-flux scenario, and the VLBA only captures the priors - more an artifact of the algorithm than an actual reconstructed intensity signal. The compared quantities of visibility amplitudes and closure phases show a very noisy picture due to the low flux. This is because the GMVA array has a relatively small bandwidth (512 MHz), which results in a higher SEFD (Eq.1.4.19). The VLBA, on the other hand, also has a small bandwidth (128 MHz) and shorter baselines overall, with a more sparse uv coverage. In the following sections, all the reconstructed images for each frequency and for the different varied parameters are presented.

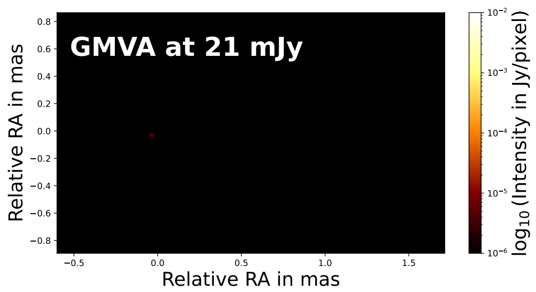

(a) Reconstruction with GMVA at 94 GHz at a declination of 70° with 21 mJy total flux and 1 mas source size.

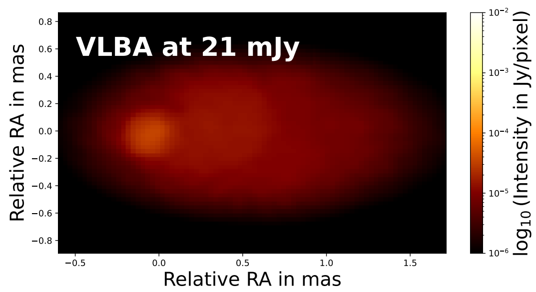

(b) Reconstruction with VLBA at 94 GHz at a declination of 70° with 21 mJy total flux and 1 mas source size.

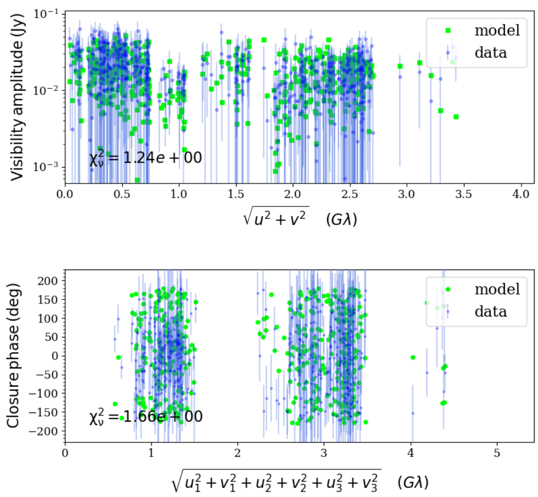

(c) Visibility amplitudes and closure phase plots of the GMVA reconstruction at 94 GHz.

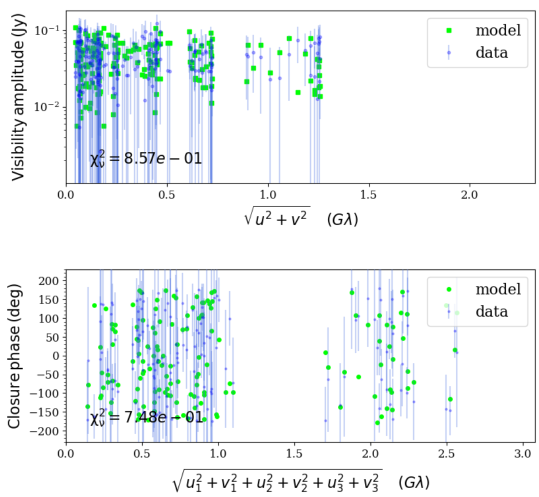

(d) Visibility amplitudes and closure phase plots of the VLBA reconstruction at 94 GHz.

Figure 4.2: Overview of reconstructed images, visibility amplitudes and closure phase plots at 94 GHz with GMVA and VLBA.

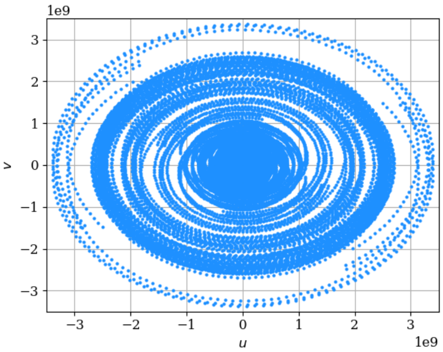

(a) Uv plot of the GMVA array at a declination of 70°.

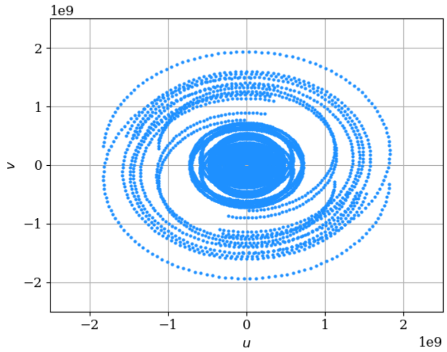

(b) Uv plot of the VLBA array at a declination of 70°.

Figure 4.3: Uv plots of the GMVA and VLBA at 94 GHz and a declination of 70°.

4.3 The variation in the declination of the source

4.3.1 Reconstructions at 15 GHz

The reconstructions were conducted at 15 GHz with fixed source size of 6 mas with 38.4 mJy total flux. Visual inspection alone (Fig.4.4) reveals only minor changes in the reconstructed image while varying the declination. The core region, as well as the second component, is well reconstructed across all declinations. The enhanced regions at the lower end of the images are also clearly visible as well as the inner filaments of the jet. The most noticeable optical difference appears when increasing the declination above 10°, since then the upper filamentary arc becomes more pronounced in comparison. However, this improvement is not substantial because the arc is already recognizable at 10°, although not so clearly. Also, the second component is resolved in more detail at 70° whereas it seems blurry at 10°. According to Fig.4.5a)-d), the biggest uv coverage is at 70°, changing mainly in the v axis. U axis stays the same at all four declinations. The visibility amplitude decreases across all baseline lengths, but the drop becomes especially pronounced beyond 0.3 $G\lambda$ where the coverage is not that dense, see Fig.4.5e)-f). The closure phases are spread evenly around ±50° until 0.5 $G\lambda$ when it starts to spread more, above 100° with strongly increased errorbars, see Fig.4.5g)-h).

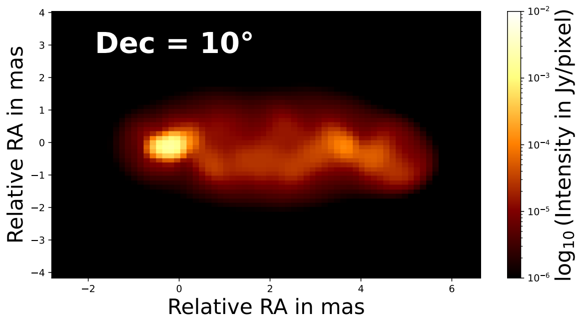

(a) Reconstruction at 15 GHz with a declination of 10° and 38 mJy total flux, in logarithmic scale.

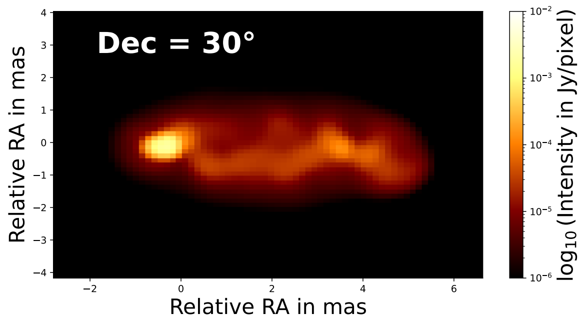

(b) Reconstruction at 15 GHz with a declination of 30° and 38 mJy total flux, in logarithmic scale.

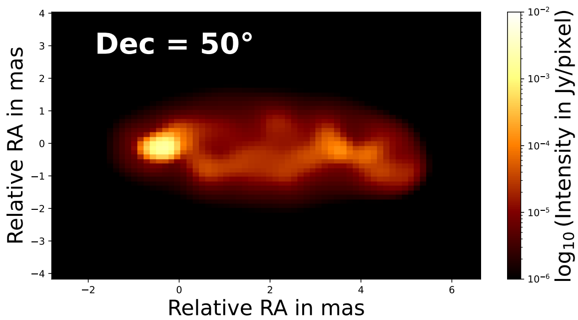

(c) Reconstruction at 15 GHz with a declination of 50° and 38 mJy total flux, in logarithmic scale.

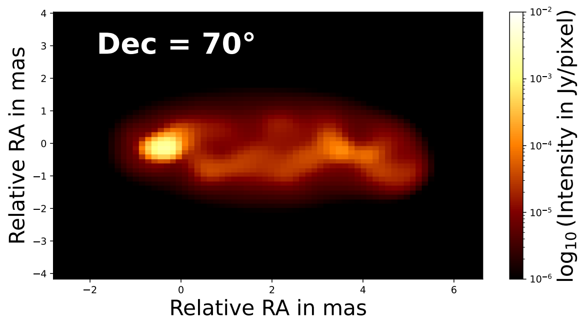

(d) Reconstruction at 15 GHz with a declination of 70° and 38 mJy total flux, in logarithmic scale.

Figure 4.4: Overview of reconstructed images at 15 GHz with 38 mJy total flux at different declinations.

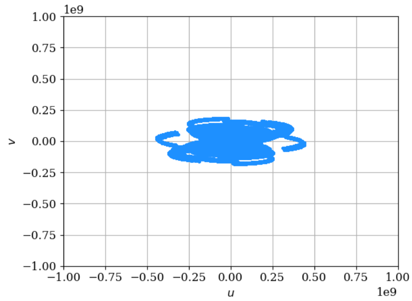

(a) Uv plot at a declination of 10° at 15 GHz.

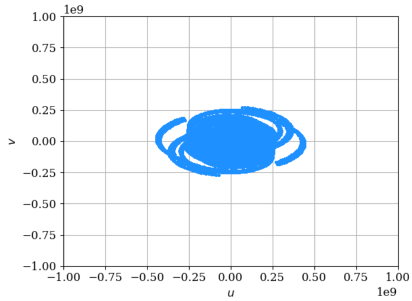

(b) Uv plot at a declination of 30° at 15 GHz.

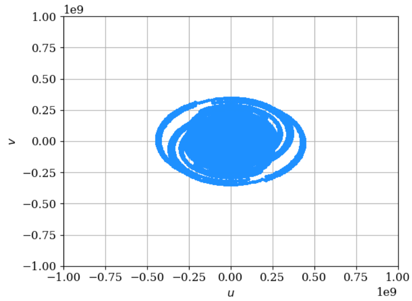

(c) Uv plot at a declination of 50° at 15 GHz.

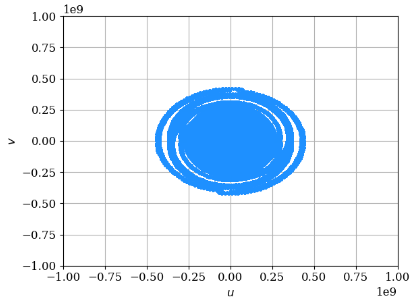

(d) Uv plot at a declination of 70° at 15 GHz.

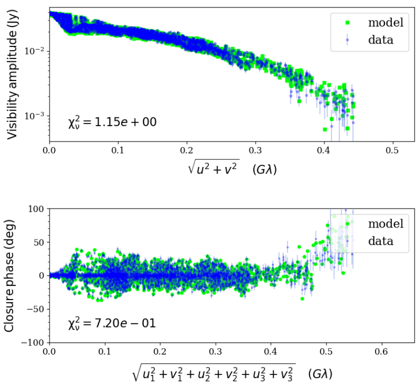

(e) Visibility amplitude and closure phase images at a declination of 10° at 15 GHz.

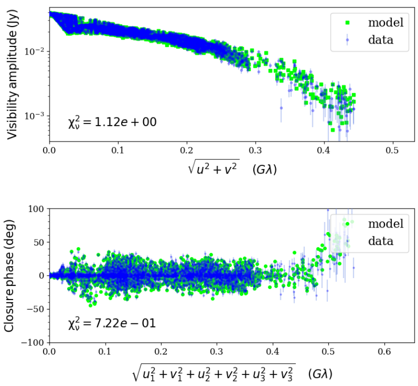

(f) Visibility amplitude and closure phase images at a declination of 30° at 15 GHz.

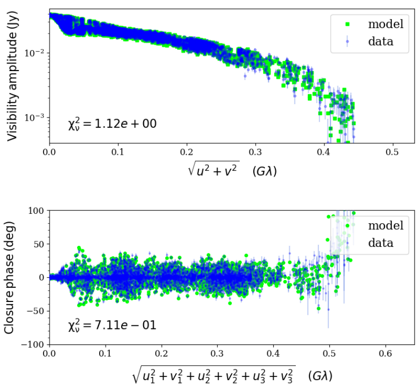

(g) Visibility amplitude and closure phase images at a declination of 50° at 15 GHz.

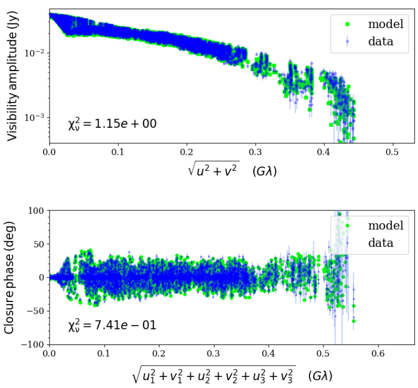

(h) Visibility amplitude and closure phase images at a declination of 70° at 15 GHz.

Figure 4.5: Overview of the uv coverages, visibility amplitudes and closure phase of the reconstructed images at 15 GHz with 38 mJy total flux at different declinations.

4.3.2 Reconstructions at 43 GHz

Here, the reconstructions were done with a source size of 3 mas and 32 mJy total flux. Most of the findings regarding the variation in declination at 15 GHz also applies at 43 GHz. Visually, there are only minor changes, especially since at 43 GHz the flux decreases, resulting in lower SNR, see Fig.4.6. The core structure and second component and the inner filaments are resolved. With increasing declination there is a higher uv coverage, see Fig.4.7a)-d) and more resolved structure especially the upper filamentary arc which appear more clearly at 70° and is blurry at 10° as well as the finer details regarding the second component. Generally, there is a bigger uv coverage at 43 GHz at all declinations. The enhanced drop in visibility amplitude appear now at roughly 0.9 $G\lambda$ and the closure amplitudes vary symmetrically around $\pm 20°$ up to 1.25 $G\lambda$ where it suddenly increase to higher degrees with increased errorbars.

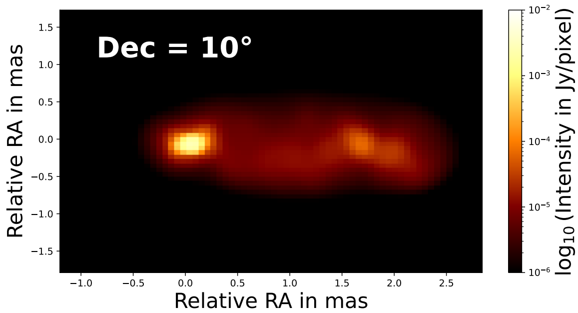

(a) Reconstruction at 43 GHz with a declination of 10° and 32 mJy total flux, in logarithmic scale.

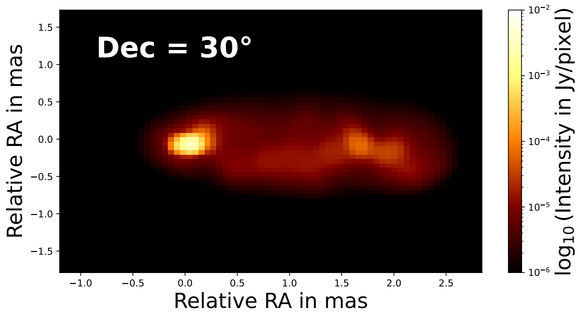

(b) Reconstruction at 43 GHz with a declination of 30° and 32 mJy total flux, in logarithmic scale.

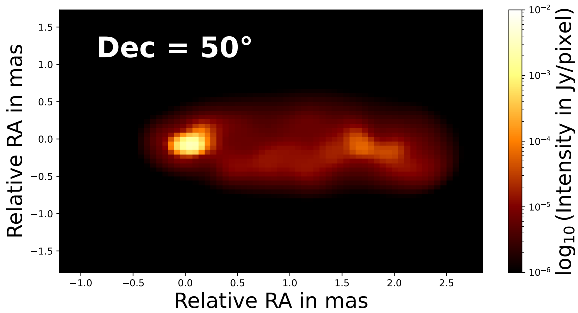

(c) Reconstruction at 43 GHz with a declination of 50° and 32 mJy total flux, in logarithmic scale.

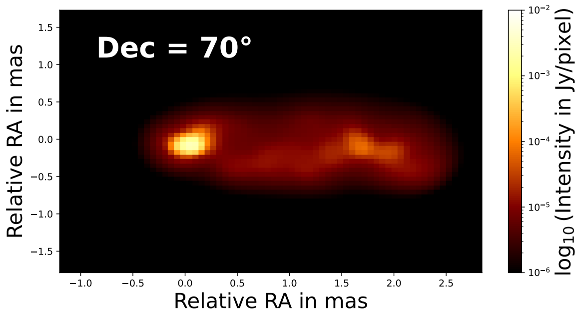

(d) Reconstruction at 43 GHz with a declination of 70° and 32 mJy total flux, in logarithmic scale.

Figure 4.6: Overview of reconstructed images at 43 GHz with 32 mJy at different declinations.

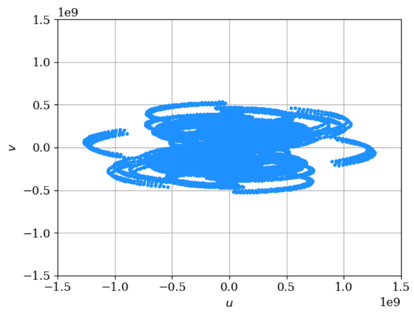

(a) Uv plot at a declination of 10° at 43 GHz.

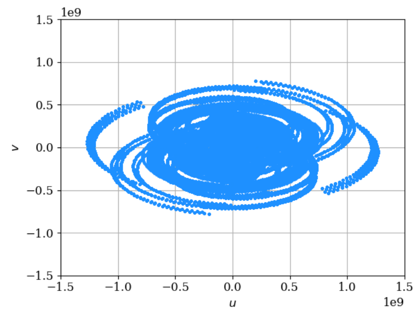

(b) Uv plot at a declination of 30° at 43 GHz.

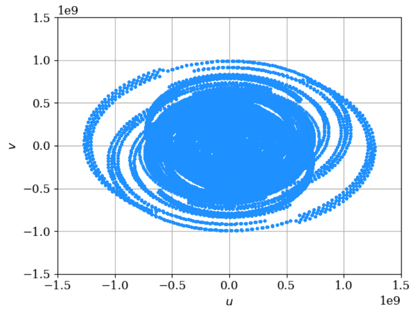

(c) Uv plot at a declination of 50° at 43 GHz.

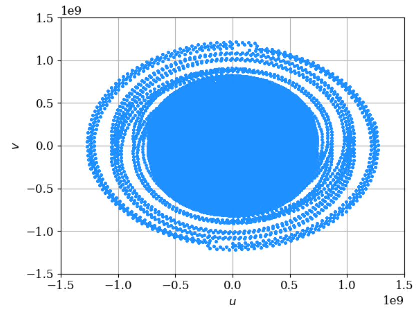

(d) Uv plot at a declination of 70° at 43 GHz.

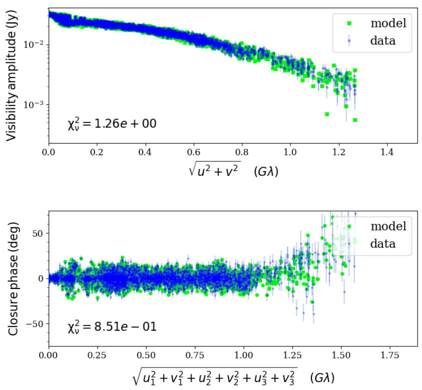

(e) Visibility amplitude and closure phase images at a declination of 10° at 43 GHz.

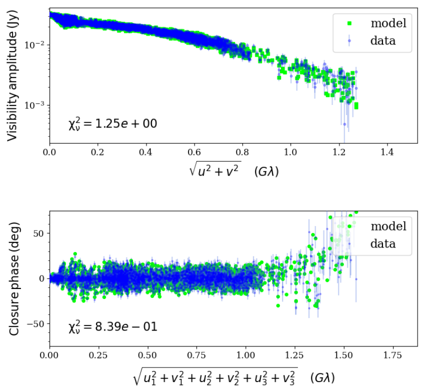

(f) Visibility amplitude and closure phase images at a declination of 30° at 43 GHz.

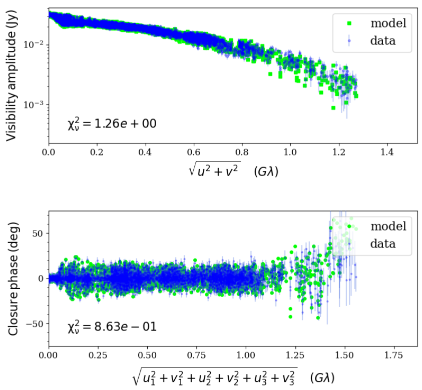

(g) Visibility amplitude and closure phase images at a declination of 50° at 43 GHz.

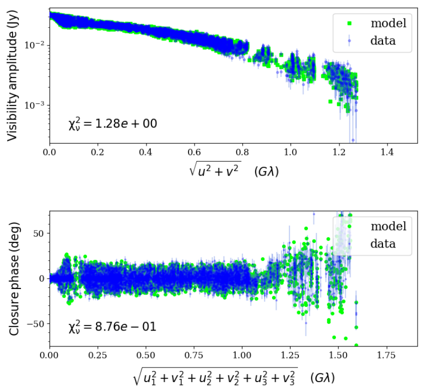

(h) Visibility amplitude and closure phase images at a declination of 70° at 43 GHz.

Figure 4.7: Overview of the uv coverages, visibility amplitudes and closure phase of the reconstructed images at 43 GHz with 32 mJy total flux at different declinations.

4.3.3 Reconstructions at 94 GHz

A similar picture emerges at 94 GHz with the ngVLA, where the reconstructions are done with 21.4 mJy total flux with a source size of 1.5 mas, see Fig.4.8. Here, the total flux is the lowest, which results in weaker SNR and thus larger scatter and mismatches, especially at longer baselines (around 2.0 $G\lambda$), see Fig.4.9e)-h), where the uv gaps become significant. There is also the largest uv coverage at 94 GHz since the baseline lengths scale with frequency. Visually, it can be seen that the source is much fainter than at 15 GHz and 43 GHz (Fig.4.4 and Fig.4.6). The core region and the second component are still recognizable, but it is challenging to discern the helical twisting arms. The closure phases are distributed equally around zero to roughly $\pm 25°$ but start to spread wider from about 2.5 $G\lambda$.

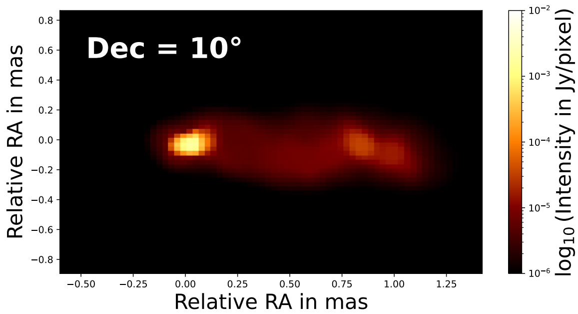

(a) Reconstruction at 94 GHz with a declination of 10° and 21 mJy total flux, in logarithmic scale.

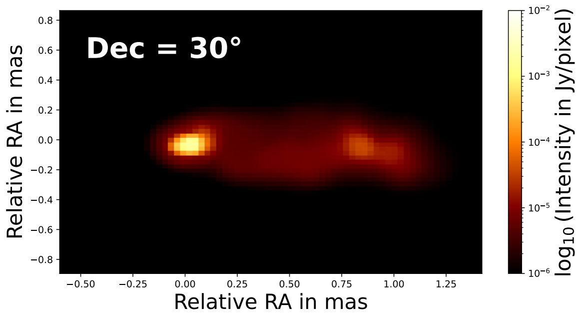

(b) Reconstruction at 94 GHz with a declination of 30° and 21 mJy total flux, in logarithmic scale.

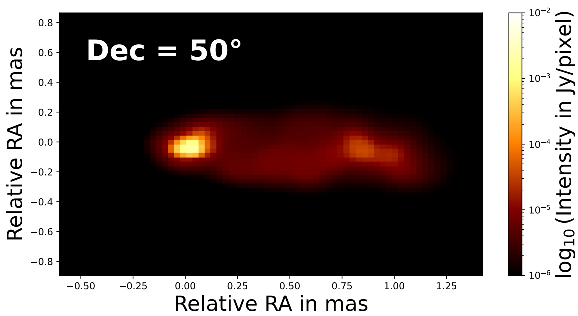

(c) Reconstruction at 94 GHz with a declination of 50° and 21 mJy total flux, in logarithmic scale.

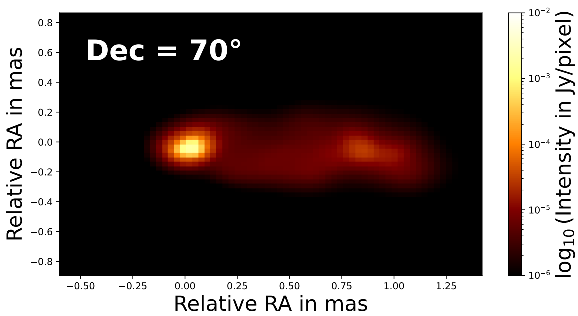

(d) Reconstruction at 94 GHz with a declination of 70° and 21 mJy total flux, in logarithmic scale.

Figure 4.8: Overview of the reconstructed images at 94 GHz with 21 mJy total flux at different declinations.

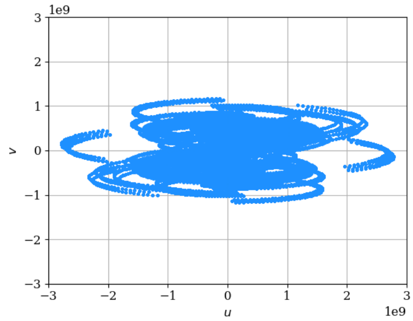

(a) Uv plot at a declination of 10° at 94 GHz.

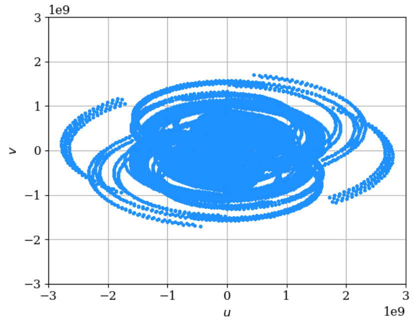

(b) Uv plot at a declination of 30° at 94 GHz.

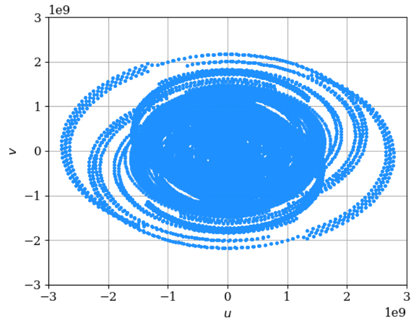

(c) Uv plot at a declination of 50° at 94 GHz.

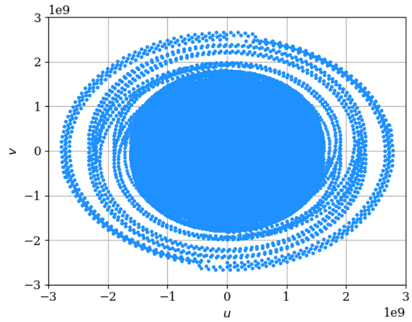

(d) Uv plot at a declination of 70° at 94 GHz.

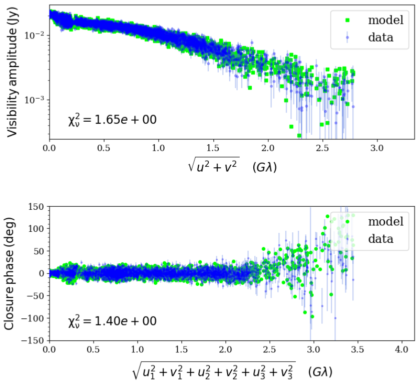

(e) Visibility amplitude and closure phase images at a declination of 10° at 94 GHz.

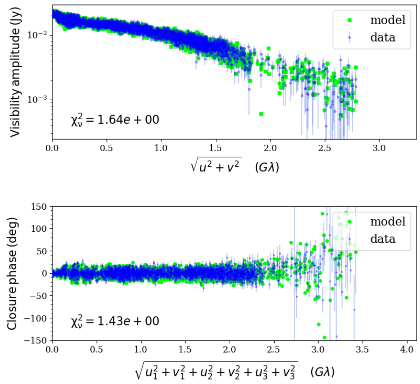

(f) Visibility amplitude and closure phase images at a declination of 30° at 94 GHz.

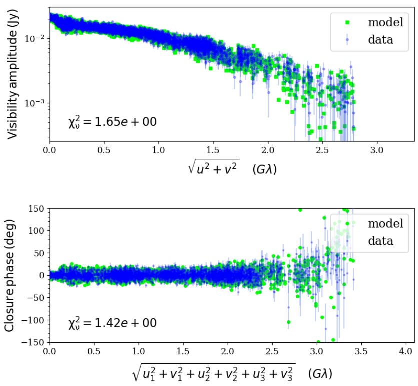

(g) Visibility amplitude and closure phase images at a declination of 50° at 94 GHz.

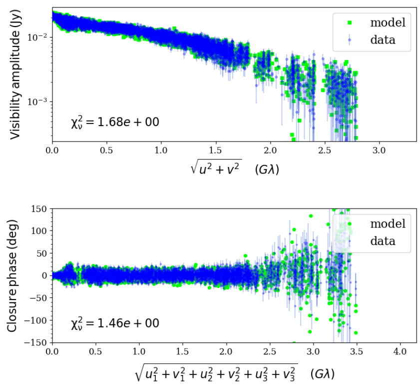

(h) Visibility amplitude and closure phase images at a declination of 70° at 94 GHz.

Figure 4.9: Overview of the uv coverages, visibility amplitudes and closure phase of the reconstructed images at 94 GHz with 21 mJy total flux at different declinations.

4.4 The variation in the length of the source

4.4.1 Reconstructions at 15 GHz

The next parameter to be varied is the source size at 15 GHz. For this, the declination was fixed at 70° and the total flux at 380 mJy. Changing this parameter significantly affects the visual appearance of the image compared to variations in declination (see Fig. 4.10). A source with an extent of 1 mas is barely resolved (see Fig. 4.10a), where only two large Gaussians are visible, representing the core region and a second component. Apart from these two potential emission regions, no finer structure is apparent. With a source size of 3 mas (see Fig. 4.10b), the reconstruction improves but still only shows two visible regions, which suggest the presence of filaments that are not yet resolved. Increasing the source size to 5 mas (Fig. 4.10c) reveals the filamentary arcs, and the core region becomes clearly separated from the second component. At 7 mas (Fig. 4.10d), the filaments and the second component are resolved in even more detail. This trend is also evident in the visibility amplitude and closure phase plots (see Fig.4.11). While there is little decrease in amplitude for a 1 mas source (Fig.4.11a), a 7 mas extended source shows a stronger amplitude cutoff, starting at roughly 0.3 $G\lambda$ similar to the behavior seen for declination variations (Fig. 4.4). The closure phases scatter around zero to ±50°.

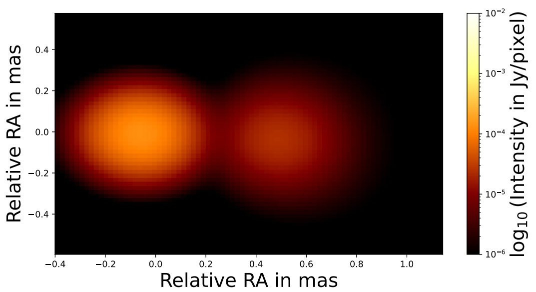

(a) Reconstructions at 15 GHz with a declination of 70°, 380 mJy total flux and 1 mas extend, in logarithmic scale.

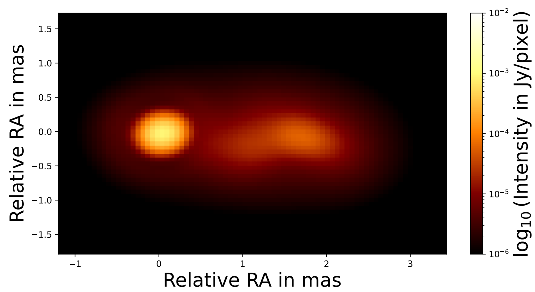

(b) Reconstructions at 15 GHz with a declination of 70°, 380 mJy total flux and 3 mas extend, in logarithmic scale.

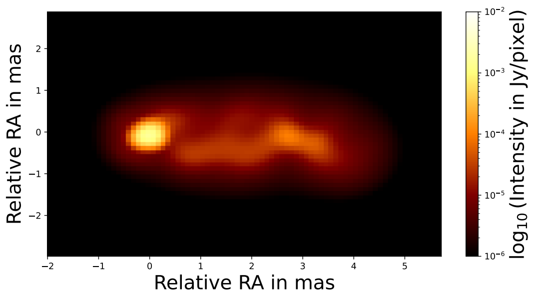

(c) Reconstructions at 15 GHz with a declination of 70°, 380 mJy total flux and 5 mas extend, in logarithmic scale.

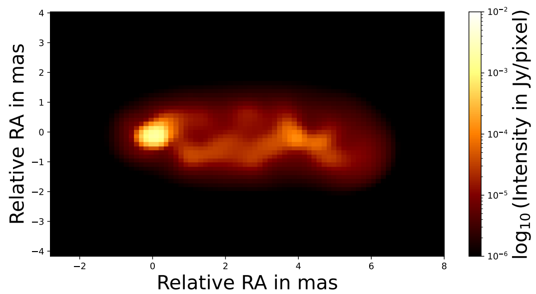

(d) Reconstructions at 15 GHz with a declination of 70°, 380 mJy total flux and 7 mas extend, in logarithmic scale.

Figure 4.10: Overview of the reconstructed images at 15 GHz, 380 mJy total flux and different sizes of the source.

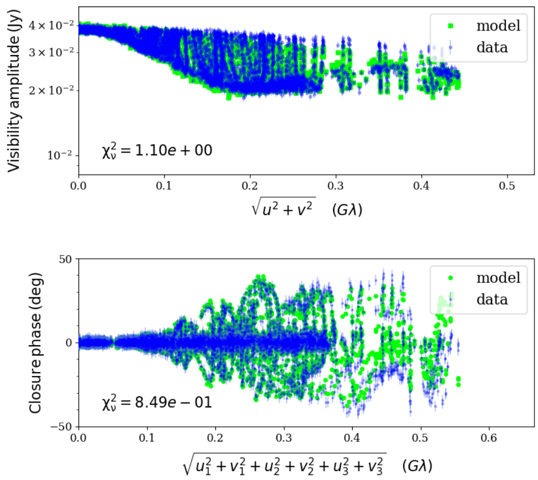

(a) Visibility amplitude and closure phase images at a length of 1 mas at 15 GHz.

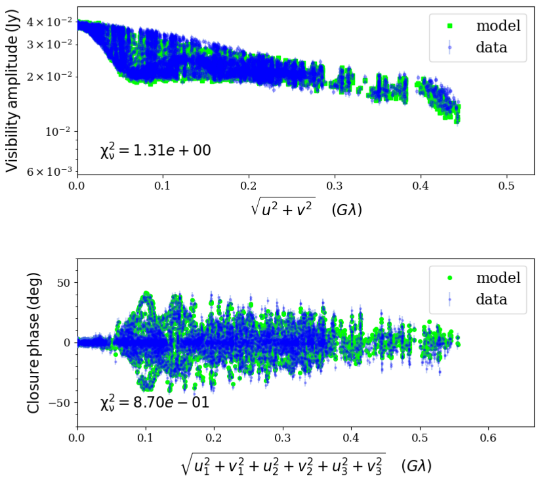

(b) Visibility amplitude and closure phase images at a length of 3 mas at 15 GHz.

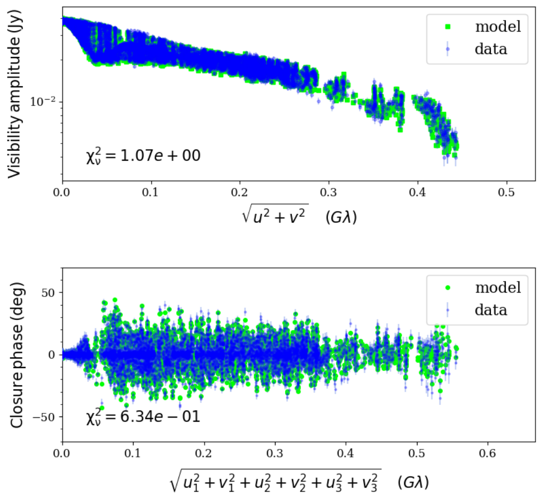

(c) Visibility amplitude and closure phase images at a length of 5 mas at 15 GHz.

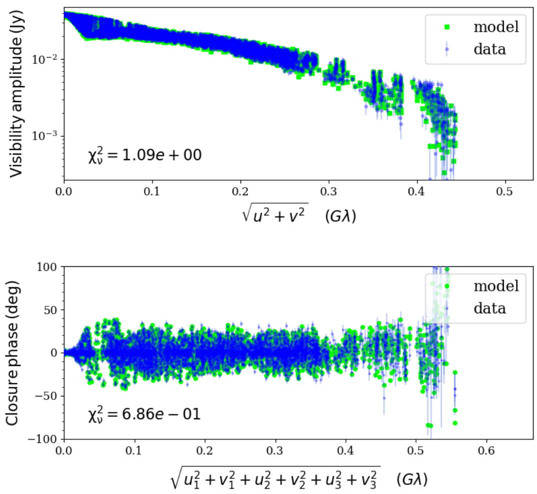

(d) Visibility amplitude and closure phase images at a length of 7 mas at 15 GHz.

Figure 4.11: Overview of the visibility amplitudes and closure phase of the reconstructed images at 15 GHz with 380 mJy total flux at different lengths of the source.

4.4.2 Reconstructions at 43 GHz

At 43 GHz, a similar picture emerges as at 15 GHz - there are significant visual differences between the reconstructed images at different source sizes, as shown in Fig.4.12. The reconstructions were conducted with a fixed declination of 70° and a total image flux of 320 mJy. The 1 mas source in Fig.4.12a) still consists mainly of two Gaussians representing the two components in the jet, but they are now more clearly defined and separated, comparable to the 2 mas image at 15 GHz (see Fig.4.10b). With larger source sizes, the visual appearance improves further, and finer details become visible. At 3 mas (Fig.4.12b), the filaments are already visible, although not very clearly, and the second component is reconstructed with more detail. Further increases in source size only enhance the quality of the reconstructed images, as shown in Fig.4.12c) and Fig.4.12d). Fig.4.12d) has a grainy appearance in comparison to the other images, which is due to the set regularizer in MEM. The visibility amplitude plots show similar behavior as at 15 GHz: for the unresolved 1 mas image there is no strong decrease in flux (Fig.4.13a), unlike the other sources (Fig.4.13b–d), where the amplitude starts to drop more enhanced around 0.8 $G\lambda$. The closure phases are evenly distributed around zero up to ±20° in the case of the unresolved source but begin to scatter strongly for larger sources beyond a baseline length of 1 $G\lambda$. While the scatter is moderate at 3 mas (Fig. 4.13b), it increases up to ±200° and becomes even larger at 7 mas, accompanied by enlarged errorbars.

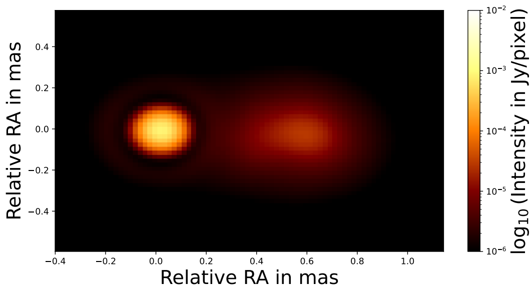

(a) Reconstructions at 43 GHz with a declination of 70°, 32 mJy total flux and 1 mas extend, in logarithmic scale.

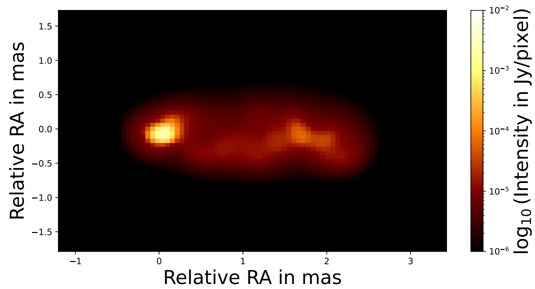

(b) Reconstructions at 43 GHz with a declination of 70°, 32 mJy total flux and 3 mas extend, in logarithmic scale.

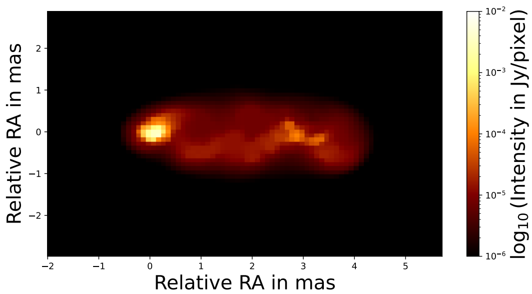

(c) Reconstructions at 43 GHz with a declination of 70°, 32 mJy total flux and 5 mas extend, in logarithmic scale.

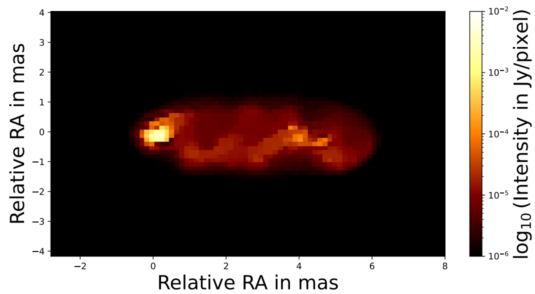

(d) Reconstructions at 43 GHz with a declination of 70°, 32 mJy total flux and 7 mas extend, in logarithmic scale.

Figure 4.12: Overview of reconstructed images at 43 GHz, 320 mJy total flux and different sizes of the source.

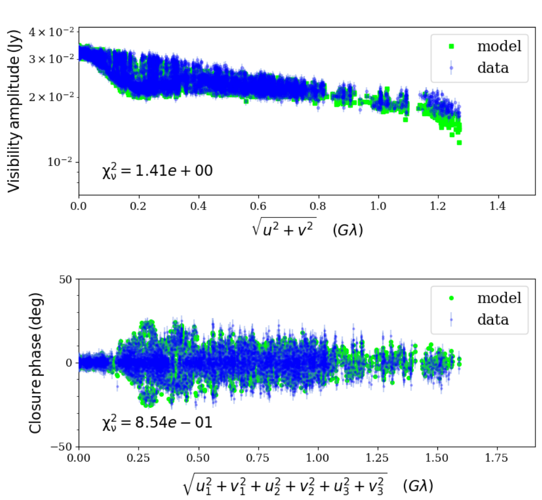

(a) Visibility amplitude and closure phase images at a length of 1 mas at 43 GHz.

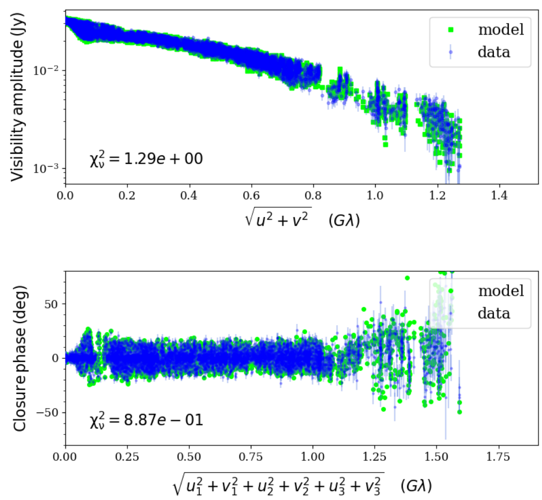

(b) Visibility amplitude and closure phase images at a length of 3 mas at 43 GHz.

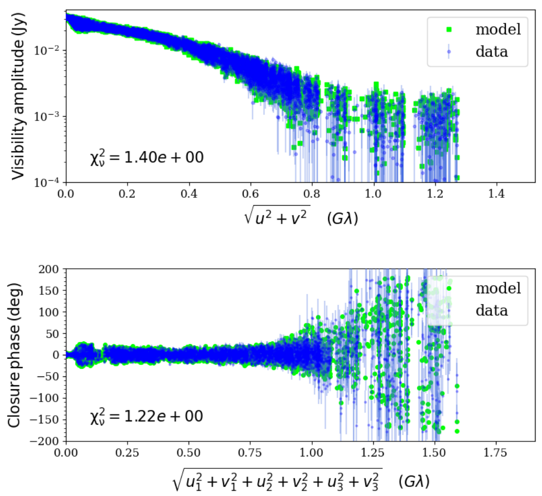

(c) Visibility amplitude and closure phase images at a length of 5 mas at 43 GHz.

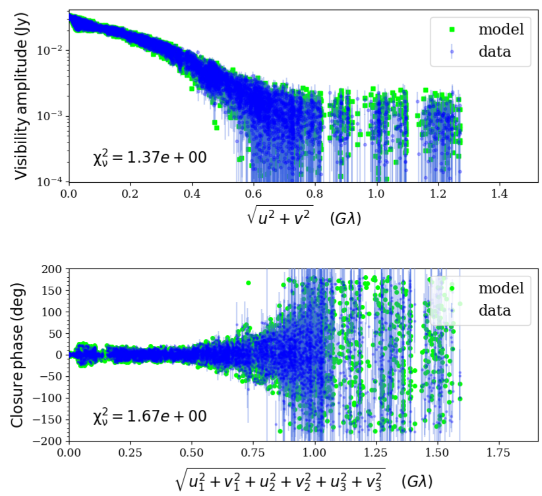

(d) Visibility amplitude and closure phase images at a length of 7 mas at 43 GHz.

Figure 4.13: Overview of the visibility amplitudes and closure phase of the reconstructed images at 15 GHz with 380 mJy total flux at different lengths of the source.

4.4.3 Reconstructions at 94 GHz

For the 94 GHz reconstructions, the source was set at a declination of 70° with a total flux of 21 mJy. At a source size of 0.2 mas, both jet components are indicated, although the second component is very faint and thus harder to recognize. The image with a 0.5 mas source size (Fig.4.14b)) closely resembles the 1 mas reconstruction at 43 GHz shown in Fig.4.12b). At 1 mas (Fig.4.14c)), the two jet components are resolved, but no filamentary structures are visible. This changes at 1.5 mas extent, where the full helical filaments are not visible, but enhanced regions at the lower end of the source become more distinct, and the second component is resolved in greater detail. Thus, the best visual reconstruction is achieved at a source size of approximately 1.5 mas (Fig.4.14d)). Because the total flux at 94 GHz is lower compared to other frequencies, the signal-to-noise ratio (SNR) is weaker. Nevertheless, it is remarkable that even at very low total flux, both components can still be properly recovered across all source sizes. When the source is resolved, a drop in visibility amplitude appears around 2 $G\lambda$, as shown in Fig.4.15c) and d). In contrast, the visibility amplitudes in Fig.4.15a) and b) remain roughly constant. The closure phases are spread evenly within ±20°, with no significant jumps except from about 2.5 $G\lambda$ onwards (Fig. 4.15), where the closure phases begin to scatter more strongly.

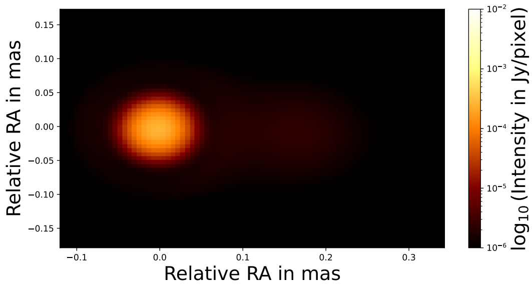

(a) Reconstructions at 94 GHz with a declination of 70°, 21 mJy total flux and 0.3 mas extend, in logarithmic scale.

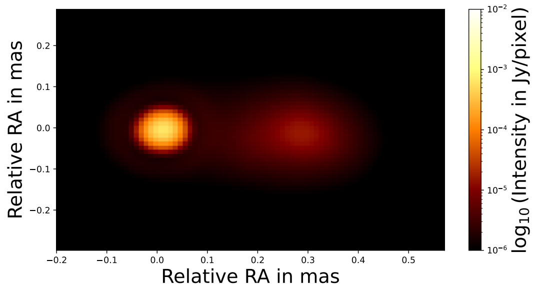

(b) Reconstructions at 94 GHz with a declination of 70°, 21 mJy total flux and 0.5 mas extend, in logarithmic scale.

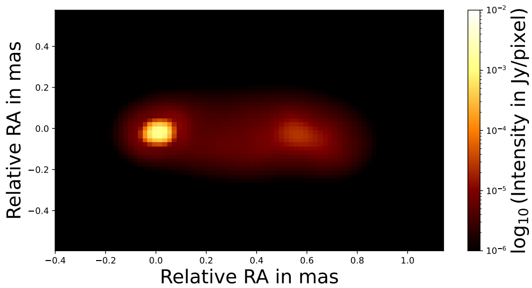

(c) Reconstructions at 94 GHz with a declination of 70°, 21 mJy total flux and 1 mas extend, in logarithmic scale.

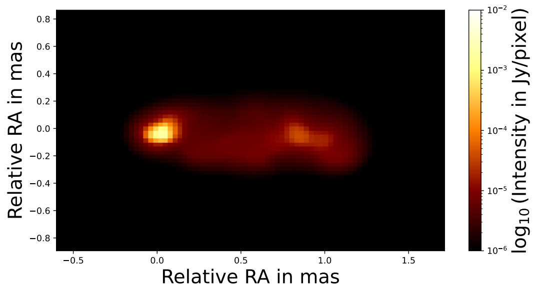

(d) Reconstructions at 94 GHz with a declination of 70°, 21 mJy total flux and 1.5 mas extend, in logarithmic scale.

Figure 4.14: Overview of the reconstructed images at 94 GHz, 21 mJy total flux and different sizes of the source.

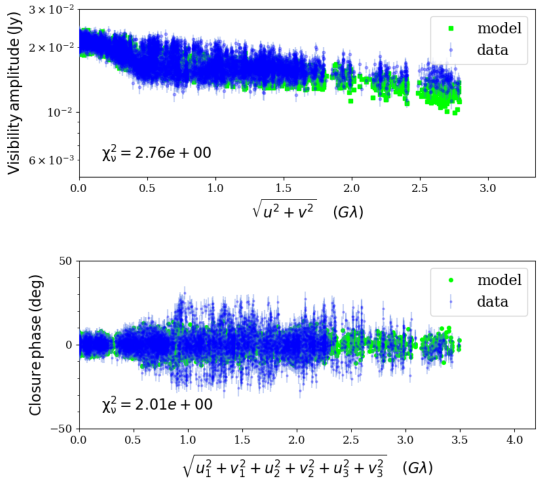

(a) Visibility amplitude and closure phase images at a length of 0.3 mas at 94 GHz.

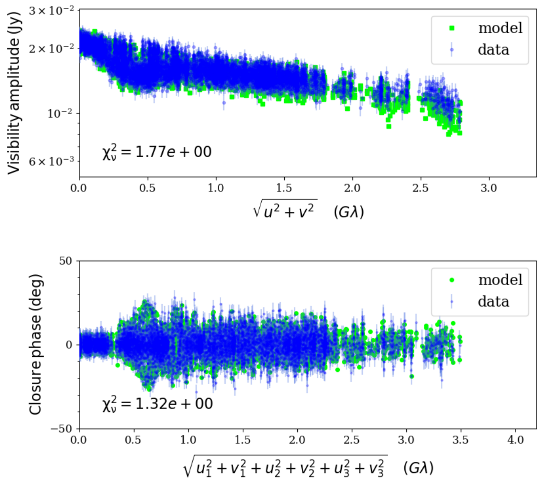

(b) Visibility amplitude and closure phase images at a length of 0.5 mas at 94 GHz.

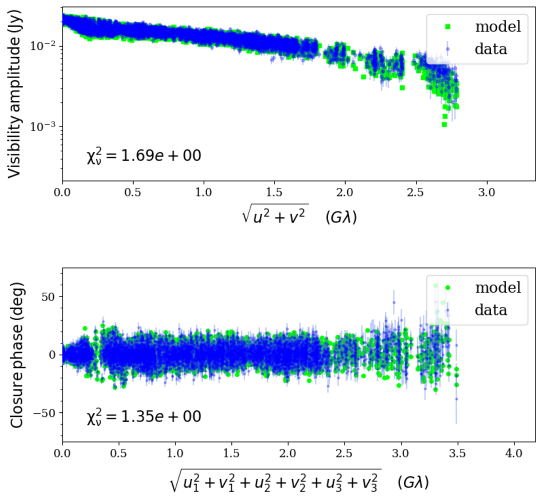

(c) Visibility amplitude and closure phase images at a length of 1 mas at 94 GHz.

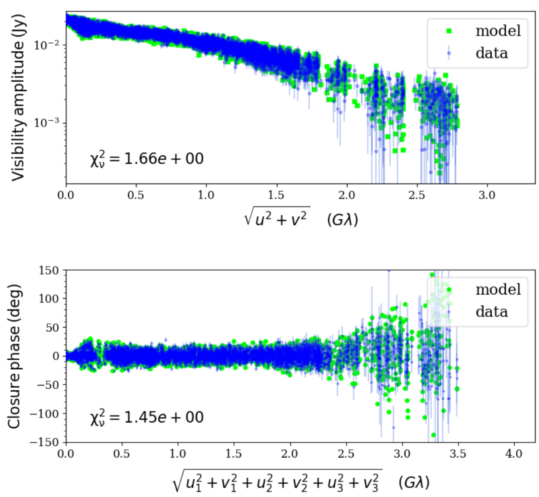

(d) Visibility amplitude and closure phase images at a length of 1.5 mas at 94 GHz.

Figure 4.15: Overview of the visibility amplitudes and closure phase of the reconstructed images at 94 GHz with 21 mJy total flux at different lengths of the source.

4.5 The variation in the intensity of the source

4.5.1 Reconstructions at 15 GHz

The last parameter varied is the intensity of the source to test the detectability limits of the ngVLA. For declination and source size, the best values were chosen: 70° and approximately 7 mas. For the source with 0.4 mJy flux (Fig.4.16a)), there is visually no essential detection in comparison to the other reconstructed images. This is mainly due to the set dynamical range, which was kept constant for compairability reasons. This will be discussed in further sections. At 3.8 mJy total flux (Fig.4.16b)), one can still reconstruct the core region and there are hints of the second component, but no filaments or inner structure at all are visible. For 38.4 mJy and 384 mJy (Fig.4.16a)-b)) the core region, the second component and the helical filaments are reconstructed very good. The visibility amplitudes and closure phases for 0.4 mJy are completely - and for 3.8 mJy nearly completely - dominated by noise, since the SNR is very weak, see Fig.4.17a)-b). The image at 38 mJy represent the same image as in Fig.4.5. For Fig.4.17d) there is a stronger cutoff in amplitude at roughly 0.3 $G\lambda$. The closure phases scatter around zero up to 50° for both 38 mJy and 380 mJy.

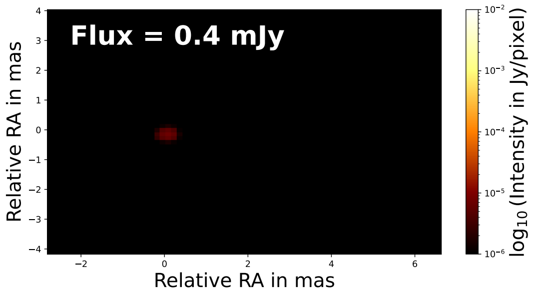

(a) Reconstructions at 15 GHz with a declination of 70°, 7 mas extend and 0.4 mJy total flux, in logarithmic scale.

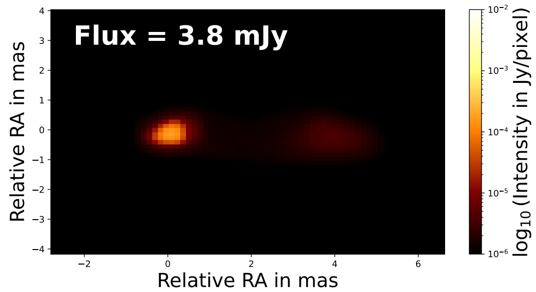

(b) Reconstructions at 15 GHz with a declination of 70°, 7 mas extend and 3.8 mJy total flux, in logarithmic scale.

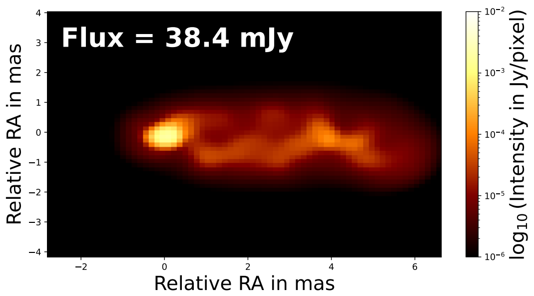

(c) Reconstructions at 15 GHz with a declination of 70°, 7 mas extend and 38 mJy total flux, in logarithmic scale.

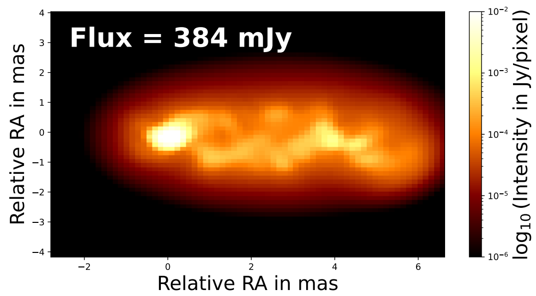

(d) Reconstructions at 15 GHz with a declination of 70°, 7 mas extend and 384 mJy total flux, in logarithmic scale.

Figure 4.16: Overview of the reconstructed images at 15 GHz with 7 mas extend and different intensities of the source.

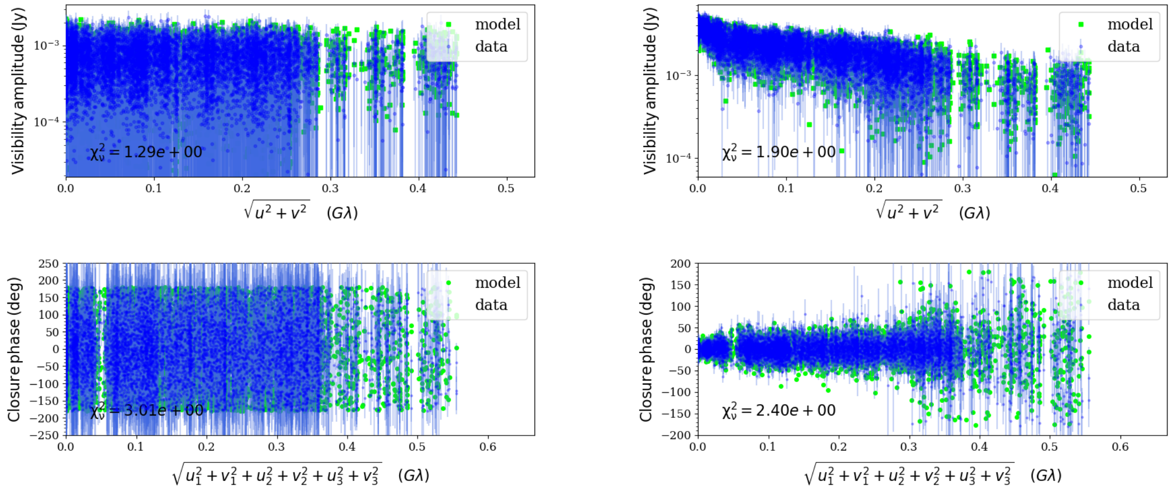

(a) Visibility amplitude and closure phase images at 0.4 mJy total flux and 15 GHz.

(b) Visibility amplitude and closure phase images at 3.8 mJy total flux and 15 GHz.

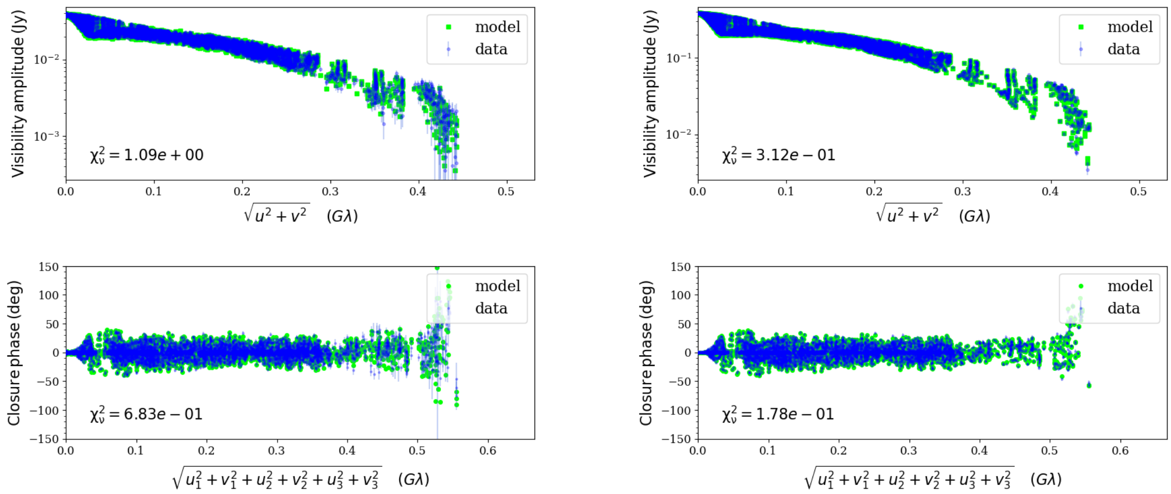

(c) Visibility amplitude and closure phase images at 38.4 mJy total flux and 15 GHz.

(d) Visibility amplitude and closure phase images at 384 mJy total flux and 15 GHz.

Figure 4.17: Overview of the visibility amplitudes and closure phase of the reconstructed images at 15 GHz with 7 mas extend and with different intensities of the source.

4.5.2 Reconstructions at 43 GHz

For the 43 GHz reconstructions, the declination was set to 70° and the source size to 3 mas. Very similar to the reconstruction at 15 GHz, there is little to no signal below 32 mJy - again considering the set dynamic range in logarithmic scale. At 3.2 mJy, only the core region is visible; the second component is no longer detectable compared to the 15 GHz case (see Fig.4.18b). At 32.1 mJy, both the core region and the second component become visible, along with filamentary structures within the jet (see Fig.4.18c). Fig.4.18d) shows the reconstruction with a total flux of 320 mJy, where the source structure is nearly perfectly recovered, including all major features.
The visibility amplitudes and closure phases for the 0.3 mJy and 3.2 mJy reconstructions are dominated by noise due to the low signal-to-noise ratio (see Fig. 4.19a–b). For the resolved images, a enhanced drop in visibility amplitude is observed around 1 $G\lambda$. The closure phases are scattered around zero up to ±25°, and begin to deviate significantly at baselines beyond approximately 1.2 $G\lambda$.

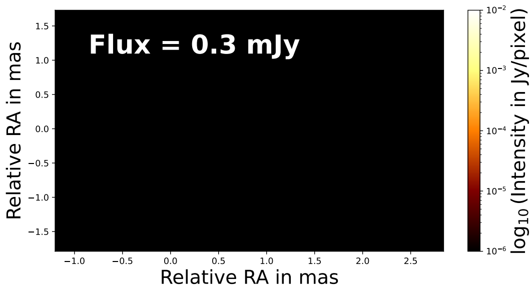

(a) Reconstructions at 43 GHz with a declination of 70°, 3 mas extend and 0.3 mJy total flux, in logarithmic scale.

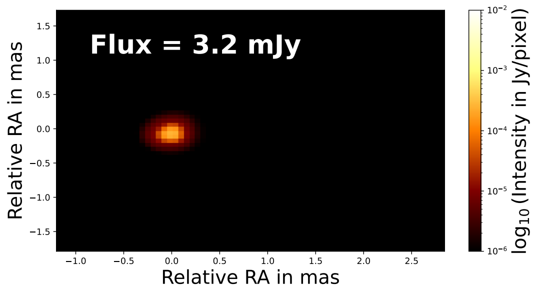

(b) Reconstructions at 43 GHz with a declination of 70°, 3 mas extend and 3.2 mJy total flux, in logarithmic scale.

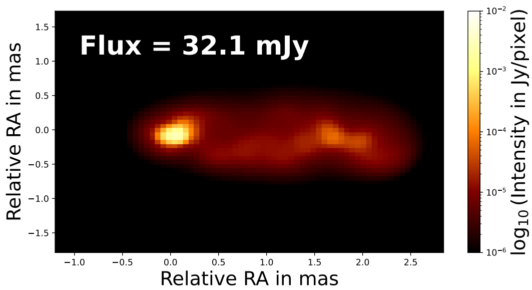

(c) Reconstructions at 43 GHz with a declination of 70°, 3 mas extend and 32 mJy total flux, in logarithmic scale.

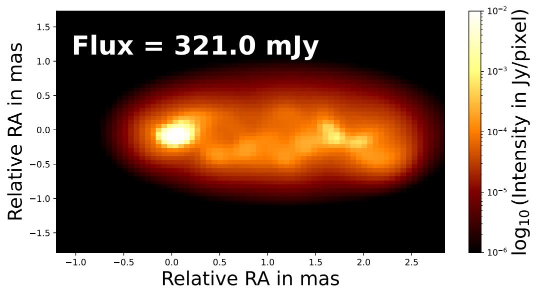

(d) Reconstructions at 43 GHz with a declination of 70°, 3 mas extend and 321 mJy total flux, in logarithmic scale.

Figure 4.18: Overview of the reconstructed images at 43 GHz with 3 mas extend and different intensities of the source.

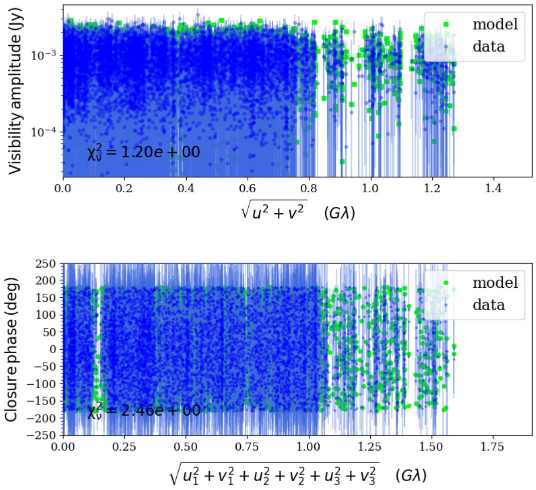

(a) Visibility amplitude and closure phase images at 0.3 mJy total flux and 43 GHz.

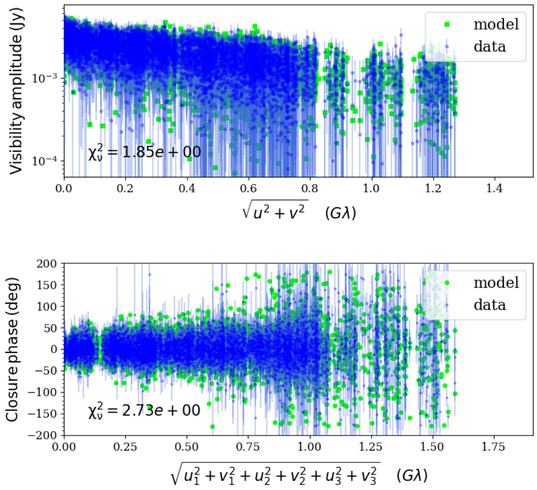

(b) Visibility amplitude and closure phase images at 3.2 mJy total flux and 43 GHz.

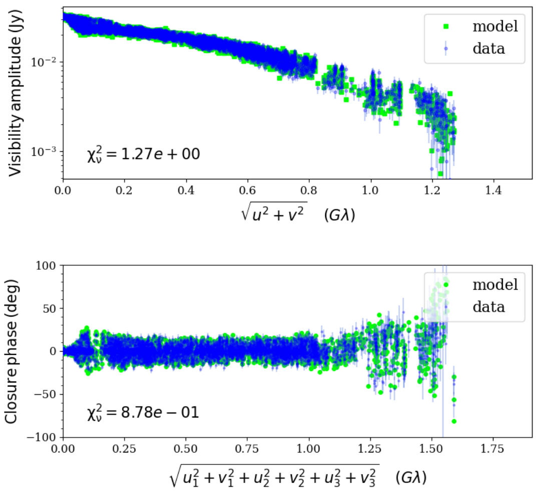

(c) Visibility amplitude and closure phase images at 32 mJy total flux and 43 GHz.

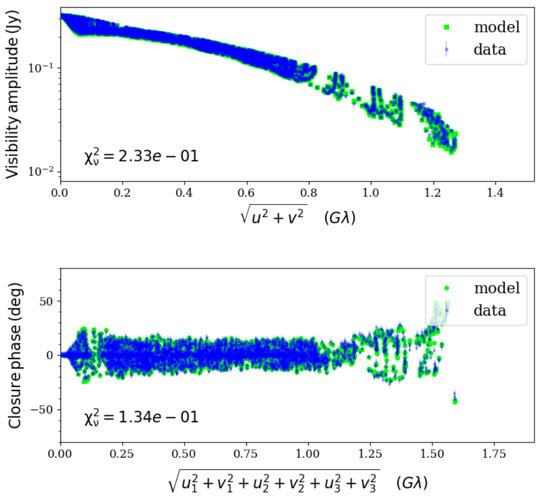

(d) Visibility amplitude and closure phase images at 321 mJy total flux and 43 GHz.

Figure 4.19: Overview of the visibility amplitudes and closure phase of the reconstructed images at 43 GHz with 3 mas extend and with different intensities of the source.

4.5.3 Reconstructions at 94 GHz

At 94 GHz, the declination was set to 70° and the source size to 1 mas. Since this is the frequency with the lowest SNR, no visible detection is possible at 0.2 mJy within the chosen dynamic range (see Fig.4.20a). At 2.1 mJy, only the core component is reconstructed, with no indication of a second component (see Fig.4.20b). At 21.4 mJy, Fig4.20c) both the core and the second component become visible, although the latter is very faint and the filamentary structure is not recovered. Only when the flux is increased to 214 mJy are all major features, including the filaments, reconstructed, as shown in Fig. 4.20d). The visibility amplitudes and closure phases for the two lowest-flux images (Fig.4.21a–b) are completely dominated by noise. In the higher-flux reconstructions (Fig.4.21c–d), the visibility amplitudes do not show a strong cutoff as observed at lower frequencies. The closure phases are evenly distributed around zero, with values up to 25°, and show less pronounced scattering at long baselines compared to the previous cases.

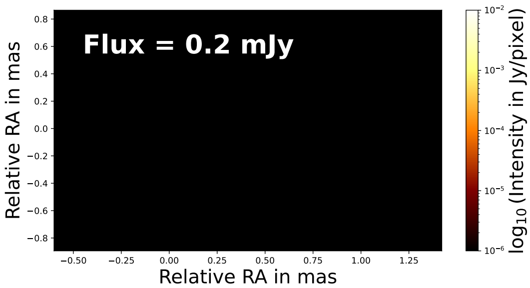

(a) Reconstructions at 94 GHz with a declination of 70°, 1 mas extend and 0.2 mJy total flux, in logarithmic scale.

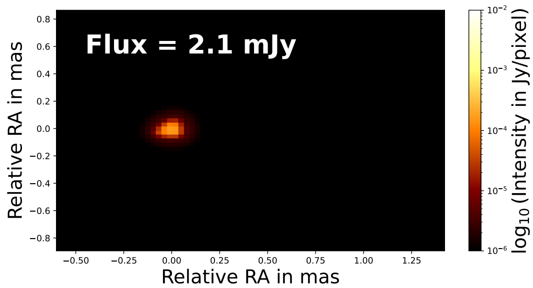

(b) Reconstructions at 94 GHz with a declination of 70°, 1 mas extend and 2.1 mJy total flux, in logarithmic scale.

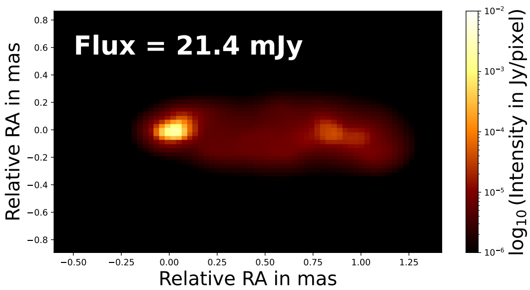

(c) Reconstructions at 94 GHz with a declination of 70°, 1 mas extend and 21.4 mJy total flux, in logarithmic scale.

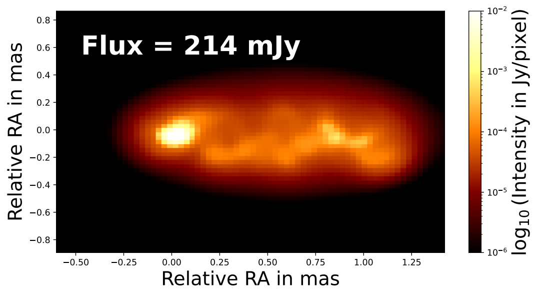

(d) Reconstructions at 94 GHz with a declination of 70°, 1 mas extend and 214 mJy total flux, in logarithmic scale.

Figure 4.20: Overview of the reconstructed images at 94 GHz with 1 mas extend and different intensities of the source.

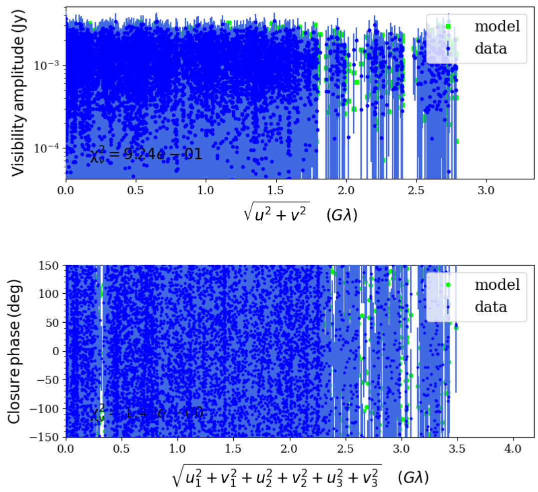

(a) Visibility amplitude and closure phase images at 0.2 mJy total flux and 94 GHz.

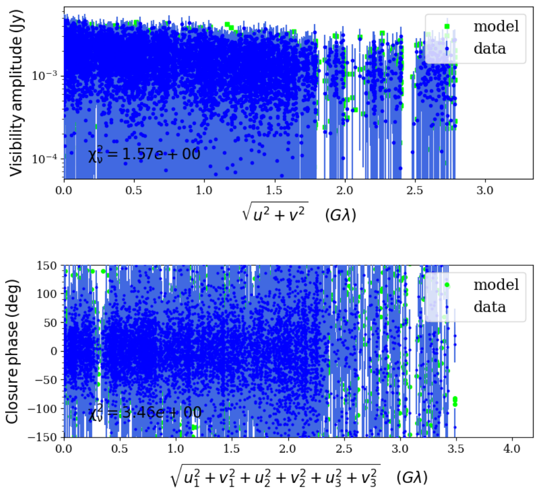

(b) Visibility amplitude and closure phase images at 2.1 mJy total flux and 94 GHz.

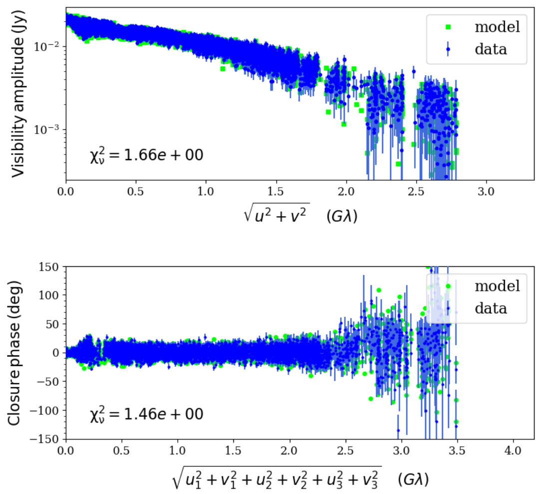

(c) Visibility amplitude and closure phase images at 21 mJy total flux and 94 GHz.

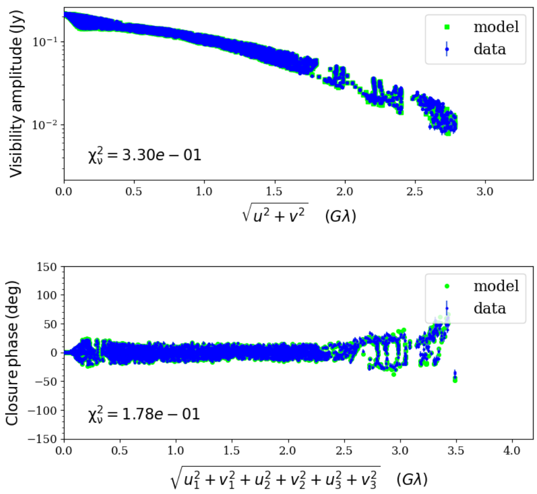

(d) Visibility amplitude and closure phase images at 214 mJy total flux and 94 GHz.

Figure 4.21: Overview of the visibility amplitudes and closure phase of the reconstructed images at 94 GHz with 1 mas extend and with different intensities of the source.

4.6 LEVERAGE reconstructions at 94 GHz

4.6.1 Variation in the declination of the source

Now, German stations were added to the ngVLA array. First, source reconstruction at different declinations were conducted. The reconstructions used the same parameters as in the 94 GHz ngVLA case: a total flux of 21.4 mJy and a source size of 1.5 mas. Despite the low flux, the core region is reconstructed well, and the second component is also clearly detected (see Fig.4.22). Although the inner filaments remain difficult to discern, they are definitely visible. At a declination of 70° (see Fig.4.22d), finer structures within the second component become resolved compared to the 94 GHz ngVLA-only observations. However, visual inspection reveals no substantial overall improvement over the ngVLA reconstructions. The uv coverage, shown in Fig.4.23a–d, is noticeably enhanced compared to the ngVLA alone (Fig.4.9a–d). By adding the German stations, the uv baselines become more extended, and the overall coverage improves due to the increased number of baselines. The visibility amplitudes and closure phases contain significantly more data and longer baselines (see Fig.4.23e–h). Similar to the ngVLA-only reconstructions, visibility amplitudes show a strong decrease beyond 1.5 $G\lambda$, and closure phases exhibit high scatter at longer baselines - reaching over 100° compared to about 50° at shorter baselines.

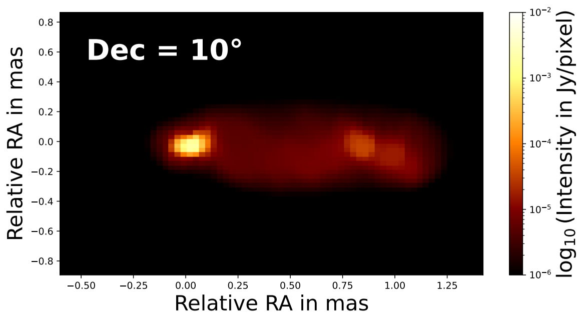

(a) Reconstruction at 94 GHz with a declination of 70° and 21 mJy total flux, in logarithmic scale.

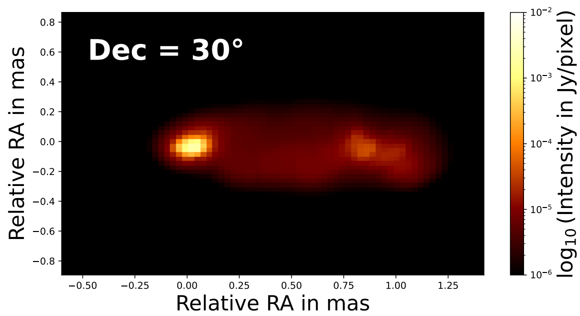

(b) Reconstruction at 94 GHz with a declination of 70° and 21 mJy total flux, in logarithmic scale.

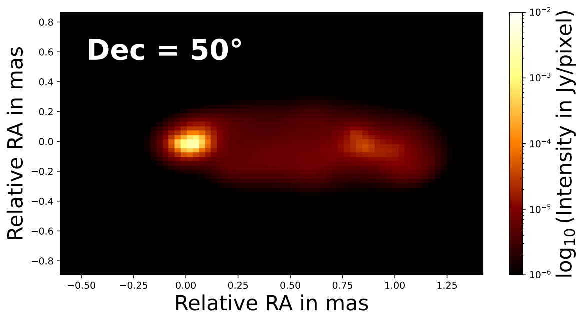

(c) Reconstruction at 94 GHz with a declination of 70° and 21 mJy total flux, in logarithmic scale.

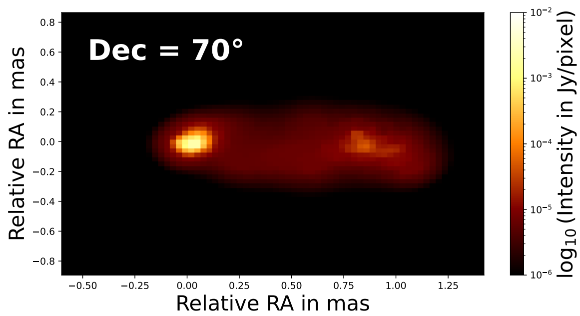

(d) Reconstruction at 94 GHz with a declination of 70° and 21 mJy total flux, in logarithmic scale.

Figure 4.22: Overview of the reconstructed images at 94 GHz with 21 mJy total flux at different declinations.

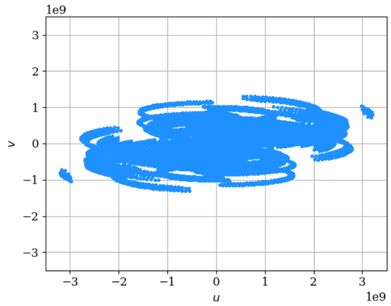

(a) Uv plot at a declination of 10° at 94 GHz.

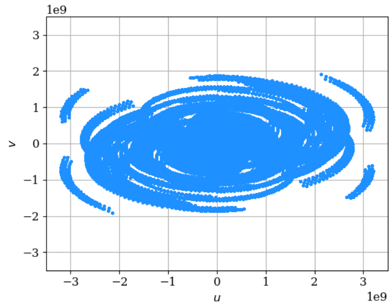

(b) Uv plot at a declination of 30° at 94 GHz.

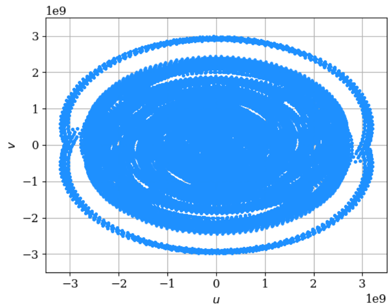

(c) Uv plot at a declination of 50° at 94 GHz.

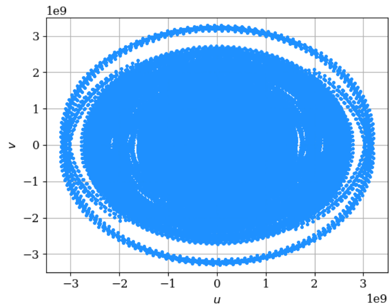

(d) Uv plot at a declination of 70° at 94 GHz.

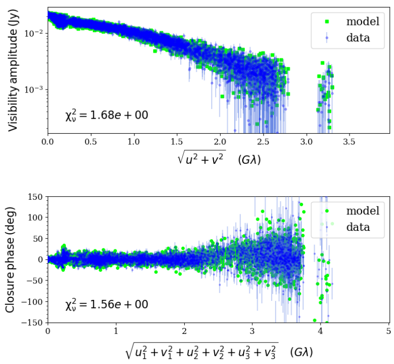

(e) Visibility amplitude and closure phase images at a declination of 10° at 94 GHz.

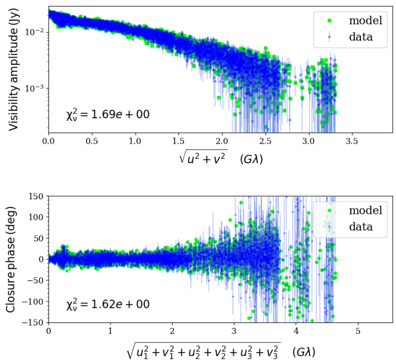

(f) Visibility amplitude and closure phase images at a declination of 30° at 94 GHz.

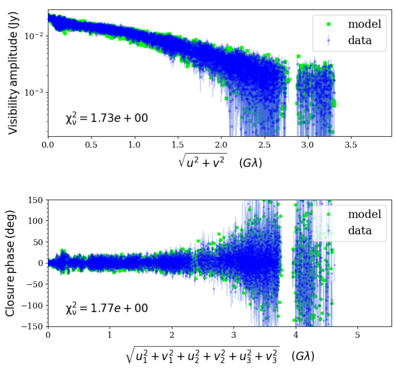

(g) Visibility amplitude and closure phase images at a declination of 50° at 94 GHz.

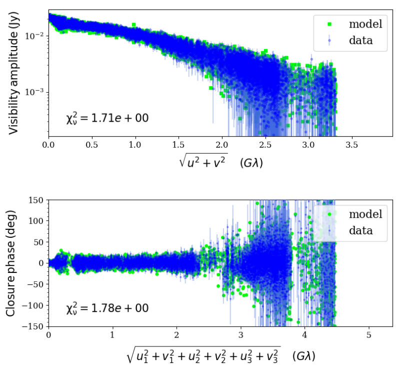

(h) Visibility amplitude and closure phases images at a declination of 70° at 94 GHz.

Figure 4.23: Overview of the uv coverages, visibility amplitudes and closure phase of the reconstructed images at 94 GHz with 21 mJy total flux at different declinations.

4.6.2 Variation in the length of the source

The source reconstructions, performed at a declination of 70° with German stations and a total flux of 21.4 mJy, show slightly better resolution compared to the ngVLA alone (see Fig.4.14). Aside from the second component being depicted in greater detail for the 1.5 mas source - Fig.4.24d) - no significant improvements are observed. The visibility amplitudes and closure phases contain substantially more data and exhibit behavior similar to other 94 GHz reconstructions. At a source size of 0.3 mas, see Fig.4.25a), there is no pronounced cutoff in visibility amplitudes, which remain roughly constant. In contrast, for source sizes of 1.0 mas and 1.5 mas, Fig.4.24c)–d), visibility amplitudes show a stronger decline starting at approximately 2.5 $G\lambda$. Closure phases are distributed evenly around zero within a range of approximately ±25°. For the 1.5 mas source, they begin to scatter more widely beyond 3 $G\lambda$, reaching values up to ±200°.

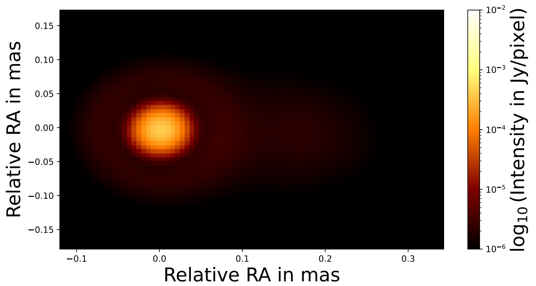

(a) Reconstructions at 94 GHz with a declination of 70°, 21 mJy total flux and 0.3 mas extend, in logarithmic scale.

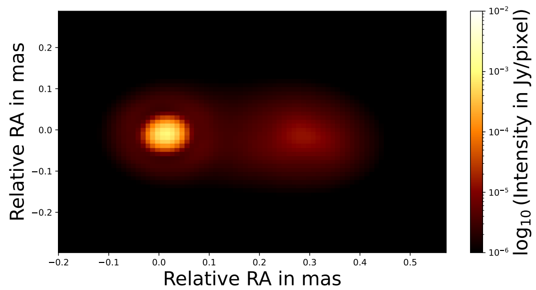

(b) Reconstructions at 94 GHz with a declination of 70°, 21 mJy total flux and 0.5 mas extend, in logarithmic scale.

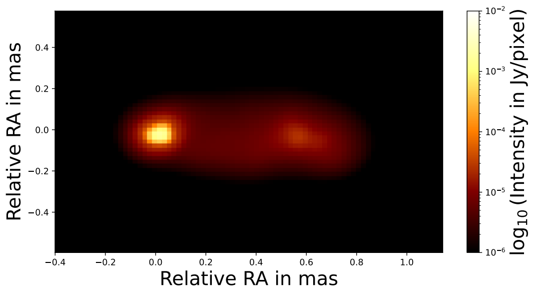

(c) Reconstructions at 94 GHz with a declination of 70°, 21 mJy total flux and 1.0 mas extend, in logarithmic scale.

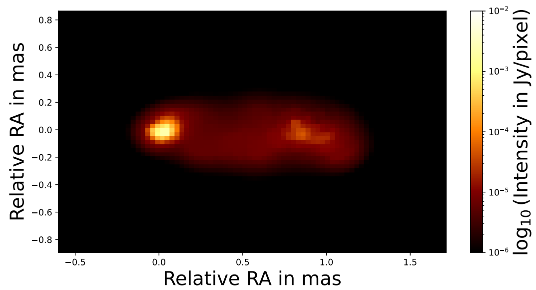

(d) Reconstructions at 94 GHz with a declination of 70°, 21 mJy total flux and 1.5 mas extend, in logarithmic scale.

Figure 4.24: Overview of the reconstructed images at 94 GHz, 21 mJy total flux and different sizes of the source.

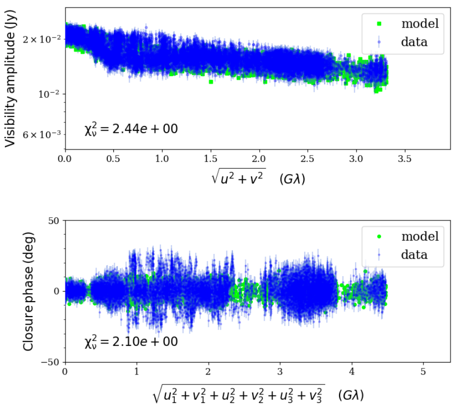

(a) Visibility amplitude and closure phase images at a length of 0.3 mas at 94 GHz.

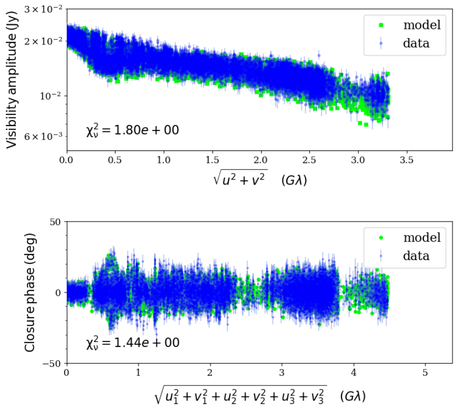

(b) Visibility amplitude and closure phase images at a length of 0.5 mas at 94 GHz.

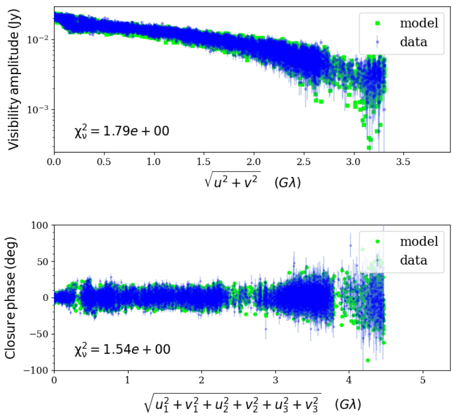

(c) Visibility amplitude and closure phase images at a length of 1.0 mas at 94 GHz.

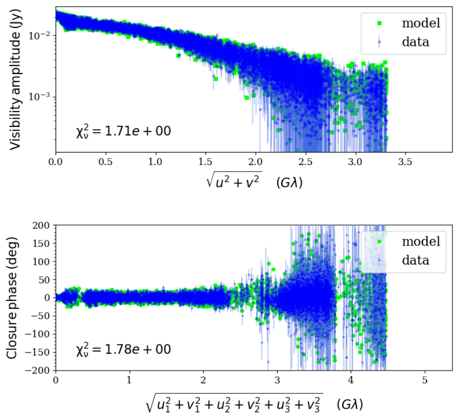

(d) Visibility amplitude and closure phase images at a length of 1.5 mas at 94 GHz.

Figure 4.25: Overview of the visibility amplitudes and closure phases of the reconstructed images at 94 GHz with 21 mJy total flux at different lengths of the source.

4.6.3 Variation of the intensity of the source

The reconstructions at 94 GHz with the German stations were performed at a declination of 70° and a source size of 1.5 mas, while varying the flux density, as shown in Fig.4.26. The results closely resemble those obtained with the ngVLA alone at 94 GHz (see Fig.4.20). At 0.2 mJy, no source is visible due to the set dynamic range. At 2.1 mJy, the core structure becomes recoverable. The image at 21.4 mJy matches the one discussed previously in Fig.4.22, where both components and even inner structures are clearly resolved. At a flux density of 214 mJy, the source is reconstructed almost perfectly. None of the images show significant improvements compared to the ngVLA-only reconstructions. The visibility amplitudes and closure phases in the low-flux images (Fig.4.27a–b) are dominated by noise. At 21.4 mJy, the amplitude exhibits a pronounced decrease starting near 2 $G\lambda$, accompanied by significant noise, which is less pronounced in the 214 mJy case. Closure phases at 21.4 mJy begin to scatter strongly beyond 3 $G\lambda$, reaching values up to 150° and beyond, whereas for 214 mJy the closure phases remain more stable.

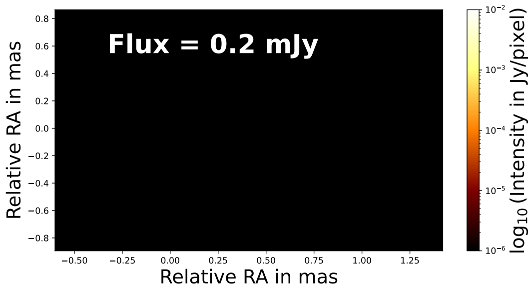

(a) Reconstructions at 94 GHz with a declination of 70°, 1 mas extend and 0.21 mJy total flux, in logarithmic scale.

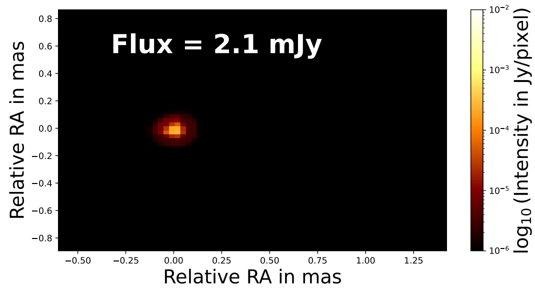

(b) Reconstructions at 94 GHz with a declination of 70°, 1 mas extend and 2.14 mJy total flux, in logarithmic scale.

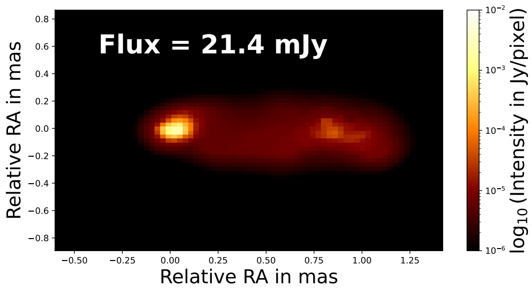

(c) Reconstructions at 94 GHz with a declination of 70°, 1 mas extend and 21.4 mJy total flux, in logarithmic scale.

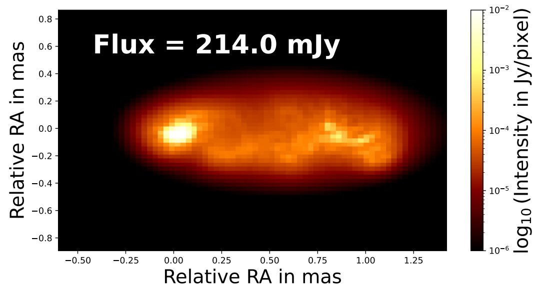

(d) Reconstructions at 94 GHz with a declination of 70°, 1 mas extend and 214 mJy total flux, in logarithmic scale.

Figure 4.26: Overview of the reconstructed images at 94 GHz with 1 mas extend and different intensities of the source.

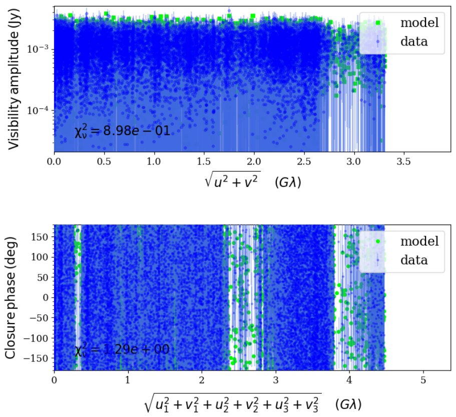

(a) Visibility amplitude and closure phase images at 0.21 mJy total flux and 94 GHz.

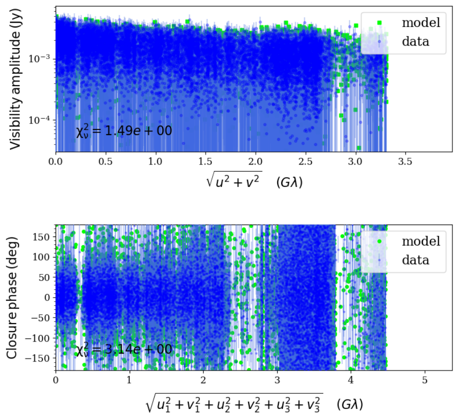

(b) Visibility amplitude and closure phase images at 2.14 mJy total flux and 94 GHz.

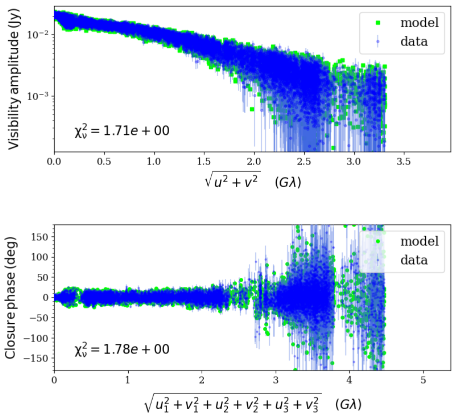

(c) Visibility amplitude and closure phase images at 21.4 mJy total flux and 94 GHz.

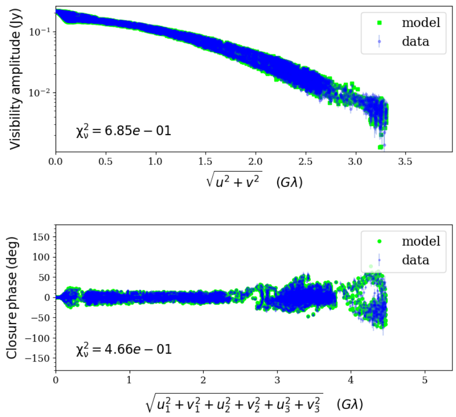

(d) Visibility amplitude and closure phase images at 214 mJy total flux and 94 GHz.

Figure 4.27: Overview of the visibility amplitudes and closure phases of the reconstructed images at 94 GHz with 1 mas extend and with different intensities of the source.

4.7 M87 reconstructions

4.7.1 Motivation and numerical setup

As discussed in the previous chapter, the addition of German stations did not lead to substantial improvements in the reconstruction results. This is mainly due to the small beam size, which becomes more critical when resolving finer structures. To further enhance the capabilities of the LEVERAGE program, another source was reconstructed - namely M87 - shown in Fig.4.28. These reconstructions focus on much smaller scales (around 0.2 mas rather than 1–5 mas), allowing the small beam of the GngVLA array (see Tab.4.3) to fully exploit its strengths.

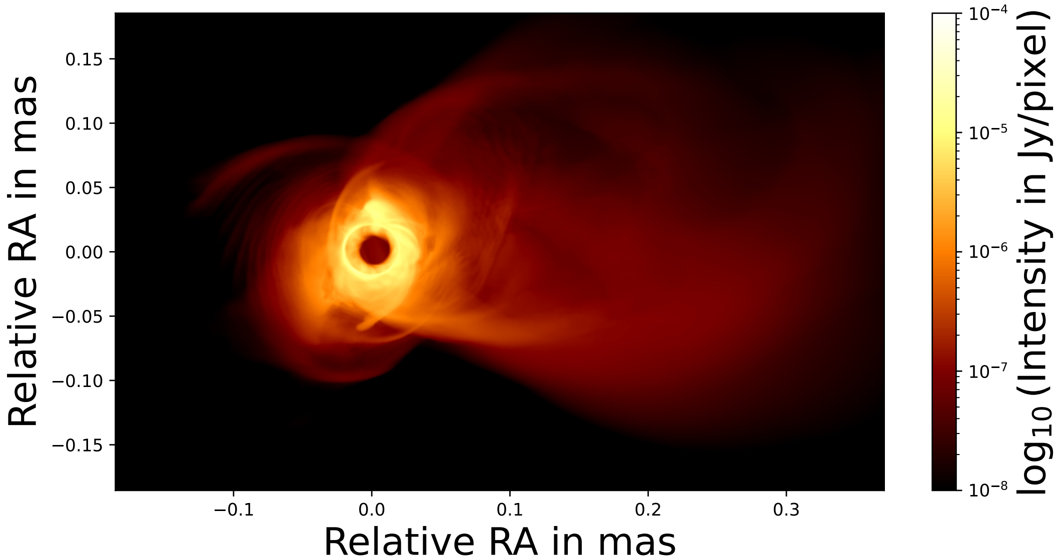

Figure 4.28: Source model of M87 with 0.3 mas extend and 960 mJy total flux.

Reconstructions were carried out at 86 GHz with different arrays, where iteratively more telescopes were added to the ngVLA array (see Fig. 4.30). The stations are listed in Tab. 4.2; these include not only German stations but also one station in Hungary and several in Scandinavia. The synthetic data were generated in the same way as for the helical model in Ch. 4.1, with only thermal noise added. The data were averaged into 1-hour bins (3600 s) to reduce numerical effort, as the reconstructions were performed with 600 pixels to resolve all possible structures. For the reconstruction process, the same regularizers as in Ch. 4.1 were used, but here all were applied simultaneously instead of in two steps as done for the helical model. The image's total flux was set as the zero-baseline flux, and Gaussians were used as priors: tiny ones to avoid singularities and large ones (nearly the whole image plane) as top hats to capture extended emission within the field of view (FOV). The final results are shown in Fig. 4.30a) - d).

4.7.2 M87 reconstruction with different arrays

Visual inspection alone reveals the improvements due to the additional telescopes compared to the ngVLA array. Without the extension, it is not possible to resolve the ring of M87. However, adding the German antennas enables the extraction of the ring size and thus the determination of the black hole mass. The inclusion of the Hungarian station further supports the determination of the ring, and the emission hot spot at the lower end of the ring appears more dominant compared to the reconstructions with only German stations. Adding the Scandinavian stations, however, degrades the result somewhat: the ring can still be guessed, but is not clearly reconstructed anymore.

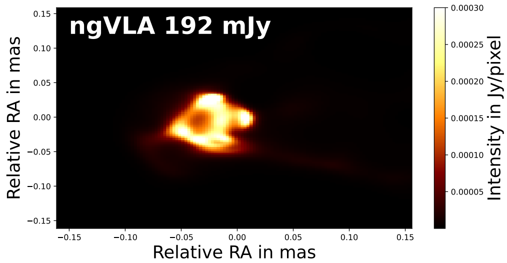

(a) M87 reconstructed with ngVLA array - shown in linear scale.

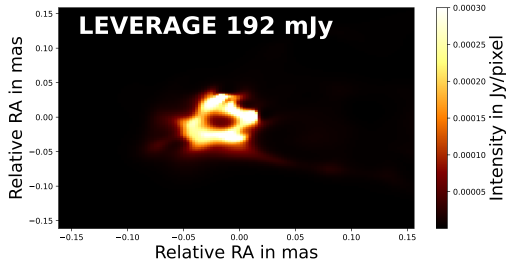

(b) M87 reconstructed with LEVERAGE array - shown in linear scale.

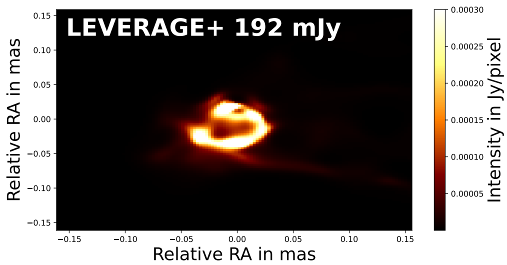

(c) M87 reconstructed with LEVERAGE and Hungarian station - shown in linear scale.

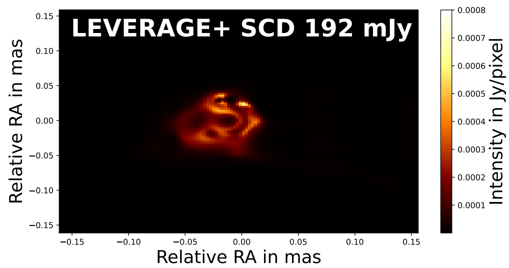

(d) M87 reconstructed with LEVERAGE, Hungarian and Scandinavian stations - shown in linear scale.

Figure 4.29: Overview of the reconstructed images of M87 with the different array configurations at 86 GHz with 0.3 mas extend at 70° declination and 192 mJy total flux.

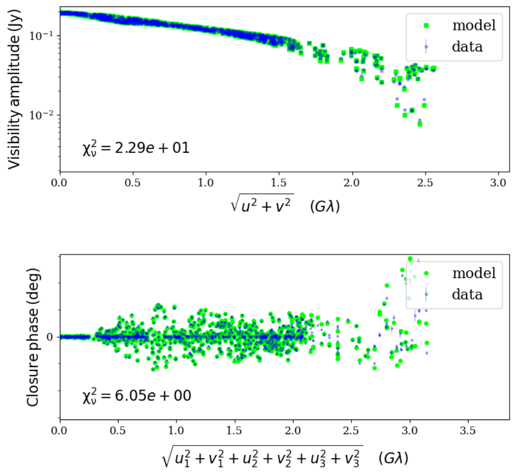

(a) Visibility amplitude and closure phases for the reconstruction of M87 with the ngVLA.

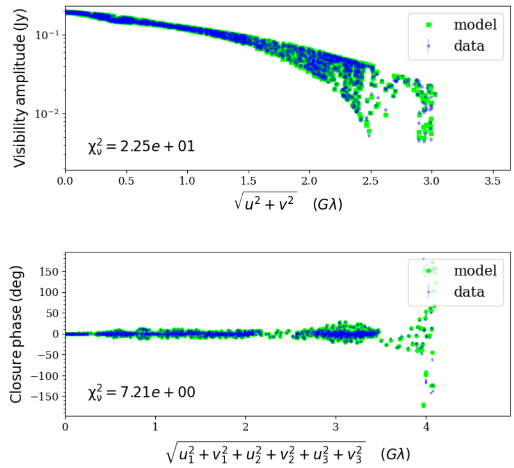

(b) Visibility amplitude and closure phases for the reconstruction of M87 with LEVERAGE.

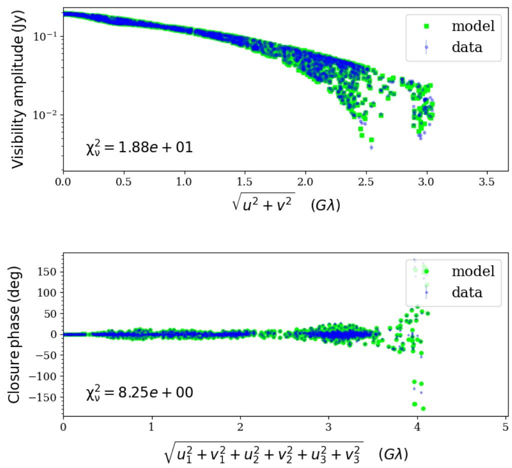

(c) Visibility amplitude and closure phases for the reconstruction of M87 with LEVERAGE+.

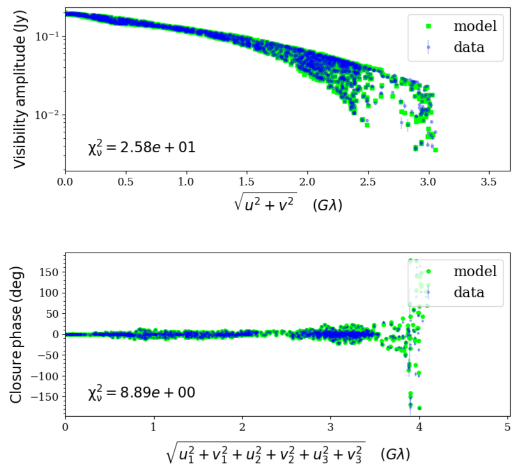

(d) Visibility amplitude and closure phases for the reconstruction of M87 with LEVERAGE+ and Scandinavian stations.

Figure 4.30: Overview of the visibility amplitudes and closure phases of M87 with the different array configurations at 86 GHz with 0.3 mas extend at 70° declination and 192 mJy total flux.

4.7.3 Variation in intensity of M87 - LEVERAGE reconstructions

For the final part, additional reconstructions of M87 were performed with LEVERAGE at 94 GHz, varying the source intensity with total fluxes ranging from 960 mJy down to 1.92 mJy, further enhancing the sensitivity of the upcoming arrays - shown in Fig4.31d)-a). Due to the set dynamic range, the images at 19.2 mJy and 1.92 mJy, are barely visible; however, as noted earlier, they are still detected since the RMS remains on the order of 1000. Upon closer inspection, the 19.2 mJy image still reveals a faint ring structure. This ring can be resolved and identified at this dynamic range in all images except for the 1.92 mJy case. The reconstructions at 192 mJy and 960 mJy are very good. The visibility amplitudes and closure phases exhibit good agreement between data and model, although the χ^2 values are all clearly above unity, indicating a poorer fit. In the 1.92 mJy case, the impact of thermal noise is evident, with large errorbars. Around 2 $G\lambda$, the source becomes resolved due to a strong decrease in visibility amplitude, which will be also discussed in the upcoming sections. The closure phase plots show a symmetrical behavior up to about 4 $G\lambda$, where significant scattering begins, indicating resolved asymmetries caused by different regions of the ring emitting varying amounts of flux. Additionally, the emitted jet of M87 could be captured, though it becomes visible only in a logarithmic intensity scale, as illustrated in Fig. 4.32. There, one can see the jet at higher fluxes and the ring also becomes visible at a total flux of 1.92 mJy.

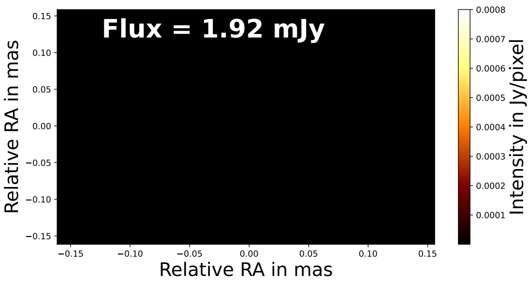

(a) M87 Reconstructions at 86 GHz with a declination of 70°, 0.3 mas extend and 1.92 mJy total flux, in linear scale

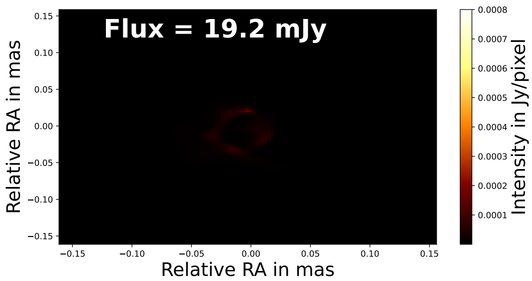

(b) M87 Reconstructions at 86 GHz with a declination of 70°, 0.3 mas extend and 19.2 mJy total flux, in linear scale

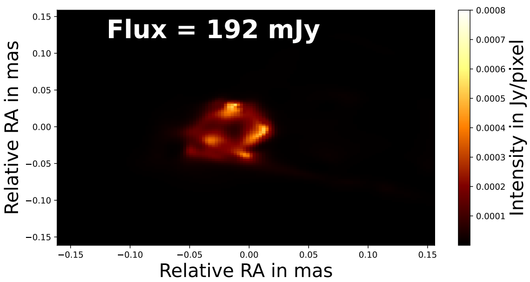

(c) M87 Reconstructions at 86 GHz with a declination of 70°, 0.3 mas extend and 192 mJy total flux, in linear scale

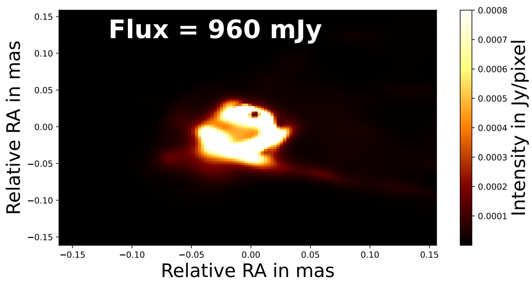

(d) M87 Reconstructions at 86 GHz with a declination of 70°, 0.3 mas extend and 960 mJy total flux, in linear scale

Figure 4.31: Overview of the reconstructed images of M87 with the LEVERAGE array at 86 GHz with 0.3 mas extend at 70° declination with different intensities of the source.

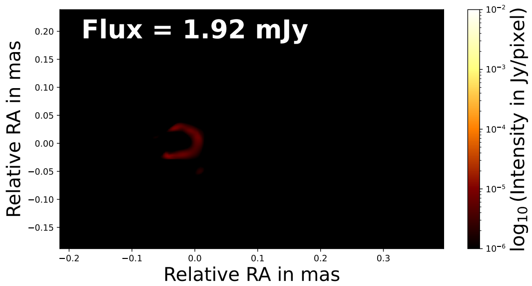

(a) M87 Reconstructions at 86 GHz with a declination of 70°, 0.3 mas extend and 1.92 mJy total flux, in logarithmic scale

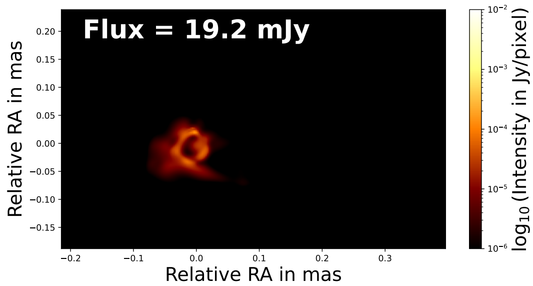

(b) M87 Reconstructions at 86 GHz with a declination of 70°, 0.3 mas extend and 19.2 mJy total flux, in logarithmic scale

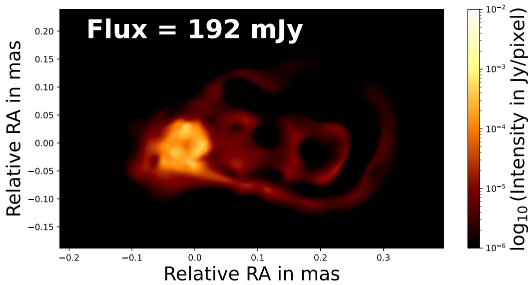

(c) M87 Reconstructions at 86 GHz with a declination of 70°, 0.3 mas extend and 192 mJy total flux, in logarithmic scale

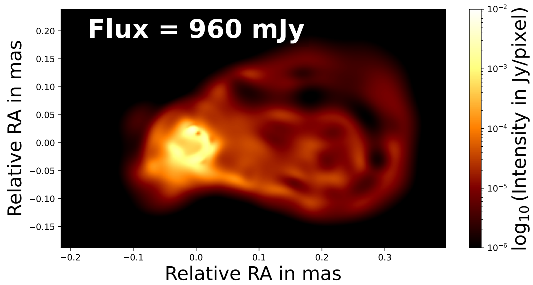

(d) M87 Reconstructions at 86 GHz with a declination of 70°, 0.3 mas extend and 960 mJy total flux, in logarithmic scale

Figure 4.32: Overview of the reconstructed images of M87 with the LEVERAGE array at 86 GHz with 0.3 mas extend at 70° declination with different intensities of the source in logarithmic scale to demonstrate the jet of M87.

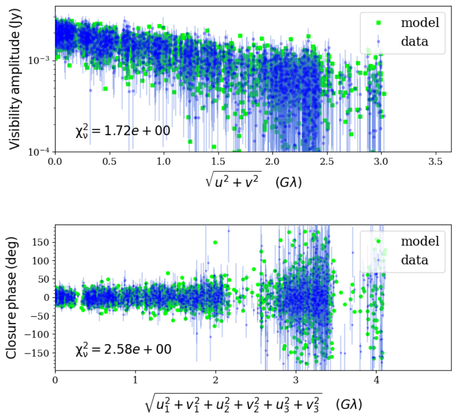

(a) Visibility amplitude and closure phase images at 1.92 mJy total flux and 86 GHz.

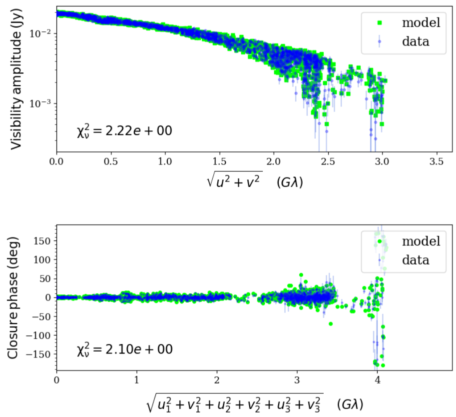

(b) Visibility amplitude and closure phase images at 19.2 mJy total flux and 86 GHz.

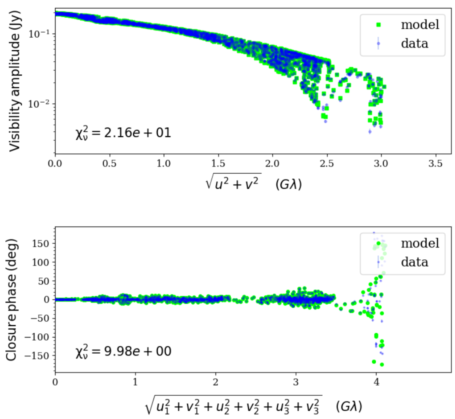

(c) Visibility amplitude and closure phase images at 192 mJy total flux and 86 GHz.

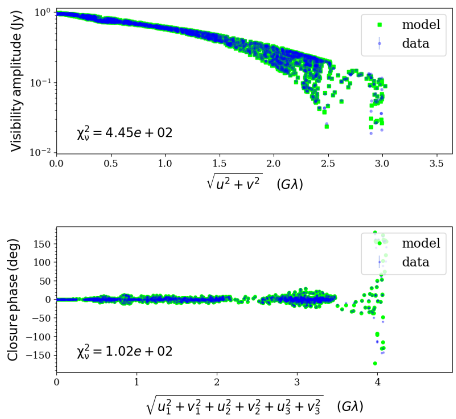

(d) Visibility amplitude and closure phase images at 960 mJy total flux and 86 GHz.

Figure 4.33: Overview of the visibility amplitudes and closure phase of the reconstructed images of M87 with the LEVERAGE array at 86 GHz with 1 mas extend and with different intensities of the source.

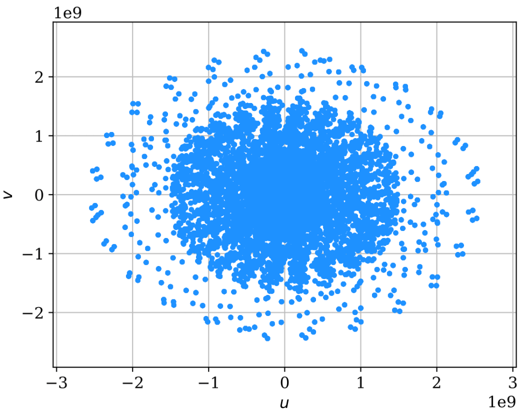

(a) UV plot of the ngVLA array at a declination of 70° at 86 GHz.

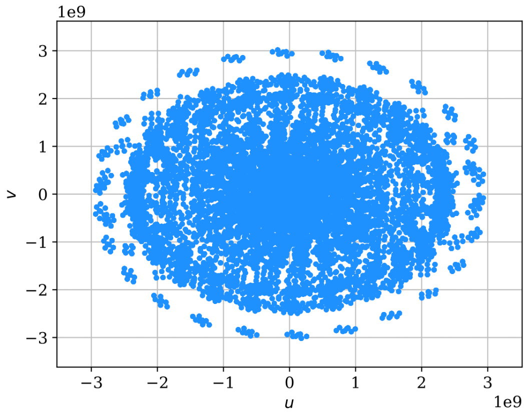

(b) UV plot of the LEVERAGE array at a declination of 70° at 86 GHz.

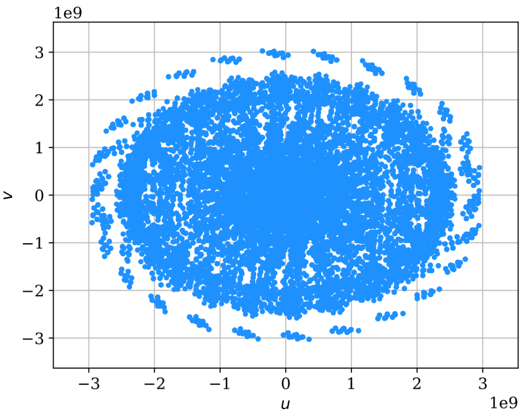

(c) UV plot of the LEVERAGE+ array at a declination of 70° at 86 GHz.

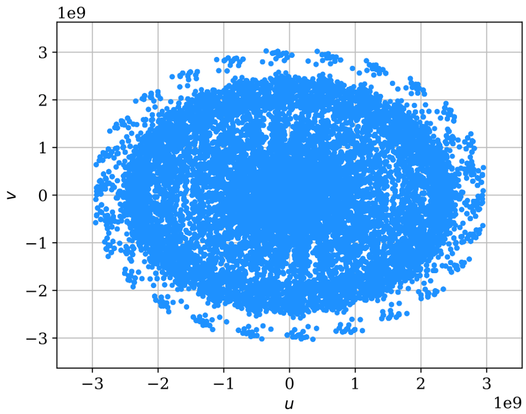

(d) UV plot of the LEVERAGE+ array with Scandinavian stations at a declination of 70° at 86 GHz.

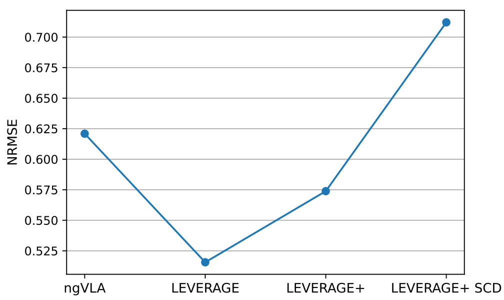

(e) NRMSE of M87 reconstructed with different arrays.

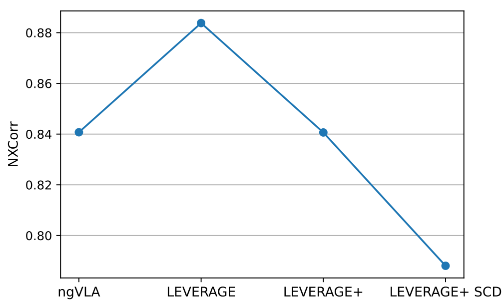

(f) NXCorr of M87 reconstructed with different arrays.

Figure 4.34: Overview of the uv plots and metrics of M87 reconstructions with different array configurations at 86 GHz, using a source extent of 0.3 mas, a declination of 70°, and a total flux of 192 mJy.

4.7.4 Discussion of the M87 reconstructions

The best results are achieved with LEVERAGE and LEVERAGE+, as confirmed by the visibility amplitude plots and closure phases, see Fig.4.33. However, adding the Scandinavian stations slightly degrades the results. This is likely due to the high SEFD of the Scandinavian antennas, which directly increases visibility errors and, consequently, the noise level (see Eq.1.4.18). The SEFD of the Scandinavian stations is approximately 17 times larger than that of the planned ngVLA telescopes. Furthermore, because these stations are located at high latitudes, they observe almost continuously, adding noise throughout the entire dataset. Given the comparable beam sizes - the smallest beam of LEVERAGE+ SCD is only 0.0025 mas smaller than that of LEVERAGE (see Tab.4.3) - no significant improvement in resolution is observed or expected. The additional stations, particularly the German ones, improve the uv coverage, especially at longer baselines (see Fig. 4.34). The χ^2 values for visibility amplitudes and closure phases are relatively high (around 2.3 for visibilities and 7 for closure phases), suggesting a poor model fit. However, this is due to the high data sampling, which reduces the data points and - because no additional systematic noise was added - the uncertainties are very small. Consequently, the χ^2 values are extremely sensitive to minor deviations from the model. Adding more data would likely reduce these χ^2 values. Visually, the model matches the data well and appears reliable - the same argument accounts for the reconstructions with different intensities. This is confirmed by the image metrics in Fig. 4.34e) and Fig. 4.34f), where the NRMSE and NXCorr values are shown. The best result is achieved with the ngVLA plus German stations array, which shows the smallest pixel-to-pixel difference (NRMSE) and the highest overall structural agreement (NXCorr). In contrast, the worst result is found for the observation including the Scandinavian stations, due to their high SEFD as discussed. These findings underline the importance of additional German stations in improving image quality and resolving critical source structure.

4.8 Discussion of the reconstructions

The first inspection of the reconstructed images can be made based on their visual appearance. For all reconstructions, the minimum flux values that could be reliably reconstructed were first determined by varying the intensity of the source. These minimum flux values were then used as reference points for further reconstructions. For example, at 94 GHz, the minimum flux that could be properly reconstructed was around 21 mJy. Consequently, the reconstructions involving variations of the declination and size were conducted using this flux value. Since a declination of 70° provides the best uv-plane coverage, this value was chosen as a reference for the other reconstructions. The reference source size was determined by identifying the source size that produced the best reconstruction results. In addition to the visual inspection of the images, χ^2 values for visibility amplitudes and closure phases (introduced in Ch. 1.4.4) were calculated by comparing the synthetic observational data to the assumed model according to

$$\chi^2_{\nu,\mathrm{CP}} = \frac{2}{N} \sum_{i=1}^{N} \frac{1 - \cos\left(\left(\phi_i^{\mathrm{obs}} - \phi_i^{\mathrm{mod}}\right) \cdot \frac{\pi}{180}\right)}{\left(\sigma_{\phi,i} \cdot \frac{\pi}{180}\right)^2} \tag{4.8.1}$$

for the closure phases and

$$\chi^2_{\nu,\mathrm{amp}} = \frac{1}{N} \sum_{i=1}^{N} \left(\frac{A_i^{\mathrm{obs}} - A_i^{\mathrm{mod}}}{\sigma_{A,i}}\right)^2 \tag{4.8.2}$$

for the visibility amplitudes. Furthermore, image metrics following Chael et al. (2016) were also computed to quantitatively assess the quality of the reconstructions. Here, the final reconstructed image was compared to the initial input image by means of the normalized root-mean-square error metric

$$\mathrm{NRMSE} = \sqrt{\frac{\sum_{x,y} |I_1(x,y) - I_2(x,y)|^2}{\sum_{x,y} |I_1(x,y)|^2}} \tag{4.8.3}$$

The NRMSE is a point-to-point metric that evaluates images based on pixel-to-pixel similarities rather than common large-scale features. In addition, the normalized correlation function was used, which is given by:

$$\mathrm{NXCorr} = \frac{\max_{i,j} \Re\left[\mathcal{F}^{-1}\left(\mathcal{F}(I_1) \cdot \mathcal{F}(I_2)^*\right)\right]}{N_x \cdot N_y} \tag{4.8.4}$$

where N_x and N_y are the image pixels in the x- and y-axis (256 pixels in each direction in all reconstructions), I_1 is the reconstructed image and I_2 in the initial model - are the two compared images which in this case were Fourier transformed to reduce computational effort. NXCorr is aimed to compare the general structural similarities. It offers the advantage of being unaffected by the absolute position of the source centroid and the overall flux level, enabling a more equitable comparison between visibility-based and closure-only image reconstructions Lai et al. (2025).

4.8.1 Declination of the source

The χ^2 values shown in Figs.4.35 and 4.36 remain mostly unchanged across all declinations within each frequency band. The lowest values are observed at 15 GHz, while the highest occur at 94 GHz for the ngVLA reconstructions including German stations, both in closure phases and visibility amplitudes. This behavior can be explained by the varying source intensities at different frequencies, as attributed to the spectral energy distribution (SED) shown in Fig.3.1f). At lower flux levels, the signal-to-noise ratio (SNR) decreases due to the increased relative contribution of thermal noise, leading to larger differences between data and model and thus higher χ^2 values. Although the uv coverage improves at higher frequencies - since baselines scale with frequency - resulting in more data points, this also increases the potential for deviations. The inclusion of German stations further increases the number of baselines, thus adding even more data points to fit, which explains the increased χ^2 values in these cases. While the χ^2 values at each frequency are generally comparable across declinations, the highest values consistently occur at 70°. Notably, even if visual differences in reconstructions are minor, the uv coverage at 70° provides the most comprehensive information. Here, the source is sampled fairly evenly in all directions (east-west and north-south), unlike at lower declinations such as 10°, where data coverage is mostly along the u-axis with less extension in the v-axis. This uniform coverage is critical for accurately capturing source symmetry, as reflected in the closure phases. For a perfectly symmetric source, closure phases would be zero. As discussed earlier, the closure phases mostly scatter around zero up to about 50°, indicating a generally symmetric structure. However, beyond a certain baseline length, the closure phases deviate strongly from zero, signaling source asymmetry. On shorter baselines (corresponding to larger spatial scales), the source appears symmetric, but on longer baselines (finer scales), asymmetries arise due to flux differences between the upper and lower parts of the image's filaments, caused by Doppler boosting or multiple jet components. Hence, the best results are achieved at 70° declination because it provides the richest source information. The visibility amplitudes also exhibit a complex structure characteristic of a jet - unlike the simpler Bessel function pattern expected from an idealized black hole. The fit between data and model is very good at shorter baselines, with small deviations at longer baselines, where uv coverage is sparser and uncertainties grow. The pronounced drop in visibility amplitude with baseline length reflects the interferometer's resolving power. When the source size is comparable to or smaller than the beam size, the source appears unresolved and visibility amplitude remains nearly constant. As baseline length increases and the source becomes resolved, the amplitude decreases, indicating detection of spatial structure. A steep amplitude drop implies extended or complex morphology - such as multiple components, filaments, or a jet with substructure. Interference from these distinct source regions causes modulations in the visibility function, observed as amplitude drops or oscillations. The metrics shown in Figs. 4.37 and 4.38 further support that reconstructions generally improve with increasing declination. For nearly every frequency, the best normalized cross-correlation (NXCorr) occurs at 70°, except at 15 GHz, where values are similar across declinations. In reconstructions including German stations, the metrics at both 50° and 70° are very close to unity, indicating excellent alignment with the source and better performance than at lower declinations. However, these metric changes are below 5%, which is within expected uncertainties from thermal and systematic noise. The normalized root-mean-square error (NRMSE) is significantly better - up to 50% improvement - when German stations are included, especially at higher declinations, indicating more accurate reconstructions in terms of dataset differences. Overall, the fits are very good, with χ^2 values around unity, and declination effects are minor across frequencies. The richest data coverage is achieved at 70°, confirmed by both visual inspection and metrics. While German station inclusion results in only subtle visual improvements, the metrics indicate a clearer enhancement in reconstruction quality.

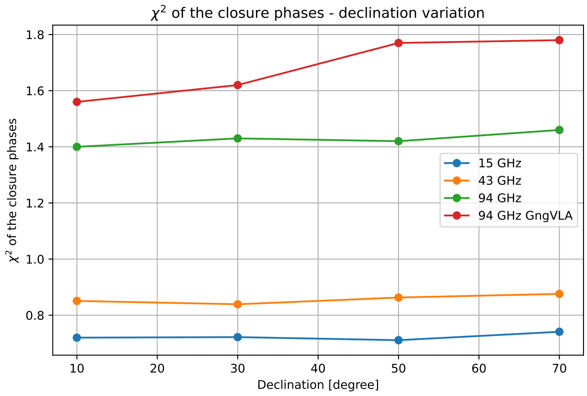

Figure 4.35: χ^2 of the closure phases on declination for each frequency of the ngVLA and 94 GHz for the ngVLA with German stations (GngVLA).

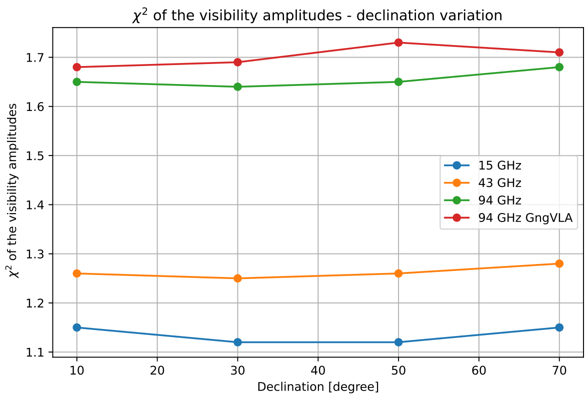

Figure 4.36: χ^2 of the visibility amplitudes on declination for each frequency of the ngVLA and 94 GHz for the ngVLA with German stations (GngVLA).

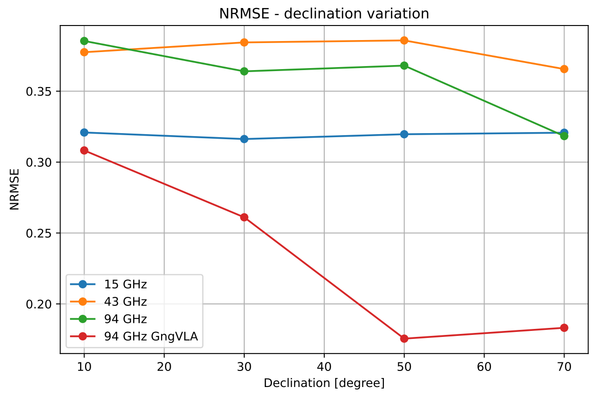

Figure 4.37: NRMSE on declination for each frequency of the ngVLA and 94 GHz for the ngVLA with German stations (GngVLA).

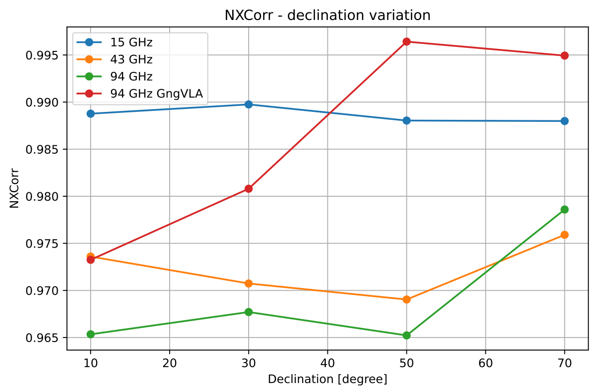

Figure 4.38: NXCorr on declination for each frequency of the ngVLA and 94 GHz for the ngVLA with German stations (GngVLA).

4.8.2 Size of the source

The next parameter varied is the size of the source. Here (see Sec.4.4.1), there are bigger differences in the visual appearance compared to the declination variation, which makes complete sense. The ability of an array to resolve certain structures depends on the size of its beam - its maximum angular resolution (see Eq.1.4.2). For 15 GHz, the beam is around 0.7 mas. With this beam size, small fine structures, such as filaments in a source with a total size of around 1 mas, cannot be resolved. The beam parameters summarized for every array configuration are shown in Tab. 4.3. However, the χ^2 values suggest a very good fit, as the values for closure phases and visibilities are both around unity. This makes sense because both the data and the model are limited by the beam and thus can only represent what the beam “sees,” successfully reconstructing that structure. Although the χ^2 values suggest a good fit, the metrics reveal a different picture (see

Fig.4.41 and Fig.4.42). The NRMSE is very high (above 3.5) compared to the source model, indicating that the model is not a good match overall. The same applies to the correlation metric NXCorr, where the values for a 1 mas source at 15 GHz are below 0.6. By increasing the source size, finer structures become visible because they are now within the range of the beam's size (around 0.7 mas). The best visual appearance is achieved at a source size of roughly 6–7 mas. Since there is a good SNR, all χ^2 values for every source size remain near unity, improving slightly for larger source sizes as previously discussed. As the source size increases, the metrics also improve. With a beam size of around 0.25 mas at 43 GHz - nearly three times smaller than at 15 GHz - smaller structures can be captured. The χ^2 values still suggest a good fit for both closure phases and visibility amplitudes at all source sizes and remain largely unchanged. However, because the total flux is lower, there is a higher thermal noise fraction and larger deviations between data and model, especially at longer baselines. The metrics behave analogously to the 15 GHz case, improving with larger source sizes and reaching their best values at 6–7 mas. Notably, the reconstruction at 4–5 mas already gives nearly identical metric results, representing a very good reconstruction in both cases. At 94 GHz, the beam size is around 0.12 mas, allowing even smaller features to be resolved. The χ^2 values deviate more from unity - around 1.6 for the visibility amplitudes and around 1.35 for the closure amplitudes, due to even lower SNR and more dominant thermal noise fraction - but still remain within a reasonable range. Especially at longer baselines, there are bigger deviations from the data. Examining the metrics, the best values are found for a source size of 1.5 mas, confirming the visual inspection. The NRMSE is comparable to the most successful 15 GHz reconstruction, while the NXCorr is slightly worse than at 15 and 43 GHz, but still indicates a good reconstruction. Adding the German stations to the ngVLA further reduces the beam size to around 0.07 mas - almost half the size of the ngVLA alone. The χ^2 values are actually worse, caused by larger baselines which give more information of the source, as already discussed in previous sections. Nonetheless, both metrics improve: the NXCorr approaches unity, and the NRMSE drops to around 0.2 compared to the reconstruction with the ngVLA alone. In general, one can conclude that adding the German stations improves the reconstruction, especially in the outer, more extended structures of the jet. It is also interesting to note that the image at 15 GHz with a size of 7 mas (Fig.4.10d) looks very similar to the 3 mas source at 43 GHz (Fig.4.12b) and 1.5 mas source at 94 GHz (Fig.4.14d) image-wise as well as in the closure phases and visibility amplitudes (at least structure-wise), which is basically explained by the definition of the resolution Eq.1.4.2, but still. So if one wants more structure either the source has to be larger (or nearer to the observer) or one has to observe at higher frequencies. This is the reason why M87 and SgrA* among others are probed at larger frequencies than 116 GHz (maximum of the ngVLA). The ngVLA however is designed to complement ALMA at lower frequencies with higher resolution and ALMA itself can observe up to 950 GHz.

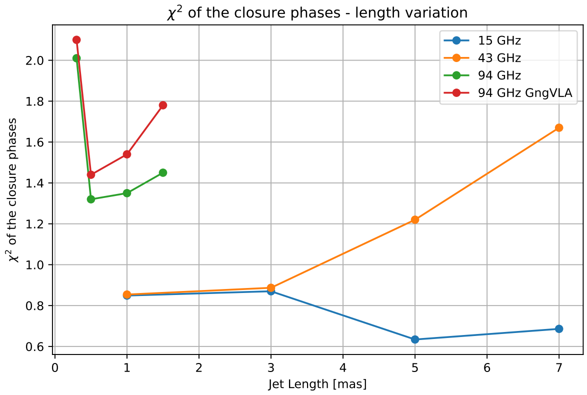

Figure 4.39: χ^2 of the closure phases on length for each frequency of the ngVLA and 94 GHz for the ngVLA with German stations (GngVLA).

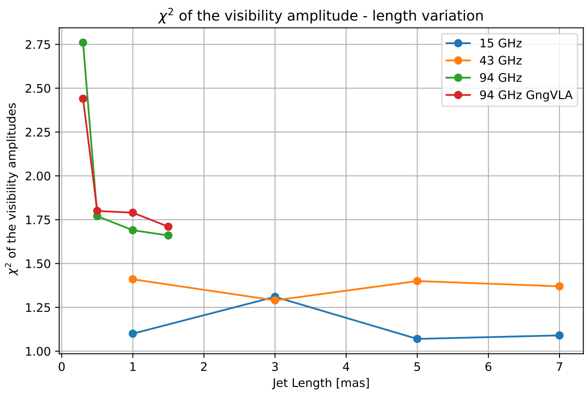

Figure 4.40: χ^2 of the visibility amplitudes on length for each frequency of the ngVLA and 94 GHz for the ngVLA with German stations (GngVLA).

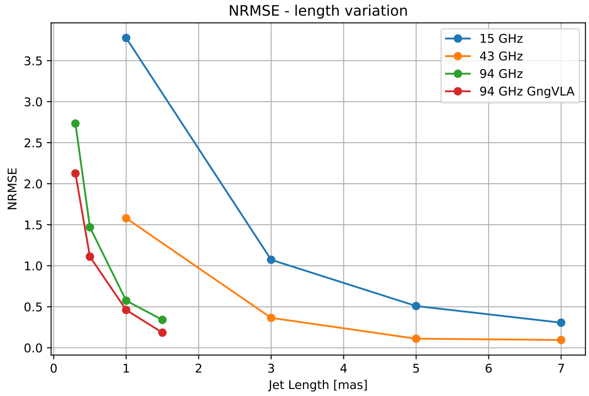

Figure 4.41: NRMSE on length for each frequency of the ngVLA and 94 GHz for the ngVLA with German stations (GngVLA).

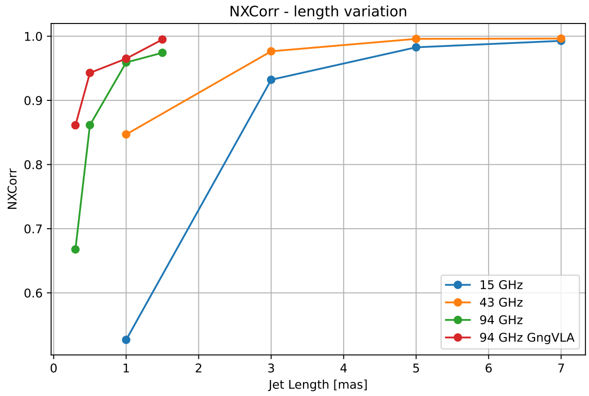

Figure 4.42: NXCorr on length for each frequency of the ngVLA and 94 GHz for the ngVLA with German stations (GngVLA).

4.8.3 Intensity of the source

As shown in Ch.4.5.1 and Figs.4.16d), 4.18d), and 4.20d), at high fluxes (214 mJy – 384 mJy), the sources are almost perfectly reconstructed. The χ^2 values are around 0.3 for visibilities and even as low as 0.18 for closure phases, indicating some degree of overfitting. The model matches the data nearly perfectly, which suggests that fewer data points could suffice, and binning might be beneficial to avoid fitting noise. Given the 24-hour observation duration combined with all baselines - which is an idealized and less realistic scenario - the source is effectively overfitted. The metrics corroborate this conclusion (see Figs. 4.44 and 4.45), showing excellent values. When the flux is reduced by a factor of 10 (21.4 mJy – 38.4 mJy), the χ^2 values for visibility and closure phases approach unity, indicating a good balance between fitting and noise. Although larger deviations appear on longer baselines, the overall fits remain very good. These flux levels are well within the ngVLA's capabilities, as the core region, second component, and nearly all filaments are reconstructed accurately. This is further confirmed by the metrics in Figs. 4.46 and 4.47, which again show very strong agreement. It was noted in previous reconstruction sections that images with fluxes in the range 3.8 mJy to 0.2 mJy show weak or no detectable source emission, primarily due to the fixed dynamic range used for consistency across comparisons. The appropriateness of the chosen dynamic range was verified by calculating the peak flux divided by the RMS noise, determined in a region free of source emission. The dynamic range spans roughly seven orders of magnitude at 380 mJy total flux and about three orders of magnitude at 0.3 mJy total flux. An example image with 0.2 mJy total flux using an adjusted dynamic range is shown in Fig. 4.43.

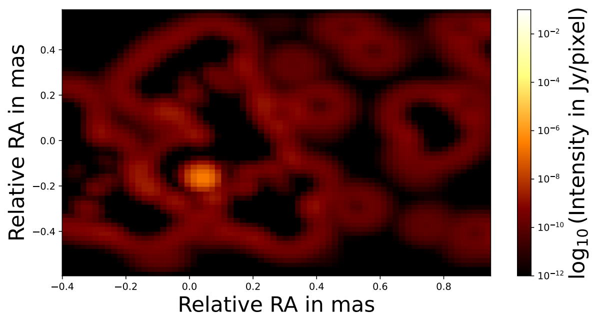

Figure 4.43: 94 GHz reconstruction with ngVLA at 70° declination and 0.2 mJy total flux. This is the same reconstruction showed in Fig.4.20a) but with adjusted intensity.

At a total flux of 3.8 mJy, the χ^2 values are close to 2, which would generally suggest a poorer fit. However, the data - especially at shorter baselines - is still well captured, so the overall structure, essentially reduced to two components, remains visible. The metrics remain very good and comparable to other reconstructions at 15 GHz. For the source at 0.4 mJy flux, the χ^2 values are dominated by noise. Consequently, the metrics are very high and do not provide meaningful insight; thus, they are omitted from the graphs for clarity. Compared to other frequencies, the NXCorr at 94 GHz is slightly lower (around 0.96 instead of 0.99), and the NRMSE is higher (around 0.6 instead of 0.4), indicating weaker similarity between the reconstructed and initial images. Nevertheless, the NXCorr values are still considered very high, and these differences are not substantial. Together with the χ^2 values, they show that reconstructions remain very reliable up to approximately 20 mJy. Reconstruction results at 94 GHz improve further when including the German stations (see Ch. 4.5.3). The highest flux image remains somewhat overfitted, with χ^2 values around 1.7 for visibilities and 1.8 for closure amplitudes, indicating good agreement at shorter baselines but increased noise at longer baselines. The metrics confirm that the inclusion of German stations enhances reconstruction quality, as reflected in improved NRMSE and NXCorr values.

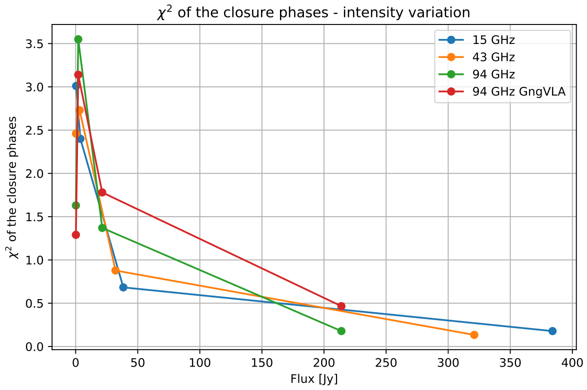

Figure 4.44: χ^2 of the closure phases on flux for each frequency of the ngVLA and 94 GHz for the ngVLA with German stations (GngVLA).

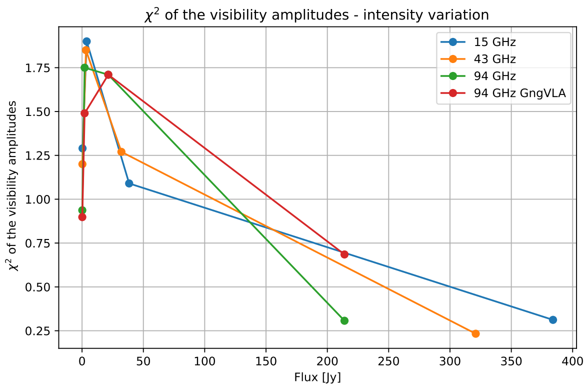

Figure 4.45: χ^2 of the visibility amplitudes on length for each frequency of the ngVLA and 94 GHz for the ngVLA with German stations (GngVLA).

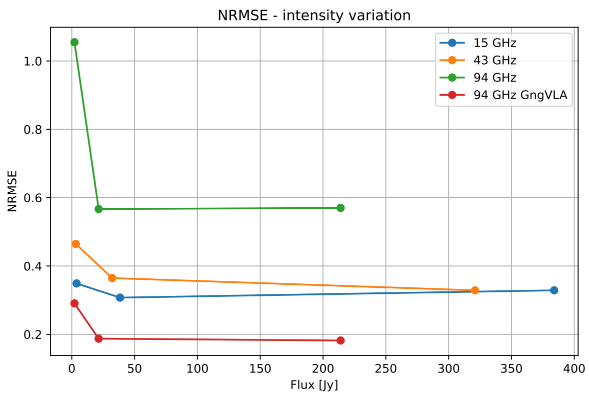

Figure 4.46: NRMSE on length for each frequency of the ngVLA and 94 GHz for the ngVLA with German stations (GngVLA).

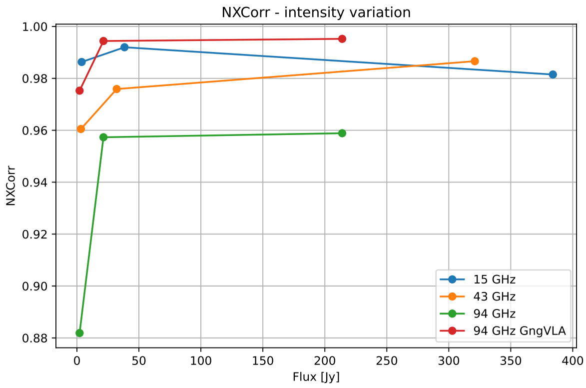

Figure 4.47: NXCorr on length for each frequency of the ngVLA and 94 GHz for the ngVLA with German stations (GngVLA).

5 Conclusion and Outlook

In this thesis, the capabilities of different planned next-generation arrays - the ngVLA and the LEVERAGE program -were tested. These arrays offer unmatched sensitivity and resolution, enabling the resolution of structures in relativistic jets that current VLBI arrays cannot capture, particularly at low flux densities. To carry out these investigations, three main steps were required:

1. Simulation
2. Ray tracing
3. Reconstruction

Motivated by the filamentary appearance of 3C279, a 3D RMHD simulation was conducted to create a generic source resembling the observed jet. High magnetic fields and low pitch angles lead to the development of various time-evolving instabilities, resulting in filamentary structures. Through visual inspection and cross-sectional analysis of the simulation, signatures of Rayleigh–Taylor, Kelvin–Helmholtz, and current-driven kink instabilities were identified. A series of ray-tracing calculations, including a parameter study of the emission properties, confirmed the presence of a helical structure in the simulated source. These simulations were then used to produce synthetic images, which were reconstructed at 15 GHz, 43 GHz, and 94 GHz while varying parameters such as declination, apparent source size, and total flux density. Reconstruction tests primarily involved the ngVLA, but additional reconstructions at 94 GHz were performed using the LEVERAGE configuration, which incorporates German, Hungarian, and Scandinavian telescopes (Kadler et al. 2024). This significantly extended the interferometric baselines and improved the angular resolution. In addition to visual inspection and χ^2 comparisons of visibility amplitudes and closure phases, quantitative image metrics such as NRMSE and NXCorr were computed to evaluate the similarity between the original and reconstructed images. While the LEVERAGE program showed significant improvements on smaller scales, it provided no substantial enhancement for the large-scale jet structures. Therefore, reconstructions of M87 at 86 GHz were carried out, where it was demonstrated that the ring-like structure around the black hole could only be resolved when additional European stations were included. Looking forward, further RMHD simulations could explore the triggering mechanisms of the aforementioned instabilities in more detail - especially the role of magnetic pitch and plasma inertia. Observationally, the RadioAstron team reported up to three distinct filamentary structures that were not captured in this simulation (Fuentes et al. 2023). Modifying the jet profile parameters could bring simulations closer to observations and enhance our understanding of instability formation and evolution. Regarding the synchrotron emission modeling, the classical approach following Pacholczyk (Pacholczyk & Roberts 1971) was used. This model could be improved through a fully numerical treatment according to Ghisellini (Ghisellini et al. 1985) - by adding effects of synchrotron self-Compton (SCC) or including broken power law regarding the SED - to better represent particle acceleration and radiative processes. Rescaling the SED would allow the inclusion of optical depth effects and extend the emission model to higher energies, where mechanisms such as inverse Compton scattering become relevant. Furthermore, ray tracing could be fine-tuned to replicate the specific features of 3C279 rather than a generic source model. For this, the grid of the simulations has to be enlarged to capture the small viewing angle. Polarimetric image reconstruction would also be highly beneficial, as it could reveal the orientation and evolution of the helical magnetic field and help identify shock structures within the jet. The LEVERAGE reconstructions so far have not included data from low-frequency SKA or ALMA. While SKA would improve coverage in the southern hemisphere, allowing the observations of Sgr A*, it is limited by its operational frequency range. Since the ngVLA is designed to complement ALMA, combined observations across a wide frequency range could provide detailed insights into the multi-scale structure of jets and black hole environments. Furthermore, it should be noted that the MEM reconstructions (Chael et al. 2016) are inherently biased by the choice of regularizer terms, which were kept constant throughout the reconstruction process. Different regularization weights or alternative imaging methods, such as the CLEAN algorithm (Högbom 1974) or resolve (Kim et al. 2025), would likely yield different results. Exploring such variations could provide a more comprehensive understanding of the reconstruction performance and its dependence on algorithmic choices. Overall, the results in this thesis highlight the potential of future radio interferometers such as the ngVLA and LEVERAGE to significantly advance our understanding of relativistic jets by delivering unprecedented resolution and sensitivity. These tools will be essential in resolving open questions in jet physics and gaining insights into mechanisms such as jet launching, collimation, and the role of magnetic fields near the black hole.

Bibliography

Aharonian F., Kelner S., Prosekin A. Y., 2010, Physical Review D—Particles, Fields, Gravitation, and Cosmology, 82, 043002

Bartelmann M., 2013, Theoretical astrophysics: an introduction. John Wiley & Sons

Bass M., Stryland E. W. V., Williams D. R., Wolfe W. L., 1995, Handbook of Optics Volume II Devices

Blandford R. D., Payne D., 1982, Monthly Notices of the Royal Astronomical Society, 199, 883

Blandford R. D., Znajek R. L., 1977, Monthly Notices of the Royal Astronomical Society, 179, 433

Bolatto A. D., et al., 2017, arXiv:1711.09960

Burke B. F., Graham-Smith F., Wilkinson P. N., 2019, An introduction to radio astronomy. Cambridge University Press

Burtscher L., et al., 2013, Astronomy & Astrophysics, 558, 46

Camenzind M., 2007, Compact objects in astrophysics. Springer

Carroll B. W., Ostlie D. A., 2017, An introduction to modern astrophysics. Cambridge University Press

Chael A. A., Johnson M. D., Narayan R., Doeleman S. S., Wardle J. F., Bouman K. L., 2016, The Astrophysical Journal, 829, 11

Collaboration E. H. T., et al., 2019, arXiv preprint arXiv:1906.11238

Cornwell T. J., Evans K., 1985, Astronomy and Astrophysics (ISSN 0004-6361), vol. 143, no. 1, Feb. 1985, p. 77-83., 143, 77

Dermer C. D., Menon G., 2009, High energy radiation from black holes: gamma rays, cosmic rays, and neutrinos. Princeton University Press

Fanaroff B. L., Riley J. M., 1974, Monthly Notices of the Royal Astronomical Society, 167, 31

Fromm C., Perucho M., Porth O., Younsi Z., Ros E., Mizuno Y., Zensus J., Rezzolla L., 2018, Astronomy & Astrophysics, 609, A80

Fuentes A., et al., 2023, Nature Astronomy, 7, 1359

Ghisellini G., Maraschi L., Treves A., 1985, Astronomy and Astrophysics (ISSN 0004-6361), vol. 146, no. 2, May 1985, p. 204-212., 146, 204

Goedbloed J. P., Goedbloed H., Keppens R., Poedts S., 2019, Magnetohydrodynamics: of laboratory and astrophysical plasmas. Cambridge University Press

Högbom J., 1974, Astronomy and Astrophysics Supplement, 15, 417

Honma M., Akiyama K., Uemura M., Ikeda S., 2014, Publications of the Astronomical Society of Japan, 66, 95

Hu X.-F., Mizuno Y., Fromm C. M., 2025, Astronomy & Astrophysics, 693, A154

Kadler M., Ojha R., Collaboration T., et al., 2015, Astronomische Nachrichten, 336, 499

Kadler M., et al., 2024, in Proceedings of the 16th EVN Symposium. pp 169–176

Kellermann K., Sramek R., Schmidt M., Shaffer D., Green R., 1989, The Astronomical Journal, 98, 1195

Kembhavi A. K., Narlikar J. V., 1999, Quasars and active galactic nuclei: an introduction. Cambridge University Press

Kim J.-S., Müller H., Nikonov A. S., Lu R.-S., Knollmüller J., Enßlin T. A., Wielgus M., Lobanov A. P., 2025, Astronomy & Astrophysics, 696, A169

Komissarov S., 1999, Monthly Notices of the Royal Astronomical Society, 308, 1069

Lai S., Thyagarajan N., Wong O. I., Diakogiannis F., Hoefs L., 2025, Monthly Notices of the Royal Astronomical Society, 536, 446

Lister M., et al., 2019, The Astrophysical Journal, 874, 43

Marscher A. P., 2009, arXiv:0909.2576

Marscher A. P., Gear W. K., 1985, Astrophysical Journal, Part 1 (ISSN 0004-637X), vol. 298, Nov. 1, 1985, p. 114-127., 298, 114

Martí J.-M., 2015, Monthly Notices of the Royal Astronomical Society, 452, 3106

Matsumoto J., Komissarov S. S., Gourgouliatos K. N., 2021, Monthly Notices of the Royal Astronomical Society, 503, 4918

Murphy E., et al., 2017, Next Generation VLA Document, 20, 15

Nan R., et al., 2011, International Journal of Modern Physics D, 20, 989

Nolting W., 2007, Elektrodynamik. Springer

Pacholczyk A. G., Roberts J., 1971, Physics Today, 24, 57

Padovani P., 1999, Vulcano Workshop 1998: Frontier Objects in Astrophysics and Particle Physics, 65, 159

Padovani P., et al., 2017, The Astronomy and Astrophysics Review, 25, 1

Porth O. J. G., 2011, PhD thesis

Porth O., Olivares H., Mizuno Y., Younsi Z., Rezzolla L., Moscibrodzka M., Falcke H., Kramer M., 2017, Computational Astrophysics and Cosmology, 4, 1

Ramesh N., Nityananda R., 1986, Annual review of astronomy and astrophysics, 24, 127

Rees M., 1966, Nature, 211, 468

Rybicki G., Lightman A., 1979, Radiative Processes in Astrophysics, A Wiley, New York

Schulga W., 2023, Long-Term Jet-Kinematics of Blazars in the TANAMI Sample

Selina R., McKinnon M. M., Murphy E. J., Farnsworth R., 2020, in Ground-based and Airborne Telescopes VIII. p. 1144518

Sikora M., Rutkowski M., Begelman M. C., 2016, Monthly Notices of the Royal Astronomical Society, 457, 1352

Sokolovsky K., Giroletti M., Corbel S., Anderson G., Stappers B., 2018, arXiv preprint arXiv:1803.02831

Thompson A. R., Moran J. M., Swenson G. W., 2017, Interferometry and synthesis in radio astronomy. Springer Nature

Urry C. M., Padovani P., 1995, Publications of the Astronomical Society of the Pacific, 107, 803

Venturi T., et al., 2020

Wang F., et al., 2021, The Astrophysical Journal Letters, 907, 7

Wrobel J., 1995, in Very Long Baseline Interferometry and the VLBA. p. 411

Wrobel J., Walker R., 1999, in Synthesis imaging in radio astronomy II. p. 171

Dankesagung

At this point, I would like to express my gratitude to everyone who contributed to the success of this work. First and foremost, I thank Dr. Christian Fromm, who made this interesting project possible for me and was always very helpful with advice and support throughout the entire work.
Many thanks also to Prof. Dr. Matthias Kadler, who gave me access to the topic of VLBI and provided important impulses to further develop it. His suggestions clearly advanced the work.
A special thanks goes to Ainara Saiz Pérez, who greatly helped me and the work through her proofreading. Her ideas and advice elevated the work to a new level.
Furthermore, I would like to thank all the staff of the Chair of Astronomy under the leadership of Prof. Dr. Karl Mannheim, especially the members of the AG Kadler and AG Fromm groups, for their warm welcome, guidance, and support. I especially want to thank my colleague Felix Glaser, who was always open for questions and discussions.
Zum Schluss möchte ich noch meinem privaten Umfeld danken, welches mich zu dem Menschen gemacht hat, der ich heute bin. Danke an alle Freunde, Bekannte und Verwandte, die Teil meiner Reise waren und ebenso ihren Teil zum Erfolg beigetragen haben.
Der allerletzte Dank gehört meinen Eltern, meinen Geschwistern und meiner Freundin. Vielen Dank für die Unterstützung.

Selbstständigkeitserklärung

Hiermit erkläre ich, dass ich die vorliegende Arbeit mit dem Titel *Jet physics with next generation VLBI arrays and radio telescopes* selbstständig verfasst und keine anderen als die angegebenen Quellen und Hilfsmittel verwendet habe.
Die Arbeit wurde in gleicher oder ähnlicher Form keiner anderen Prüfungsbehörde vorgelegt und auch nicht veröffentlicht.

Würzburg, den 18.06.2025

Unterschrift